LOW FREQUENCY TURBULENCE, PARTICLE AND HEAT TRANSPORT

IN THE WISCONSIN LEVITATED OCTUPOLE

by

Harold Ray Garner

A thesis submitted in partial fulfillment of the

requirements for the degree

DOCTOR OF PHILOSOPHY
(Nuclear Engineering)

at the

UNIVERSITY OF WISCONSIN-MADISON

1982

Abstract

Low Frequency Turbulence, Particle and Heat Transport

in the Wisconsin Levitated Octupole

Harold Ray Garner

Under the supervision of Professor Richard S. Post

Low frequency turbulence in the drift frequency range and its relation to the observed particle transport in the Wisconsin Levitated Octupole has been studied with a microwave scattering apparatus. The experimental parameters were: $T_e \sim T_i < 30$ eV, $n < 1.5 \times 10^{13}$ cm^{-3}, 200 G $< B_{p\text{ - average}} <$ 1.25 kG. The effect of shear on the transport was studied by the addition of a small toroidal field. By matching experimentally measured density profiles to those given by numerical solutions of the transport equations, diffusion coefficients were obtained. At high magnetic field strengths the gun injected plasmas initially decayed in such a way as to indicate a diffusive mechanism which scaled like $D_\perp \propto n^{-0.5}$ dominated the transport, damping out on a time scale of milliseconds. The residual diffusion scaled like classical, $D_\perp \propto \frac{n}{B^2}$, but was enhanced above classical by an order of magnitude. At lower values of magnetic field and for all times following injection, the diffusion scaled like classical, but again was an order of magnitude above classical.

Time dependent density fluctuation spectra were measured with an 8 mm microwave scattering diagnostic to correlate the drift wave portion of the spectrum with the observed diffusion. The density fluctuation spectrum of low frequency (1 kHz< ω <6 MHz) turbulence was measured for several values of perpendicular wavenumber, $k_\perp$. The spectrum peaked at a value of $k_\perp$ such that $k_\perp \rho_i \approx 1$. The frequency spectra were found to extend to 150 kHz and peak at 1 kHz, the lowest frequency measured. The fluctuation level, $\frac{\tilde{n}}{n}$, was found to vary from 5% in the $B_{P-average}(\psi = 4) = 1$ kG magnetic field case to 60% in the $B_{P-average}(\psi = 4) = 200$ G magnetic field case. Even with such high fluctuation levels, the diffusion attributable to the drift wave portion of the spectra could not account for the observed magnitude of the diffusion.

Electron heat transport was studied by fitting experimentally measured electron temperature profiles to those predicted by numerical solutions of electron energy transport equation. Electron heat transport was dominated by neutral gas refluxing from the titanium coated walls. It was found that ionization and excitation of neutral hydrogen accounts for 95% of the electron energy loss. The remaining 5% is shared between impurity radiation and heat diffusion. Assigning the full 5% to heat diffusion gives an upper bound to the electron heat transport coefficient of 5 times classical. Richard S Post

Acknowledgements

First and foremost, I wish to thank Professor Richard S. Post, whose ideas, advice, and support has made my graduate career successful and rewarding. My first conversation with Dr. Post convinced me to come to Wisconsin and ask him to be my advisor. It was the best decision I have made.

I wish to thank Sensei Sugiyama, Sensei Schulz, and John Pueschner, for they have shown me how to surface the budo spirit which existed within me.

I wish to thank Dr. Callen, Dr. Prager, and the rest of the faculty for teaching me Plasma Physics and for their valuable advice.

The much appreciated technical expertice of John Laufenberg and Tom Lovell made it all work. John Twichell, Carl Karcher, and Mike Zarnstorff were particularly helpful with the data aquisition and data analysis systems used in this research. I also wish to thank the rest of my fellow graduate students who contributed mentally and physically, particularly late at night when nothing seemed to work.

I also wish to thank Kay Shatrawka and Trudy Rempel for editing this manuscript.

This work was supported by the United States Department of Energy.

Table of Contents

Chapter 1

Introduction

Diffusion of plasma across field lines in the Wisconsin Levitated Octupole has been studied by many groups for many years.[1,2,3] These studies were carried out on relatively low density plasmas, 10^9 cm^{-3}< n <10^{12} cm^{-3}, for a variety of magnetic field strengths, with and without shear. The higher density plasmas were cold, $T_e = T_i = 1$ eV, and collisional (mean free path less than the connection length between poloidal mirrors). The lower density plasmas were hotter, $T_e = 10$ eV, $T_i = 20$ eV, and collisionless.

Experimental techniques involved the measurement of ion saturation current profiles and temperature profiles with Langmuir probes to determine the ion density profile. Striped particle collectors mounted on the walls of the Octupole were used to measure the total flux of particles to the wall of the device.[4,5] The cross field (perpendicular) particle diffusion coefficient was then calculated using $D_\perp = -\frac{\vec{\Gamma}}{\vec{\nabla} n}$.

For extremely low fields ($B_{p\text{ - average}} = 40$ Gauss), it was found that the particle diffusion was classical. For stronger magnetic fields, the transport was found to be dominated by

vortex diffusion. This diffusion mechanism has been named such because of the large, machine-sized potential structures which were present. It was also demonstrated that adequate power existed in the electric field spectrum for these vorticies to account for the observed diffusion.[6] When these large vorticies were present the diffusion coefficient, $D_\perp$, was found to scale like $n^{-0.5}$, independent of $|B_p - \text{average}|$ with $B_T = 0$ G. These low frequency, long wavelength potential structures have been mapped out in space using a (toroidally) movable cart to which an array of Langmuir probes had been mounted. It has also been found that these large vortex structures can be modified by the addition of a small amount of toroidal field (shear), or by increasing the plasma viscosity. They have been modified in such a way as to break up the potential structures into smaller wavelengths, thereby reducing their contribution to the diffusion.

These vortex (convective cell) modes and their associated enhanced particle diffusion were studied theoretically by many groups including Okuda, Dawson, Kamimura, and Montgomery.[7,8,9,10] It has been found analytically and in numerical simulations that large vorticies could exist. They were also able to predict the scaling of the diffusion coefficient when plasma diffuses under the influence of these modes and this scaling was the same as that which was

experimentally observed. These simulations have also predicted that the diffusion scaling should change from $n^{-0.5}$ to $n^{-1.0}$ as the low frequency dielectric constant approached a value of 1.0, which was also observed in the experiment.[11] The major discrepancy between theory and experiment was found to be the magnitude of the diffusion coefficient. Theory predicted a diffusion level which was much less (by approximately 10^2) than that experimentally observed. This was reconciled by the introduction of a 'turbulence temperature', T^*, which replaced the thermal temperature used in the theoretically derived diffusion equation. The diffusion equation would then calculate the proper magnitude for the diffusion coefficient, indicating that these modes are excited above thermal levels in the plasma.

In order to attribute the diffusion in these low density plasmas to vortex diffusion, and thus calculate T^*, the contribution of other fluctuations to the net diffusion had to be measured. The higher frequency, shorter wavelength portion of the spectrum was measured with probes, and was found to contribute little to the diffusion when the large vortex structures were present.[11] Since Langmuir probes have a number of limitations; they may perturb the plasma, their response to oscillating quantities ($\tilde{n}$, $\tilde{V}_f$) is questionable, and they can resolve wavelengths only by cross correlation of several probes. It was decided to construct a new diagnostic for the Octupole, a

microwave scattering system, to better measure the wavelengths and frequencies of the non-vortex modes.

This system was designed principally to study turbulence in the drift frequency range, $\omega < \omega_*^e$. Receivers were positioned to collect microwaves scattered from density fluctuations with toroidal wavelengths between 0.5 cm and 5.6 cm. This wavelength band was chosen because the drift wave turbulence is expected to have the greatest growth rate at wavelengths for which $k_\perp \rho_i \sim 1$, corresponding to approximately 3 cm for the plasmas and magnetic field strengths of interest. The receiver system for the microwave scattering diagnostic was also designed so that it could measure turbulence in both the absolute-minimum-B (inside the magnetic separatrix) and the average-minimum-B (outside the magnetic separatrix) regions of the Octupole. A receiver was also installed in the radial direction to measure the radial wavelengths of the turbulence, and to determine if any k-space anisotropy was exhibited by the modes. Refraction and attenuation effects limit the range of plasma density over which the scattering device, operated at a frequency of 35 GHz, can be used to less than 1.7×10^{13} cm^{-3}. The minimum fluctuation level detectable by the system is about 10^4 times the thermal fluctuation level $\langle |n(k)|^2 \rangle = nV$, where V is the scattering volume.

In addition to the installation of the microwave scattering diagnostic, several new plasma sources have come on line, allowing us to study transport in higher density and temperature plasmas. The direction of research on the Wisconsin Levitated Octupole has recently been to hotter, higher density plasmas, and away from the lower density plasmas where the bulk of the vortex diffusion work was done. With the installation of the 'intermediate density' Marshall gun came hot plasmas ($T_e = T_i = 30$ eV) with densities to 2×10^{13} cm^{-3}, which is above the critical density for the 35 GHz scattering apparatus. Even greater densities, to approximately 1×10^{14} cm^{-3}, can be made with either of two 'big' guns, but at a lower plasma temperature. This is again above the critical density for the microwave scattering system. Since all plasmas diagnosable with the microwave scattering apparatus can be made with the 'intermediate density' gun, it is used exclusively.

With the installation of these new plasma sources, specifically the intermediate density gun with its higher gas to plasma conversion efficiency and higher total plasma energy content (nkT), plasmas capable of burning out the neutral particles in the center (regions most distant from the walls) of the device were made. Subsequent electron temperature gradients arose from the spacially uneven energy loss out of the neutral excitation and ionization channel. This caused peaking of the

electron temperature at the separatrix, and a lowering of the temperature near the plasma boundary where the neutral density is higher. Since electron temperature gradients can now be made in the Octupole, a heat transport study was done to determine the relative contribution of each of the electron energy loss channels, including heat diffusion. An attempt to correlate any enhanced heat transport with the fluctuation level in the plasma was done.

This thesis contains eight chapters. Chapter one is this introduction. Chapter two contains a description of the Wisconsin Levitated Octupole and a description of the microwave scattering hardware used during this research. Chapter three is a review of all pertinent theory used throughout this thesis. This will include theory relating the fluctuating density to the scattered power, data processing (FFT's, smoothing, numerical simulations, etc.), vortex diffusion theory, drift wave theory, and various theories connecting the fluctuating quantities ($\tilde{n}$, $\tilde{V}_f$) to diffusion coefficients. Chapter four shows raw data and the associated spectra for the density fluctuations measured with the microwave scattering apparatus. Chapter five contains calculations of diffusion coefficients from experimental time dependent density profiles and a calculation of the transport attributable to the drift frequency portion of the fluctuation spectra. Numerical solutions to the particle diffusion equation

including contributions from vortex diffusion and non-vortex diffusion will be shown. Chapter six describes the experiments done to understand the electron heat transport in the Octupole. Measurments of the experimental time dependent electron temperature profiles and the corresponding numerical solutions of the electron energy balance equation will be given. Chapter seven contains a summary of other experiments that were conducted. This will include a comparison of data taken with Langmuir probes ($\tilde{I}_s$, $\tilde{V}_f$) and data taken with the microwave scattering diagnostic ($\tilde{n}$). There will also be a discussion of some of the previous work done with microwave scattering diagnostics on other devices including tokamaks and spherators. Raw data, fluctuation spectra, and the associated diffusion coefficients are discussed for experiments carried out when the Octupole was operated as as Octupole-Tokamak hybrid with a current being carried by the plasma. Chapter eight includes conclusions and proposals for future work.

References for Chapter 1

[1]G. A. Navratil, R. S. Post, and A. B. Ehrhardt, Phys. Fluids 20, 156(1977).

[2]G. A. Navratil, R. S. Post, and A. B. Ehrhardt, Phys. Fluids 22, 241(1977).

[3]J. R. Drake, D. W. Kerst, G. A. Navratil, R. S. Post, S. Ejima, R. LaHaye, C. P. Moeler, T. Ohkawa, P. I. Peterson, R. Prater, and S. K. Wong, in Plasma Physics of Controlled Nuclear Fusion Research (International Atomic Energy Agency, Vienna, 1976), Vol. II, p. 333.

[4]A. Cavallo, Phys. Fluids 19, 394(1976).

[5]J. R. Drake, J. R. Greenwood, G. A. Navratil, and R. S. Post, Phys. Fluids 20, 148(1977).

[6]A. B. Ehrhardt, and R. S. Post, Phys. Fluids 24, 1625(1981).

[7]H. Okuda and J. M. Dawson, Phys. Fluids 16, 408(1973).

[8]T. Kamimura and J. M. Dawson, Phys. Rev. Lett. 36, 313(1976).

[9]C. Z. Cheng and H. Okuda, Nucl. Fusion 18, 587(1978).

[10]J. B. Taylor and B. McNamara, Phys. Fluids 14, 1482(1971).

[11]A. B. Ehrhardt, H. R. Garner, G. A. Navratil, and R. S. Post, Phys. Fluids 24, 1859(1981).

Chapter 2

Experimental Apparatus

The transport studies described in this thesis were performed on the Wisconsin Levitated Octupole. Many of the engineering details of its construction and operation can be found in previously released literature.[1] However, since the machine is continuously being upgraded, it is necessary to include a description of the operating modes that were used when taking data for this thesis.

General Machine Description

The Wisconsin Levitated Octupole toroidal vacuum vessel was constructed from aluminum (Fig. 1). It has continuously variable, independently driven, poloidal and toroidal fields. The poloidal field is generated by inductively driving the four internal aluminum hoops within the vacuum vessel.

It is possible to "levitate" the four internal rings for 20 msecs during a discharge by pneumatically driving the titanium hoop supports in and out. Levitating the rings removes the hoop supports from the plasma confinement region, thus preventing them from being bombarded with plasma.

Figure 2 shows a poloidal cross section of the Octupole with the poloidal field lines drawn in. There are three degenerate poloidal field nulls along the center line of this view. The volume between the hoops and the separatrix field line is called the private flux region and is absolute-minimum-B stable to MHD activity. The volume between the separatrix and the critical field line is referred to as the common flux region and is average-minimum-B stable.

Figure 3 shows a poloidal cross section with the poloidal field mod-B surfaces drawn in. Note that the field strength peaks near the hoops and drops to zero at the degenerate field nulls.

Toroidal field is generated by passing currents along the aluminum walls making up the torus. The toroidal field has the typical 1/R behavior, where R is the distance along a major radius. The toroidal field strengths quoted in this thesis refer to the field strength at the midplane of the torus.

Table 1 gives a summary of the operating parameters for the Wisconsin Levitated Octupole.

At present the Octupole is equipped to do a variety of experiments. A high power (2 MW) oscillator and associated antenna has been installed to study ion cyclotron heating.[2] Neutral beams (2 MW) have also been installed to study plasma heating.[3] There also are three small hoops mounted near the upper lid of the Octupole which are sometimes used to divert poloidal flux into a limiter. These hoops were used in a poloidal divertor experiment,[4] but were not used during the experiments discussed in this thesis.

Significant improvement in wall surface cleanliness and an improvement in background neutral pressure has been achieved through the installation of an array of 6 titanium getters. Typical pressures in the Octupole are 6×10^{-8} torr, composed mainly of hydrogen and water, as measured with a residual gas analyzer. Seventy-five percent of the vacuum chamber surface area[5] is now being continuously coated with titanium between discharges. The pumping speed of neutral H_2 on the titanium has been measured and is 1.0×10^5 ℓ/sec. A regular program of discharge cleaning has been instituted to further condition the surfaces of the vacuum vessel, and thus reduce reflux of impurities and fuel gas during a discharge.

Plasma Parameters

Most of the plasmas under study were injected from coaxial Marshall guns into the crowbarred magnetic fields. The measurements were then made in the afterglow plasma. There was at least 100 microseconds of delay between gun injection and the beginning of the fluctuation measurements. This allowed the large potential fluctuations generated during the plasma injection and trapping phases to subside. By then, the plasma also had become toroidally symmetric.

There are three coaxial guns mounted on the Octupole which are capable of injecting plasmas. Two are virtually identical, one has a copper barrel and one has a stainless steel barrel. These are referred to as the "big" guns. They produce very dense ($n \simeq 7 \times 10^{13}$ cm^{-3}) warm plasmas ($T_e \sim T_i \sim 15$ eV) at high poloidal magnetic field strengths ($B_{p\text{-average}}$ ($\psi = 4$) = 1 kG). These guns are principally being used by the high beta research group. These guns produce plasmas whose density is far above the cutoff density, $n_c \leq 1.7 \times 10^{13}$ cm^{-3}, for a 35 GHz microwave scattering system.

The third gun, referred to as the "intermediate" density gun produces a plasma with an electron density of 2×10^{13} cm^{-3} at the maximum poloidal field strengths

($B_{P\text{-average}}(\psi = 4) = 2$ kG). The temperatures achievable with this gun are $T_e \sim T_i < 30$ eV, at a reduced density, when operated in a gas starved mode. Under normal operating conditions, for a poloidal field strength of 1 kG (average at $\psi = 4$) the gun fills the machine with a plasma whose density peaks on the separatrix and is equal to 1.5×10^{13} cm^{-3}. In this case $T_e \sim T_e \sim$ 15 eV at 0.25 msec after injection. As the field strength is lowered the amount of plasma trapped in the magnetic field is less and colder. This gun is capable of overlapping the full parameter range of the "big" guns when the experimenter wants a less dense plasma, i.e. $n < 1.5 \times 10^{13}$ cm^{-3}. Since the scattering apparatus is constrained to use only the less dense plasmas, the "intermediate" density gun was used exclusively for these studies.

The "intermediate" density gun was also used to produce the plasmas for the heat transport studies. This was for two reasons. First, it could produce a hotter plasma, $T_e \sim 30$ eV. Second, it was more efficient in its gas usage. This meant that for a given density of plasma trapped in the Octupole magnetic field, the "intermediate" density gun introduced a smaller amount of nonionized neutral hydrogen into the torus. Typically, the background pressure rise during a discharge, when the "intermediate" density gun was used with extensive

was only to 8×10^{-7} torr. This rise occurred a few milliseconds after plasma injection.

Plasmas were also made in the Octupole without having to use a gun when the octupole was operated as an octupole-tokamak hybrid. In this mode, neutral gas which had been puffed into the torus, was pre-ionized with a 2.45 GHz (100 watt) microwave source. The toroidal field was fired first, then the poloidal field was fired, placing a 30 volt potential across the poloidal gap. This drove a toroidal current in the plasma and the aluminum hoops. This mode of operation produced a plasma whose density was 5×10^{12} cm^{-3}. The electron temperature was greater than 30 eV. This operating mode was used because of its resemblance to tokamak and FM-1[6] plasmas which allowed us the opportunity to compare data and results obtained with the microwave scattering system.

Auxiliary Diagnostics

There are a host of diagnostics available for use on the Levitated Octupole. Many of these diagnostics took data which did not enter directly into the calculation of the fluctuation spectrum or the transport calculations. These diagnostics were monitored to insure that day to day and shot to shot variations in the plasma were minimized.

The principle diagnostic used by all experimenters is the 70 GHz microwave digital multiradian fringe shift interferometer[7]. This instrument is absolutely calibrated. It is used to measure the plasma density through the midcylinder of the Octupole along a chord from the top aluminum wall to bottom aluminum wall. By measuring the phase shift of a 70 GHz, 20 milliwatt beam as it passes through the plasma and recording this information in a digital counter circuit, the time dependent density can be read out directly on an oscilloscope. This interferometer has measured plasma densities to 7×10^{13} cm^{-3} before being cutoff. Components have been ordered to upgrade this interferometer to 140 GHz, so that densities to 3×10^{14} cm^{-3} can be measured.

There are a number of spectroscopic diagnostics installed on the Octupole. All of these diagnostics are relatively calibrated allowing one to compare the amount of radiation emitted in a variety of lines from discharge to discharge. Since they are not absolutely calibrated it is not possible to calculate the power radiated in these lines from those diagnostics. A "hydra head" is mounted on the lower lid of the torus, viewing the midcylinder. It contains four detectors, one measuring each of the following lines: oxygen III, carbon III, nitrogen III, and hydrogen-beta. Mounted on the upper lid,

viewing the midcylinder, is a vacuum ultraviolet spectrometer, a monochrometer, and a total radiated power bolometer.[8]

There are several diagnostics used to measure vacuum quality in the Octupole. There are ionization gauges mounted in a variety of positions, and two fast (nude) ionization gauges are mounted immediately inside the aluminum vacuum wall. The nude gauges are protected by chevrons to minimize plasma bombardment during a discharge. These chevrons limit the conduction of neutral gases from the vacuum tank to the ionization gauges, imposing a limitation on the response time. The response time is less than 0.2 msec, which was more than adequate for all experiments that were done. There also is a differentially pumped residual gas analyzer mountable either on a 50 cm (2" diameter) stalk (limiting response times to 1.0 msec) or a neutral charge exchange analyzer (with an even longer response time).

The use of probes to measure plasma properties are heavily relied upon for most experiments being done on the Octupole. Plasma energy content is sufficiently low for all the gun injected plasmas that probes sustain very little damage due to plasma bombardment. This is not true for the ohmically heated octupole-tokamak hybrid discharge, where one shot is sufficient to destroy a probe due to heating from plasma bombardment. For

normal "gun" injected plasmas, arcing from probe tip to probe tip or continual exposure to the titanium getter "shine" usually limits the lifetime of probes. Probes are small in volume compared to confined plasma volumes. No detectable perturbation to bulk plasma characteristics (n_e, T_e, T_i, τ_{n_e}, τ_{T_e} τ_{T_i}) is seen for the plasmas under study.

Double tipped and triple tipped Langmuir probes biased to collect ion saturation current and measure plasma admittance[9] were used to measure the time dependent density and electron temperature profiles presented in this thesis. These probes are constructed with platinum electrodes to minimize surface contamination problems. These electrodes were supported by a ceramic stalk which extends from the probe tips to the probe body (stainless steel), which was kept outside the plasma confinement region. When measuring ion saturation current with probes, the bias was kept high compared to floating potential or electron (or ion) temperature. That is, $V_{bias} = 150$ V $>> T_e = T_i = 30$ eV $>> V_{floating} \simeq 10$ V. Admittance probe techniques involved measuring the sheath resistance of a normal Langmuir probe by sweeping the bias on the probe by a small amount, $V_{sweep-peak\ to\ peak} \sim 1$ V, at a high frequency, $f = 250$ kHz. This was sufficiently fast to measure bulk plasma temperature changes. Once the sheath resistance and saturation current is known the potential drop across the sheath can be

calculated. The potential drop across the probe sheath is proportional to electron temperature.

A paddle probe [10] was used to measure the ion current, the electron current, and the net plasma current flowing around the toroid. This allows one to estimate the plasma rotation velocity, and thus calculate the Doppler shift (if any) in the fluctuation data from the plasma frame to the laboratory frame. This probe was constructed of two collecting electrodes of equal area. Each collecting area was a flat, plane surface, one surface normal points in the toroidal direction and the other surface normal points in the anti-toroidal direction. The collected current is proportional to the local flux of electrons and ions.

A miniaturized gridded energy analyzer probe was constructed and used [11] to measure the ion velocity distribution function, thus the ion temperature. This probe contains several biased grids and a collecting cup, all built into a 1/4" probe body. This probe was used to measure the ion temperature in all the experiments performed for this thesis.

There are two particle collectors still mounted in the Octupole. Particle collectors are constructed from a flat plate of circuit board material with interdigitated aluminum stripes

electroplated on the surface. The collectors were used to measure the particle flux to the walls of the device. These remaining collectors have movable shields, which can be swung over them to stop them from being bombarded with plasma. Plasma bombardment of the plastic is undesirable, because high Z contaminants such as carbon will be released. It is particularly important for the ICRH and neutral beam heating experiments to keep the plasma as "clean" as possible. With the limited number of collecters, complete measurements of the flux at various wall locations cannot be made. However, comparisons can be made among data taken with the existing collectors, in the present high density plasmas, and collectors mounted in the same locations where extensive data was taken in the low density plasmas.[12] This information was used in the neutral transport model. This model, in turn, was used in the electron heat transport studies.

Hall probes and B-dot probes were used to measure the local magnetic field, and fluctuating magnetic field, at a variety of locations around the torus. This included measurements of magnetic field fluctuations induced by plasma activity in and around the areas where microwave scattering was used to measure plasma density fluctuations.

The frequency of the drift wave turbulence under study was low, i.e. less than or approximately equal to the electron diamagnetic drift frequency, ω_e^*. For the plasmas studied $\omega < \omega_*^e = k_\perp \frac{T_e}{eBn} \frac{dn}{dr}$ was less than 10 kHz. Therefore, the scattering system was designed to measure frequencies from 0 Hz to 1 MHz, which covers the frequencies of interest. This frequency limit was set by the bandwidth of available electronics which amplified the signals from the balanced mixers. The balanced mixers have a bandwidth greater than 2 GHz.

The wavelength, and thus the wave number, $k_\perp$, for drift wave modes can be estimated from the equation: $k_\perp \rho_i \sim 1$. The perpendicular wave number is $k_\perp$. The ion gyroradii is ρ_i. The range of $k_\perp \rho_i$ measurable with the scattering system is from 0 to 4, set by the $k_\perp$'s viewable with the available receivers, the range of ion temperatures, and the magnetic field strength. An illustration of accessable $k_\perp$ space is given in Fig. 4 for $\psi = 4$ (absolute minimum-B region) and $\psi = 7$ (average minimum-B region). There is a receiver module installed to measure several values of $k_\perp$. Figure 4 also shows the values of $k_\perp$ observable.

The frequency of the drift wave turbulance under study was low, i.e. less than or approximately equal to the electron diamagnetic drift frequency, ω_e^*. For the plasmas studied $\omega < \omega_*^e = k_\perp \frac{T_e}{eBn} \frac{dn}{dr}$ was less than 10 kHz. Therefore, the scattering system was designed to measure frequencies from 0 Hz to 1 MHz, which covers the frequencies of interest. This frequency limit was set by the bandwidth of available electronics which amplified the signals from the balanced mixers. The balanced mixers have a bandwidth greater than 2 GHz.

The wavelength, and thus the wave number, $k_\perp$, for drift wave modes can be estimated from the equation: $k_\perp \rho_i \sim 1$. The perpendicular wave number is $k_\perp$. The ion gyroradii is ρ_i. The range of $k_\perp \rho_i$ measurable with the scattering system is from 0 to 4, set by the $k_\perp$'s viewable with the available receivers, the range of ion temperatures, and the magnetic field strength. An illustration of accessable $k_\perp$ space is given in Fig. 4 for $\psi = 4$ (absolute minimum-B region) and $\psi = 7$ (average minimum-B region). There is a receiver module installed to measure several values of $k_\perp$. Figure 4 also shows the values of $k_\perp$ observable.

A chord from the upper lid to the lower lid of the machine passing just inside the outer hoops was chosen for the path of the probe beam. The beam radius is 3.8 cm at the launching structure, a parabolic mirror (see Fig. 5). The beam radius is defined as the radius out to which the beam contains 95% of its power. The beam spread at full width half max in power of the gaussian beam is 7°. This results in a beam 6.7 cm in radius at the dump mirror. A 5 cm radius dump mirror (receiver) then captures 80% of the power launched. Geometric calculations had predicted that 76% of the power would be captured, in good agreement with the measured value. Parabolic receivers mounted on the torus floor, along a toroidal tangent, and along a radius, can be tilted to receive scattered power from anywhere along the chord. Figure 6 shows the placement of receiver mirrors (B, D, E, F), on the lower lid of the octupole for the scattering system, the dump mirror (C), and the receiving mirror (A) for the 70 GHz interferometer. The tilt angles for mirrors (D, E, F) are set by push rods penetrating the vacuum wall. The center of the scattering volume can in this way be adjusted to view portions of both the absolute minimum-B stable regions (ψ=4 to ψ=5.7) and average minimum-B stable confinement regions (ψ=5.7 to ψ=7). Plasma is actually contained between the internal ring surface (ψ=2.5) and the last $\oint \frac{d\ell}{B}$ stable "critical" surface, $\psi = 7.8$.

Calculations of the scattering volume, weighted by the gaussian response functions (gain patterns) of the parabolic receivers and transmitters have been made for the three viewing regions. (See Table 2.) Region one is adjacent to the upper outer hoop centered at $\psi = 4.0$. Region two is centered on the nose $\psi = 7.0$. Region three is adjacent to the lower outer hoop at $\psi = 4.0$. Each region corresponds to one $\vec{k}$ value of the wave under study, selected by the equation: $\vec{k}_s = \vec{k}_i + \vec{k}$. $\vec{k}_s$ is the scattered wave vector (see Fig. 7). $\vec{k}$ is the wave vector associated with modes in the plasma. $\vec{k}_i$ is the incident "probe wave" wave vector. $|k_i| = 2\pi/0.8$ cm^{-1}. Gaussian weighted scattering volumes vary in size from $V = 21.89$ cm^3 to $V = 113.3$ cm^3. The scattering angle, $\theta_s = \tan^{-1}(k/k_i)$, varies from 8.1° to 60°. Due to the finite extent (width) of the probe beam, the scattering will have an angular extent, $\Delta\theta_s = \frac{2}{a_o |k_i|}$, where a_o is the beam radius. The calculations summarized in Table 2 were made with computer codes "ANTANE" and "VOLUME".[15] More complete descriptions of these calculations can be found in Chapter 3.

The transmitted beam has its k-vector (for B_p only) nearly perpendicular to $\vec{B}_o$ and its electric field vector $\vec{E}$ perpendicular to $\vec{B}_o$ as it enters and leaves the plasma. The orientation of $\vec{k}_i$, and $\vec{E}$ relative to $\vec{B}_o$ change along the beam path (recall Fig. 2).

The plasma density gradients seen by the transmitted beam upon entry, and while traveling through the plasma region are sufficiently gentle so as to keep refraction and reflection of the beam from affecting the magnitude calibration data by more than 5%. This number was calculated with a ray tracing code. The code calculated the reflection and refraction coefficients along the path of the beam as it passed through the plasma. The calculations were made using the measured density profiles and the octupole vacuum flux plots (to measure the angle of the density gradient normal with respect to the beam). The scattered beam follows a path very close to the main beam, and therefore, the calculations were done for the main beam only, and are assumed to represent the behavior of the scattered beam. This is for peak plasma densities less than the critical density, $n_c = 1.7 \times 10^{13}$ cm^{-3}. The critical density is calculated from equating ω_i, the microwave beam frequency, to ω_{pe}, the electron plasma frequency. Figure 8 shows that for all times after plasma injection ω_{pe} was less than ω_i for the two magnetic field strengths (and resulting trapped plasma) which were studied extensively in Chapters 4 and 5. Refraction causes a phase shift in the microwave beam as it moves through the plasma because its phase velocity changes. For the microwave scattering system, only the power scattered by waves was measured, preserving the phase information was not necessary. So refraction of the beam was unimportant. Reflection of the

beam as it traverses the plasma for a typical octupole density profile was less than 5% of the beam power, for peak densities less than n_c. For a plasma whose collision frequency, ν, is small compared to the beam frequency, ω, attenuation becomes significant only when the plasma density is greater than the critical density.[16,17] Only when $\nu > \omega$ would the attenuation of the microwave beam be larger than the reflection of the beam.

A homodyne system was chosen for the Octupole since it was simple, inexpensive, and had enough sensitivity to make the measurements desired. A homodyne system is described as a system whose transmitter signal is the same as the local oscillator signal used in the mixer. By definition, a homodyne system has no intermediate frequency. The local oscillator power is a small sample of the power from the transmitter oscillator. This sample is taken before the power is delivered to the launching antenna. This is shown schematically in Fig. 9. It is informative to trace along the path of the microwaves and detected signals to further describe the operation of the scattering system that was on the Octupole. The oscillator is a Varian[18] Extended Interaction Oscillator (E.I.O.), which continuously supplies microwaves at 35 GHz, and at a power level up to 100 watts. The E.I.O. is more difficult to install and operate than a klystron, but a klystron operated at this frequency and power level would have an intolerably high

noise level. The power supply for the E.I.O. is a specially modified traveling wave tube power supply made by Universal Voltronics.[19] With this power supply the E.I.O. could be run over its entire power output range with safety. Figure 9 shows that the power output of the oscillator is divided into two paths. A small amount of power (.01%) is diverted into the reference arm, this is the local oscillator power which is delivered to the balanced mixer. The bulk of the power from the E.I.O. is tranmitted in waveguide to vacuum feed-throughs and eventually to the 4" diameter parabolic launching mirror. In this high power arm, there also is a coupler used to measure the power reflected from the launching mirror (and plasma) back towards the E.I.O. The scattered beam is captured in the receiving mirror. This scattered power passes through vacuum feed-throughs to the balanced mixer where it is mixed with the reference power. The scattered power is much less (-20 dbm) than the reference power of approximately 3 mW. The balanced mixer consists of hybrid ring (where the two signals are actually mixed), two diode mounts (which are adjustable to "balance" the mixer), and two attenuators (which control the power level of the two signals to guarantee that the balanced mixer has a linear response to the scattered signal). The mixer is said to be balanced when the response of the two diodes is equal, thus canceling out most of the noise in the reference arm signal.[20] All components used in fabricating the balanced mixer

were manufactured by Baytron.[21] The output of the balanced mixer is then fed into a Tektronix differential amplifier[22] which has an adjustable gain (typically a gain of 1000 was used). This amplifier has a bandwidth of 1 MHz. The output of the amplifer can then be viewed on an oscilloscope or be digitized, and then processed on the computer. The digitizers used were LaCroy 8210, 10 bit, 8 K word sample size, 1 MHz sample rate units.[23] The on-line data acquisition computer is a PDP-11/20.[24]

The hardware cost of the fully operational system, not including the digitizers or computer, was less than $35,000.

The sensitivity of the scattering system is defined as the minimum scattered signal which can be discerned from the inherent noise of the entire system. For the Octupole scattering system, the sensitivity at high frequencies (f >200 Hz) was set by the noise level in the differential amplifier. At lower frequencies (f<200 Hz), the sensitivity was set by a combination of the noise in the power supply (60 Hz and 120 Hz components) for the E.I.O. and by machine vibration (at very low frequencies, f ~ 10Hz).

Measurement of plasma emission at 35 GHz by the microwave radiometer confirmed that plasma radiation contributed less than 0.1% to the signal picked up by the receiving mirrors. The 20%

of the probe beam power not picked up by the dump mirror did not contribute to the measured scattered power through setting up cavity modes, or by specular reflection off the walls. The power reflected off the walls was found not to be a problem in this experiment. There are at least two possible explanations for this fact: the rough surface flakes of titanium may be absorbing the microwave power; the solid angle of the receiver is very small compared to all the possible solid angles into which reflecting microwaves may emerge from the wall. This power was below the sensitivity of the balanced mixers when they were attached to the receiver and transmitter mirrors for the 70 GHz inteferometer system (see Fig. 6, Mirror A). These mirrors do not aim toward the main probe beam. They are mounted so the orientation of the $\vec{E}$ (of the microwave scattering system probe wave) is perpendicular to the 70 GHz interferometer mirrors receiver $\vec{E}$. In units of $\bar{n}$, the overall sensitivity of the microwave scattering system is approximately 3.6×10^{10} cm^{-3} (or less). This means that the plasma fluctuation level must be at least 1% to be detectable in a 3.6×10^{12} cm^{-3} plasmas. The fluctuation level corresponds to $S(k) = 10^{4}$, where $S(k) = 1$ is the level of thermal fluctuations for a plasma. See Chapter 3 for a further discussion of the spectral density function, S(k).

The scattering system on the Octupole was absolutely calibrated. This means that the system was calibrated such that $\bar{n}(\omega,k)$ could be expressed as a function of the system output power or voltage, where all constants were known. In some systems this calibration is estimated by summing up all the gains, losses, and conversion factors for all the microwave equipment. This technique gives a poor estimate, so for the Octupole system an alternative technique was used. The overall system calibration was done in one step by measuring the power scattered from a radar target of a known scattering cross section,[25] and thus the multiplicative constant (the overall system gain) could be evaluated. See also Chapter 3. This could be done easily on the Octupole since there was access to the center of the scattering volumes with probes (Fig. 5). A small stainless steel sphere mounted on a glass stalk was used to do the calibration. Before and after each data taking run, the sphere was inserted into the scattering volume through a vacuum lock to insure that the system sensitivity had not changed. The system linearity was also checked by inserting spheres of different sizes, and thus cross sections, and then noting the system output voltage.

It is apparent from the above discussion, that the homodyne system selected for the Octupole had the necessary sensitivity

to measure the fluctuations of interest. It was also easy to build, calibrate, and operate.

The alternative to the homodyne system which was not selected is of the heterodyne type. A heterodyne system has a high power (> 1 W) oscillator for the main probe wave, and a low power(~ 10 mW) local oscillator at a slightly different frequency. When the two signals are mixed in the balanced mixer, there is a resulting intermediate frequency. A heterodyne system is, therefore, insensitive to the relative phase between the signal and local oscillator, which is unwanted information anyway. Further advantages to a heterodyne system is its high sensitivity; i.e., the smallest true signal it can discern from the noise present in the device. It can get high sensitivity since one can take advantage of high gain, low noise amplifiers available at typical intermediate frequencies, like 200 MHz. Heterodyne systems have disadvantages also; two oscillators are required, adding to the cost and making frequency stabilization necessary. The difference frequency of the two oscillators must remain stable, during the experiment, which is difficult to do, or the system sensitivity will change.

References for Chapter 2

[1]J.D. Steben, J. Appl. Phys. 43, 1211 (1972).
J.R. Drake, University of Wisc., Ph.D. Thesis 1974, PLP-549.
A.J. Cavallo, University of Wis., Ph.D. Thesis 1975, PLP 628.

[2]J.C. Sprott, E.J. Strait, C.M. Fortgang, J.C. Twichell, R.N. Dexter, and J.D. Barter, High Power Experiments on the Wisconsin Levitated Octupole, Fourth Topical Conference on Radio Frequency Heating, 1981, Austin, Texas.

[3]R.P. Torti, J. Conrad, R. Moyer, and L. Peranich, University of Wis. Status of the Neutral Beam Injectors for the Octupole Upgrade, 1980, PLP-846.

[4]E.J. Strait, Nuclear Fusion 21, 943 (1981).

[5]H.R. Garner, University of Wisc., Large Octupole Gettering Area, 1980, PLP 834.

[6]M. Okabayashi and V. Arunasalam, Nuclear Fusion 17, 497(1977).

[7]H.R. Garner, University of Wis., Digital Multiradian Fringe Shift Interferometer, 1980, PLP-833.

[8]J. Twichell, private communication.

[9]J.C. Sprott, Rev. of Scientific Instruments 39, 1569 (1968).

[10]M.C. Zarnstorff, private communication.

[11]C. Klepper, private communication.

[12]A. Cavallo, Phys. Fluids 19, 394(1976).

[13]R. Cano, A. Bagdasarov, A. Berlizov, E. Gorbunov, and G. Notkin, Nuc. Fusion 9, 1415(1979).

[14]A.P. Biddle and J.C. Sprott, Plasma Physics 23, 679 (1981).

[15]H.R. Garner, Design of Parabolic Microwave Antenna, University of Wis. PLP (To be published).

[16]M.A. Heald, C.B. Warton, Plasma Diagnostics with Microwaves, R.E. Krieger Publishing Company, Huntington, New York, 1978.

[17]H.R. Garner, University of Wisc. Fluctuation Studies with Microwave Scattering in the Wisconsin Levitated Octupole, 1979, PLP 813.

[18]Varian Associates of Canada Limited, Georgetown, Ontario, Canada.

[19]Universal Voltronics Corporation, Mount Kisco, New York.

[20]R.J. King, Microwave Homodyne Systems, Peter Peregrinus Ltd., London, England, 1978.

[21]Baytron Co., Medford, MA.

[22]Tektronix, Inc., Beaverton, Oregon.

[23]LeCroy Research Systems of California, Palo Alto, CA.

[24]Digital Equipment Corporation, Maynard, MA.

[25]M. Kerker, The Scattering of Light and Other Electromagnetic Radiation, Academic Press, New York, NY, 1969.

Fig. 1. The Wisconsin Levitated Octupole toroidal vacuum vessel is pictured here showing the location of much of associated equipment. The toroidal angle increases as you move counter-clockwise from zero, which is located at the poloidal field gap, beneath the laminated core.

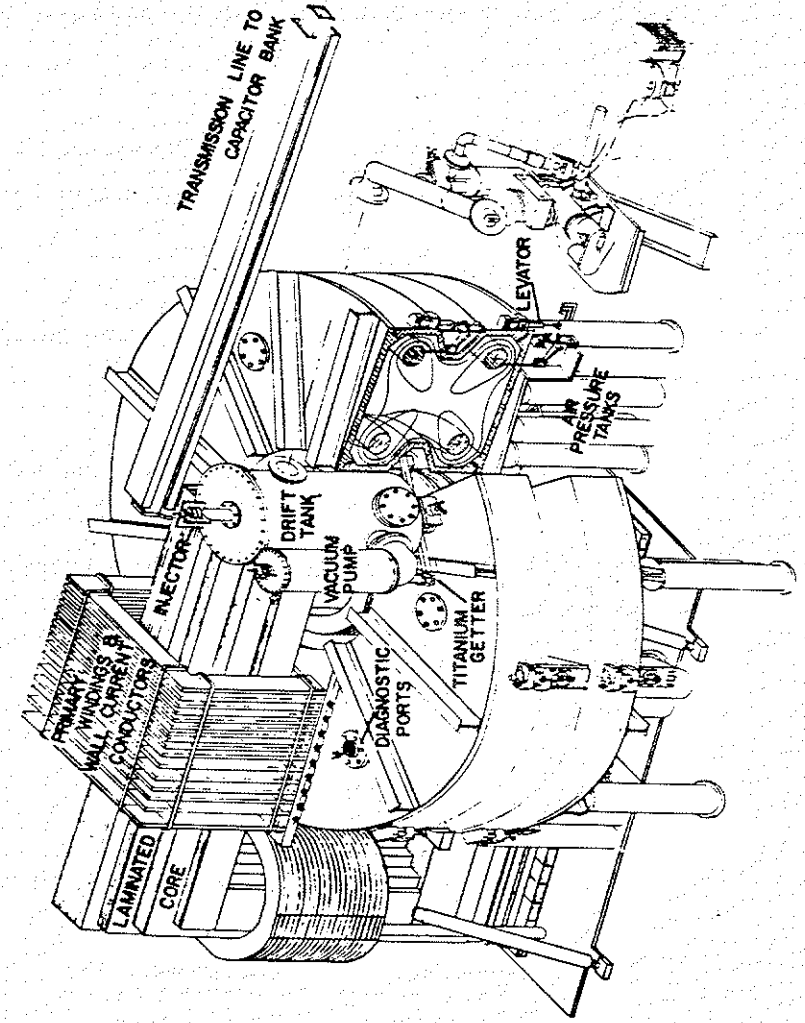

Fig. 2. The positions of the poloidal field lines was shown here for the time, 25 msec after the field capacitor banks are fired. The total flux in the machine at peak field is defined as equal to 10 Dorys. The dashed line is the separatrix field line (ψ = 5.5 Dorys). The dot-dashed line is the critical field line (ψ = 7.2 Dorys). The hoop surfaces are approximately at ψ = 2.5 Dorys. The outside wall surfaces are approximately at ψ = 9.0.

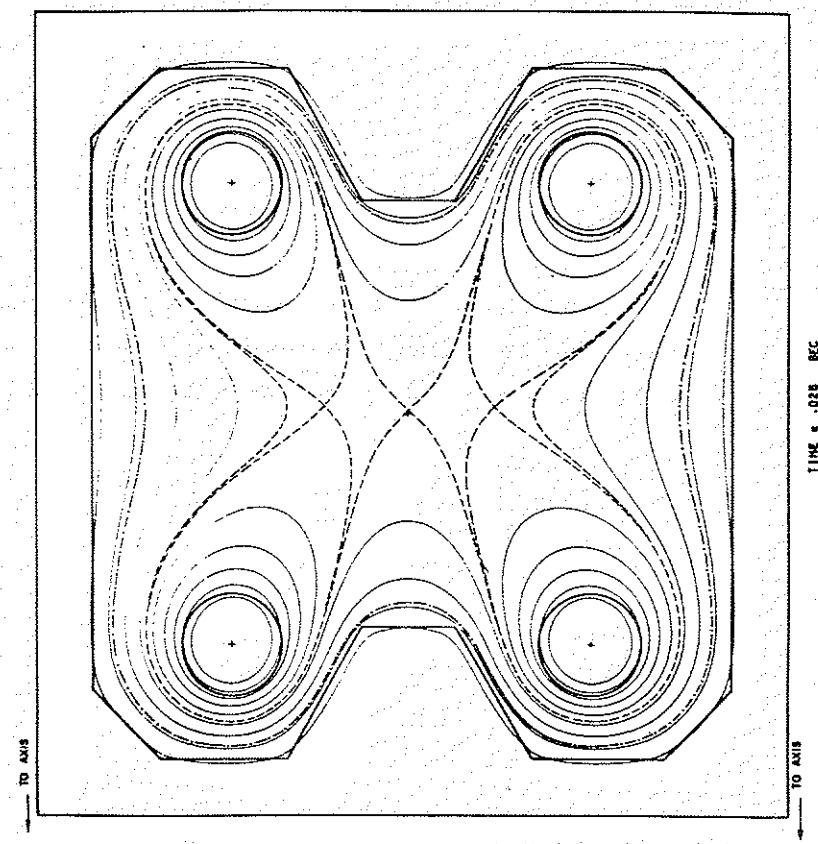

Fig. 3. The poloidal field strength varies as a function of position. The poloidal field strength (in Gauss) is shown here for the poloidal field banks fully charged to 5 kVolts.

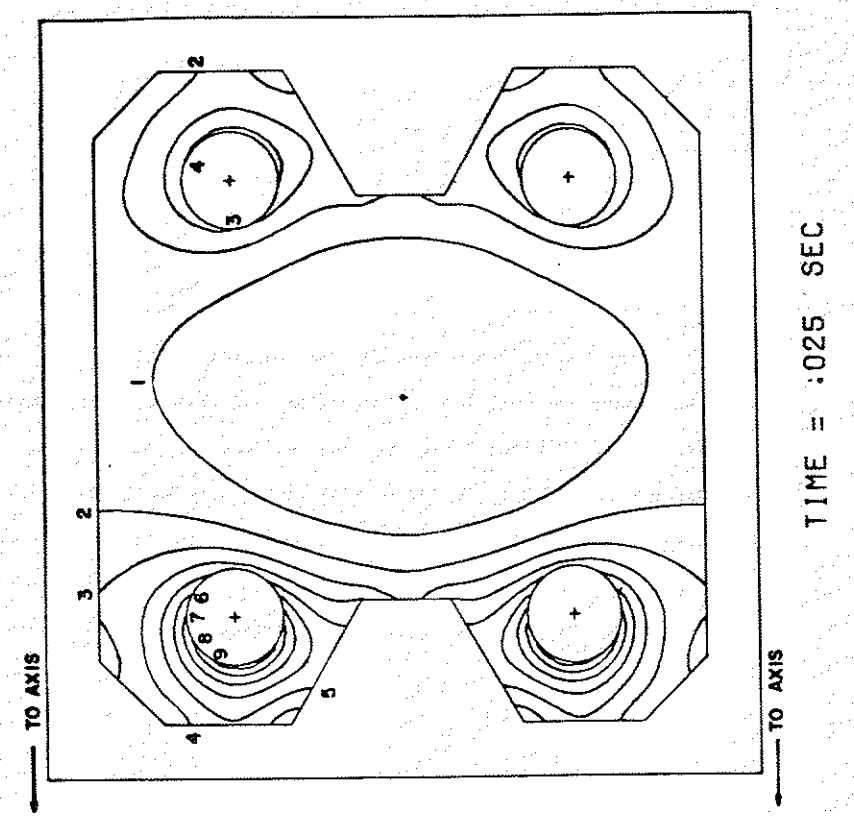

Fig. 4. The regions of k-space which are measureable are shown here as darkened lines. The scattering directions are for $B_T = 0$. The scattering volume located in the absolute-minimum-B region is at $\psi = 4$. The scattering volume located in the average-minimum-B region is at $\psi = 7$.

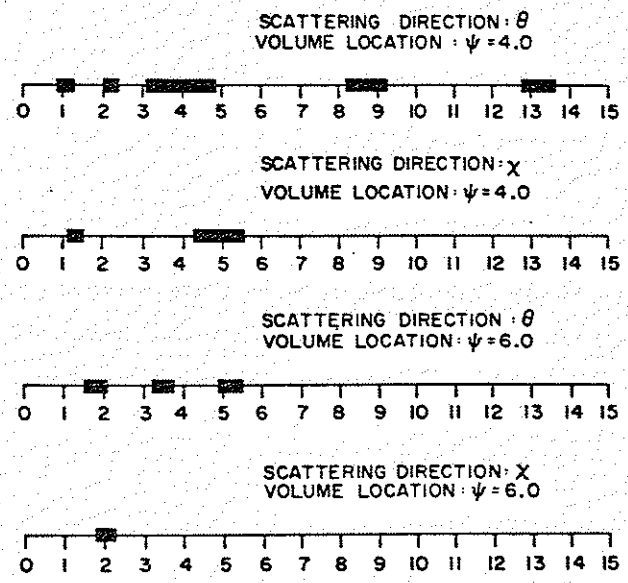

Fig. 5. This view of the placement of the microwave mirror (receiver) placement is shown here, where the perspective is along a major radius, looking towards the axisymetric center of the device.

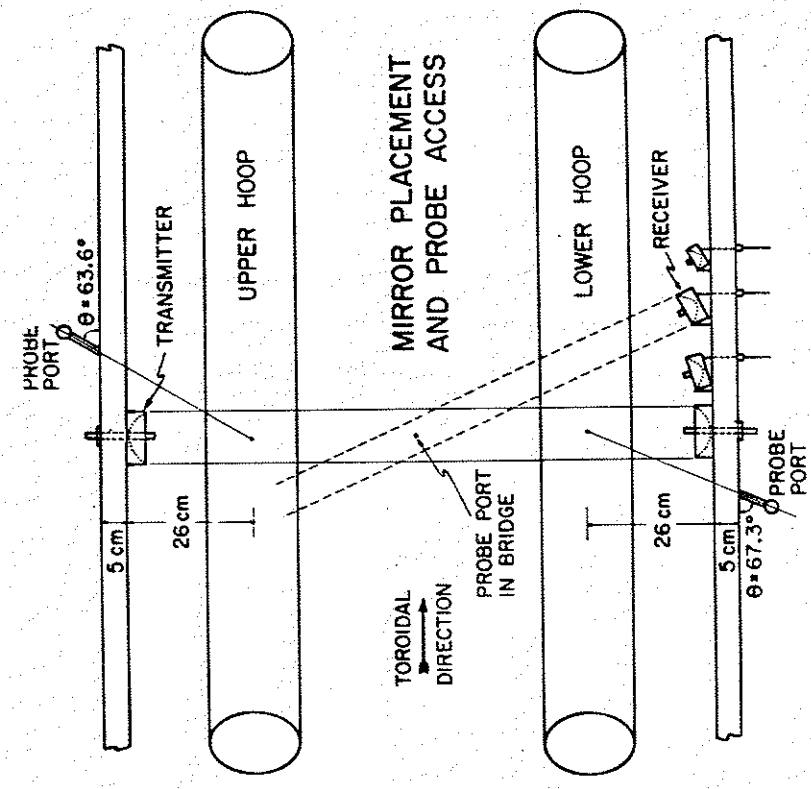

Fig. 6. This is a view of the placement of the microwave receivers, when one is looking from above, along the transmitted beam. Mirror (A) is the receiver for the 70 GHz microwave inteferometer. The remaining mirrors are receivers for the microwave scattering system.

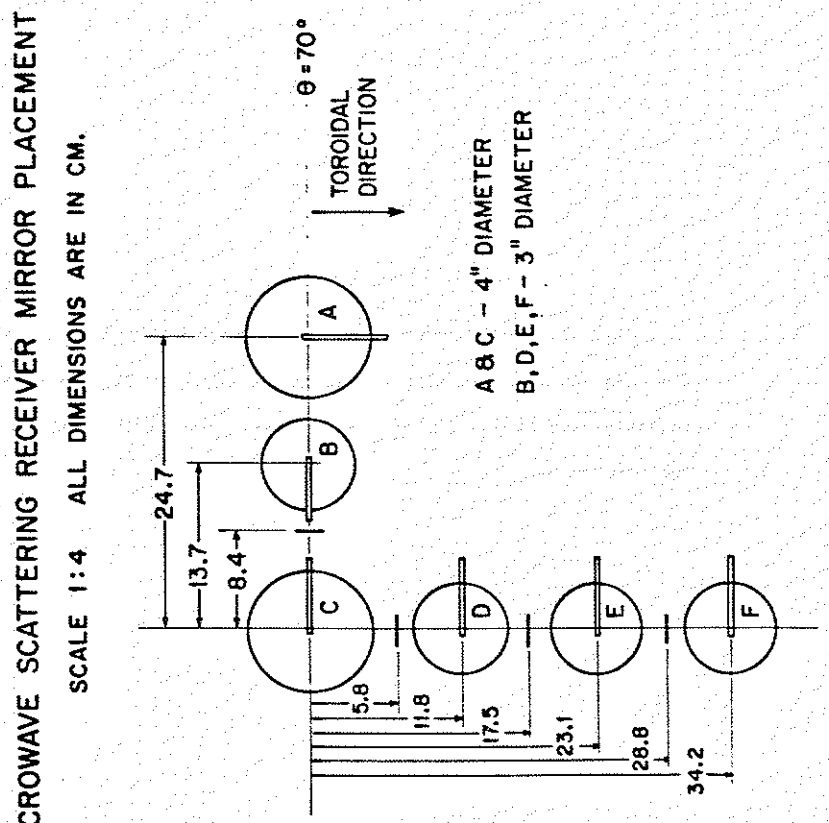

Fig. 7. This figure illustrates how three different wave k's can be measured with one receiver mirror. This is done by adjusting the tilt angle of the receiver beam with respect to the main beam.

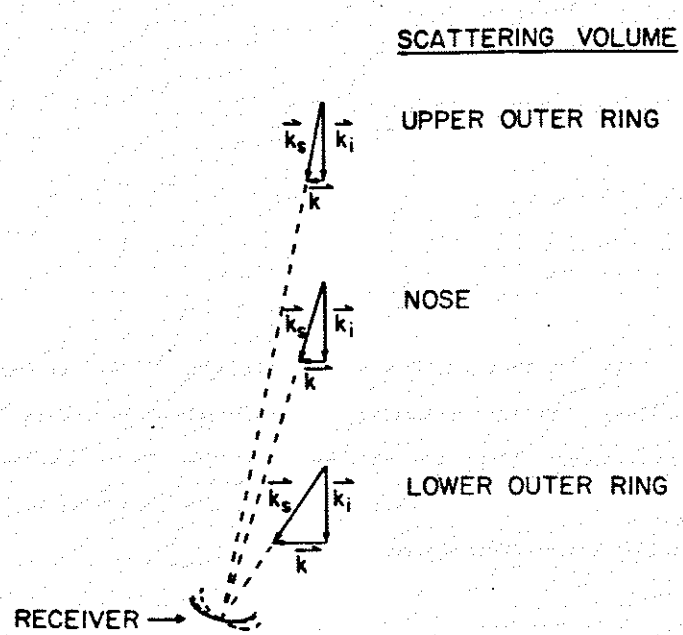

SELECTION OF k VIEWED BY CHANGING TILT ANGLE OF RECEIVER.

Fig. 8. The attenuation and refraction of the microwave beam is less than 10% when the electron plasma frequency is kept below the scattering frequency (35 GHz). Shown here is the time dependent electron plasma frequency for two values of the poloidal field strength, where much of the data was taken. At the different values of $B_{p-average}$ ($\psi = 4$), the plasma trapping varied, thus, the confined plasma temperature and density varied.

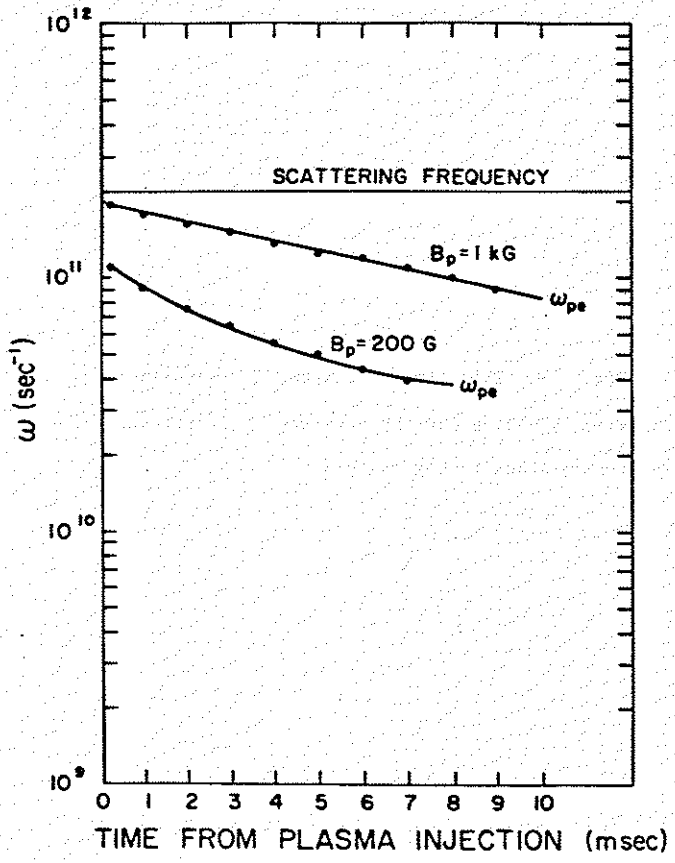

Fig. 9. This is a schematic representation of the microwave plumbing and the electronics plumbing associated with the microwave scattering system.

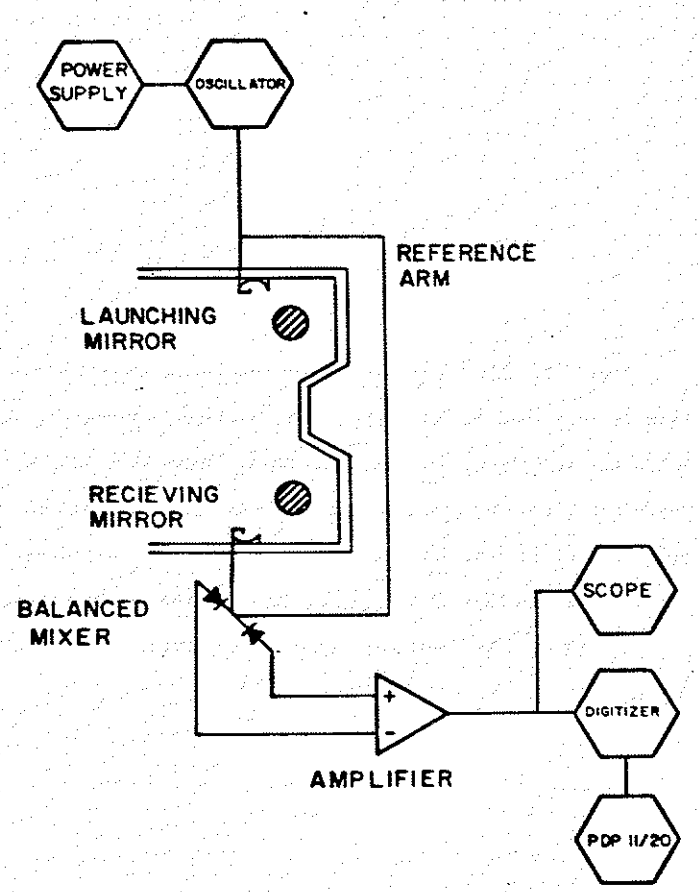

Table 1.

Table 1

Machine Parameters

Major Radius:	140 cm
Minor Radius (typical):	50 cm
Minor Radius of Rings:	8.9 cm
Vacuum Tank Volume:	8.6 m^3
MHD Stable Volume:	7.7 m^3

Poloidal (without power crowbar) and
Toroidal (with power crowbar) Magnetic Fields:

Uncrowbarred Pulse Length:	43 msec
Crowbarred Decay Time:	70 msec

Poloidal Field (at 5 kVolts on Poloidal Field Bank):

	Inner Ring	Outer Ring	Inner Wall (at nose)
Max. B at Surface:	11.6 kG	5.6 kG	8.5 kG
Current:	.46 MA	.25 MA	1.42 MA
Energy: .60 MJ			

Toroidal Field (at 450 Volts on Toroidal Field Bank):

B at midcylinder:	450 G
Energy:	37 kJ

Table 2.

Table 2

Scattering Parameters

Mirror	Direction	Volume Location (Psi)	k (cm^{-1})	Δk (cm^{-1})	Volume Size (cm^3)
B	x	6.0	2.04	.56	113.4
D	θ	6.0	1.76	.56	102.7
E	θ	6.0	3.48	.54	89.9
F	θ	6.0	5.19	.50	73.7
B	x	4.0	1.30	.36	59.38
D	θ	4.0	1.12	.36	59.81
E	θ	4.0	2.2	.35	33.61
F	θ	4.0	3.27	.34	21.89
B	x	4.0	4.91	1.23	49.75
D	θ	4.0	4.23	1.28	42.87
E	θ	4.0	8.67	1.04	59.11
F	θ	4.0	13.21	.82	63.90

Chapter 3

Theory

This chapter is intended to lay the foundation necessary to relate the measurable quantities, the fluctuating density, $\tilde{n}(\omega,k)$, and the time dependent density profile, $n(\psi,t)$, to the perpendicular particle diffusion coefficient, $D_\perp(\psi,t)$. This must be done for each of the areas involved, the interpretation of the microwave scattering diagnostic output, the application of the particle transport equation, and the application of the electron energy transport equation. The theory used in the remaining chapters will be summarized and discussed in the following five sections.

Scattering Power and the Spectral Density Function

This section describes how the microwave scattering signal is related to the density fluctuations present within the scattering volume.

When a beam of electromagnetic radiation with its wave vector described by $\vec{k}_i$, at a frequency, $\omega_i/2\pi = f_i$, is shined at a plasma, some of that power is scattered from coherent density fluctuations which are present.[1] The density flucutations are at a frequency, ω, and have a vector, $\vec{k}$, associated with them.

The orientation of the transmitter and receiver of the microwave beam determines the density fluctuation wave vector which is viewed. The selection rule for scattered k-vector is:

$$\vec{k}_s = \vec{k} + \vec{k}_i \qquad (1)$$

The receiver picks up the power scattered into the wave described by $\vec{k}_s$ and ω_s. The frequency, ω_s, of the scattered wave is determined from a second selection rule:

$$\omega_s = \omega + \omega_i \qquad (2)$$

In this experiment $\omega_i/2\pi = f_i = 35$ GHz and $\omega < 1$ MHz, therefore, $\omega_s \approx 35$ GHz. The frequency of the density fluctuations, ω, is recovered when the incident wave, at frequency, ω_i, is mixed with the received scattered signal. In this experiment, $\vec{k}_i$ was constant and $\vec{k}_s$ was varied to select plasma waves with different $\vec{k}_s$'s to be studied. This scattering diagram is shown in Fig. 7 of Chapter 2.

The power scattered from the incident beam towards the receiver due to the density fluctuations in the plasma can be written in the form:

$$P_s = \int_{-\infty}^{\infty} \int_V P_{in}(r,\theta,z)\, \sigma_e n\, S(k,\omega)\, \Omega_{eff}(r,\theta,z)\, dV \frac{d\omega}{2\pi} \qquad (3)$$

The coordinate system used in the evaluation of equation 3 is cylindrical. It is convenient to use cylindrical coordinates to describe the transmitted and received beams because they are launched and received with parabolic antennae. The coordinate system is oriented such that "z" is along the transmitted beam. This is vertical in the octupole. The radial distance from the center of the beam is "r". The third orthogonal coordinate is "ϑ". The orgin of the coordinate system is located at the center of the scattering volume. The total power scattered (in units of watts) into the receiver is:

$$P_s = \int_{-\infty}^{\infty} P_s(\omega)\, d\omega \qquad (4)$$

The illumination of the scattering volume is done with a transmitter beam at a power of $P_{IN}(r,\vartheta,z)$ (in units of W/m^2):

$$P_{IN}(r,\vartheta,z) = P_T\, G_T(0)\, A_T(r,\vartheta,z) \qquad (5)$$

where P_T is the total power launched, which for this experiment was approximately 25 W. $G_T(0)$ is the normalized transmitted power flux, P(0), at the center of the scattering volume, (in units of m^{-2}):

$$G_T(0) = \frac{P(0)}{P_T} \qquad (6)$$

The antenna gain function, $A(r,\vartheta,z)$, absorbs all the spatial dependences of the beams. The beams launched by the parabolic mirrors have a gaussian weighted power distribution along "r", and are symmetric in "ϑ". There is a finite angular beam spread resulting in a beam which is expanding as it traverses in the "z" direction. The equation for $A(r,\vartheta,z)$ is as follows:

$$A(r,\vartheta,z) = A_o\, e^{-r^2/r_o^2}\, e^{(z-z_o)/z_{BS}} \qquad (7)$$

A_o is a constant which guarantees that $A(0,\vartheta,0) = 1$. The constants, r_o and z_{BS}, are the exprimentally measured beam radius and beam spread. The distance from the mirror focus to the scattering volume is z_o. The effective aperture of the receiver antenna is (in units of steradians):

$$\Omega_{eff}(r,\vartheta,z) = \frac{\lambda_o^2}{4\pi}\, G_R(0)\, A_R(r,\vartheta,z) \qquad (8)$$

$A_R(r,\vartheta,z)$ and $G_R(0)$ refer to the receiver parabolic mirrors and are defined similarly to the tramsmitter quantities, $A_T(r,\vartheta,z)$ and $G_T(0)$. The wavelength of the incident radiation is λ_o, which for this experiment is 8 mm. The Thompson scattering cross section is (in units of m^2):

$$\sigma_e = \frac{e^2}{4\pi\varepsilon_o mc^2} = 7.9 \times 10^{-30}\ m^2 \qquad (9)$$

The quantity which contains the density fluctuation information desired is the spectral density function, $S(\omega,\vec{k})$, (in units of sec) which is defined as:

$$S(\omega,\vec{k}) = \lim_{\substack{V\to\infty \\ T\to\infty}} \frac{1}{VT} \left\langle \frac{\bar{n}(\omega,\vec{k})\bar{n}^*(\omega,\vec{k})}{n} \right\rangle \qquad (10)$$

The mean plasma density in the scattering volume is n. The scattering volume is V. The time over which the observations are being made is T. The Fourier transformed density fluctuation function, $\bar{n}(t,\vec{r})$, is $\bar{n}(\omega,\vec{k})$. This is defined using the equation[1]:

$$\bar{n}(\omega,\vec{k}) = \int_V d\vec{r}\, e^{+i\vec{k}\cdot\vec{r}} \int_T dt\, e^{-i\omega t}\, \bar{n}(t,\vec{r}) \qquad (11)$$

where $d\vec{r}$ is the volume element. The brackets, $\langle\rangle$, represent an ensemble average. The spectral density function will be discussed in more detail shortly; but, first, the final form of Eq. (3), which directly relates the voltage out of the scattering diagnostic to $S(\omega,\vec{k})$, should be given.

In order to absolutely calibrate the system, the quantities P_T, $G_R(0)$, and $G_T(0)$ must be known. In principle, these constants, along with the losses and conversion factors associated with the microwave hardware, are difficult to measure individually. By measuring the response of the microwave scattering system to a target located at $(0,\theta,0)$ in the scattering volume, and equating that to the actual cross section for the target, the total system efficiency can be evaluated. For a target (in our case a metallic sphere) of differential cross section $\sigma_c(\theta)$, Eq. (3) reduces to:

$$P_{SC}(\theta) = P_T \frac{\lambda_o^2}{4\pi} G_T(0)\, G_R(0)\, \sigma_c \qquad (12)$$

This equation along with an equation for the power to output voltage conversion will give the final form of Eq. (3) used in this experiment. This equation for the output voltage is:

$$V_{s,sc} = CP^N \qquad 0 < N < 2 \qquad (13)$$

For the system used, the bias on the microwave diodes was adjusted to make $N = 1$. The proper bias to make $N = 1$ was selected by inserting spheres of different cross sections and measuring the resulting output voltage. Inserting equations (12) and (13) into equation (3) yields:

$$\int_{-\infty}^{\infty} S(\omega,\vec{k})\,\frac{d\omega}{2\pi} = \frac{V_s}{V_{sc}}\,\frac{\sigma_{c(\theta)}}{\sigma_e}\,\frac{1}{n\int_V A_T A_R dV} \qquad (14)$$

The voltage output from the scattering of the density fluctuations is V_s. The voltage output from the scattering system when the sphere is inserted for calibration is V_{sc}. The equation for the differential cross section for a sphere of radius, a, scattering plane polarized electromagnetic waves of wavelength $\lambda > a$, at an angle θ is:

$$\sigma_c(\theta) = \frac{2(4\pi)^5 a^6}{\lambda^4}\,(\cos\theta - \frac{1}{2})^2 \qquad (15)$$

The only remaining portion of Eq. (14) to be evaluated is:

$$\int_V A_T\, A_R\, dV \qquad (16)$$

This volume integral was calculated numerically with the codes, ANTANE and VOLUME, for each scattering volume of interest. A_T and A_R were of the form in Eq. (7), but with the respective z-axis for each of the two intersecting gaussian beams intersecting at the scattering angle, θ_s.

$$\theta_s = \tan^{-1}\left(\frac{k}{k_i}\right) \qquad (17)$$

Now that the overall output and calibration of the diagnostic is understood, the discussion of the spectral density function, $S(\omega,\vec{k})$ can be resumed.

The limiting values of V and T of Eq. (10) will, for this experiment, become the scattering volume and the measurement time. This will place restrictions on the wavelengths and frequencies of density fluctuations which can be measured with the scattering system. The restriction on the volume limits the measurement of fluctuations to wavelengths less than the characteristic lengths describing the volume, i.e. the beam diameter. For this system, therefore, for $\frac{2\pi}{k} = \lambda < 6$ cm, the volume integral over the antennae functions indicates that the measurement of the power scattered from these fluctuations into the solid angle of the receiver is known to within 5%.

The average over the ensemble of possible systems, $\langle\rangle$, becomes equivalent to a time average if the ensemble average is independent of time. This is true if the system is stationary on the time scale of the measurement. For the data presented in this thesis, the system integration time is equal to the total

observation time, T. The shortest observation time used was 1 msec. For the system to be stationary, the observation time (which is integration time in this case) is required to be significantly longer than the correlation time, τ_c, for the fluctuations under study. The correlation time is defined as the time, τ, where the autocorrelation function, $A(\tau)$, is at 50% of it's maximum value. The autocorrelation function is defined as:

$$A(\tau) = \int_T X(t)\, X(t+\tau)\, dt \qquad (18)$$

where $X(t)$ reptesents the temporal data. In Chapter 4, the correlation time for $k_\perp = 4.23\ cm^{-1}$ waves (which were the most powerful) was approximately 10^{-5} sec, which is considerably less than the 1 msec observation time. For all data presented in this thesis $T > \tau_c$. The hardware was designed to measure λ of approximately 5 cm ($k_\perp \sim 1.1$ cm). The fluctuations, with wavelengths long compared to 6 cm, have small scattering angles and fall into the extreme forward angle mirror. Thus, these long wavelength fluctuations can be measured with interferometry methods. The finite length of time over which the measurement is made restricts the frequencies which can be measured to be greater than $f = 1/2T$. For our measurements which span 1 msec, the smallest frequency which can be resolved is 500 Hz. The highest frequency which can be resolved for the 1 microsecond

sampling time, Δ, used is the Nyquist frequency[4], $f_n = \frac{1}{2\Delta} = 0.5$ MHz (for the 1 microsecond sampling time).

The time averaged, Fourier transformed density fluctuation function can be calculated once $S(\omega,\vec{k})$ has been measured. This is done by inverting Eq. (1). If the total level of fluctuations, $\frac{\tilde{n}}{n}$, is desired, Eq. (10) is simply integrated over all wavelength and frequency space:

$$\frac{\tilde{n}}{n} = \left(\frac{VT}{n} \int S(\omega,\vec{k})\, d\omega\, d\vec{k} \right)^{0.5} \qquad (19)$$

The integral over the frequency space is easy, just select the range of frequencies of interest and integrate the periodgram formed when the Fourier time transform of the data was taken. The k-space integral is 3-dimensional and requires some assumptions to be made concerning the mode structure of the density fluctuations, since only a finite amount of k-space is sampled. For example, the data anaylsis indicated that there was a slight k-space anisotropy present (see Chapter 4). This then must be taken into account when this integral is calculated. Only a finite amount of $k_\perp$-space was measured and even smaller portions of $k_\parallel$-space was measured. Thus, the

anisotropy which was measured, for the range over which $k_{\parallel}$ and $k_{\perp}$-space overlapped was assumed to exist over the entire k-space in which the integration was done. Also, to some extent, the data determined the amount of k-space to be integrated over, i.e., fluctuations which resemble vortex cell activity would not be included in the drift wave analysis.

The calculations of $\frac{\tilde{n}}{n}$, $S(\omega,\vec{k})$, and the correlation time were performed using specialized data analysis software called VAMP.[5] VAMP is a language which was designed to analyze data taken with the data acquistion software, DAMP.[6] The data flow schematic is shown in Fig. 1. The programs written in VAMP which were used to analyze the microwave scattering data are listed and discussed in Reference 7.

Particle Transport Equation

The actual diffusion of particles perpendicular to the magnetic field was measured in the Octupole using the profile evolution technique. First, the ion saturation current ($I_s \propto n\,(T_e)^{0.5}$) and the electron temperature (T_e) profiles were measured using probes. The time dependent plasma density profile was then unfolded from this data. Second, these density profiles were compared to theoretical profiles calculated from

numerically solving the particle conservation equation with a computer program. The particle conservation equation:[8]

$$\frac{\partial n}{\partial t} + \vec{\nabla} \cdot D\vec{\nabla} n = S \qquad (20)$$

was solved in multipole coordinates:

ψ = poloidal flux function

λ = magnetic scaler potential

θ = toroidal angle

where:

$$\vec{B}_p = \frac{1}{2\pi}(\vec{\nabla}\psi \times \vec{\nabla}\theta) = \vec{\nabla}\lambda \qquad (21)$$

The particle motion along a field line, $d\ell = B_p d\lambda$, is rapid compared to the perpendicular particle diffusion. For this reason, Eq. (20) can be flux surface (volume) averaged by operating upon it from the left with:

$$\oint \frac{d\ell}{B_p} \qquad (22)$$

The plasma was azmuthally symmetric, so $n = n(\psi)$ only. The source function, S, was calculated in the heat and neutral transport code, TEVOL. See Chapter 6. The neutral particles

refluxing from the walls contributed at most 20% to the refueling of the plasma at any spacial position. This effect was greatest near the plasma boundry. Refueling contributed less than 5% to the total particle balance near the seperatrix volume, where the plasma density maximized. The neutral density maximized near the vacuum vessel wall, where it had a maximum of 2.5×10^{10} cm^{-3}, while the plasma density at the separatrix was 5×10^{13} cm^{-3}. Recombination and particle loss to the internal ring supports was small. The experimentally measured profiles and confinement times in the plasma regimes studied were unaffected when the internal hoops were levitated. This was done by removing the titanium hoop supports during the discharge and repeating the profile measurements. Therefore, because of the above mentioned reasons, the sources and sinks term, S, in Eq. (20) could be ignored.

The perpendicular diffusion coefficient used in the flux surface averaged particle diffusion equation was chosen to be of the form:

$$D_\perp = C_1 n^{\delta_1} B^{\gamma_1} T_e^{\beta_1} + C_2 n^{\delta_2} B^{\gamma_2} T_e^{\beta_2} \qquad (23)$$

In this way, two different scalings and magnitudes of terms contained in $D_\perp$ can be put into the numerical code. The experimental density profiles, when evolved in time, indicated

that a diffusion coefficient was comprised of two parts, one with classical scaling and one with anamolous scaling. This conbination of scalings adequately described the plasma behavior. Classical scaling would have $\delta = 1$, $\gamma = -2$, $\beta = -0.5$. The anamolous vortex diffusion scaling would have $\delta = -0.5$, $\gamma = 0.0$, and $\beta = 0.5$. After putting the above diffusion coefficient into Eq. (23), the final form of the particle diffusion equation, which was solved numerically in the computer program, NEVOL, is:

$$\frac{\partial n}{\partial t} \oint d\lambda + \sum_{i=1,2} [T_e^{\beta_i} C_i \frac{\partial}{\partial \psi} \{n^{\delta_i} (\oint B^{\gamma_i} R^2 d\lambda) \frac{\partial n}{\partial \psi}\}] = 0 \qquad (24)$$

The tabulated functions:

$$\oint d\lambda \ , \ \oint B^{\gamma_i} R^2 d\lambda \qquad \gamma_i = -2,-1,0,1,2 \qquad (25)$$

and the time dependent electron temperature, T_e, were inputs to the program. The initial conditions, i.e. the starter density profiles, used were the experimental density profiles taken at 0.25 msec after plasma injection.

The outputs of NEVOL are the time dependent density profile, the time dependent diffusion coefficent profile, $D_\perp(r,t)$, and the profile averaged particle confinement time.

The profile (volume) averaged particle confinement time, τ_p, is defined as follows:

$$\tau_p = \left(\int_{V_m} \frac{n}{dn/dt} dv \right) / \left(\int_{V_m} dv \right) \qquad (26)$$

where V_m is the total machine volume. The particle confinement time can be calculated from time step to time step for profiles which are changing their shape in time. Therefore, this is not necessarily the confinement time for the normal mode profile decay, where the particle confinement time is not a function of position within the profile.

Vortex Diffusion

This section is intended to justify the choice of the scaling for the anamolous part of the diffusion coefficient which was used in the profile evolution program. Detailed discussions of vortex diffusion theory can be found in References 8, 9, 10, 11, and 12.

J.B. Taylor and B. McNamara[11] expressed the perpendicular diffusion coefficient for thermally excited, 2-dimensional, vortices as:

$$D_{\perp v} = \frac{C}{B} \left(\frac{2T_e}{\varepsilon}\right)^{0.5} \left(\ell n \frac{L}{2\pi\lambda_D}\right)^{0.5} \qquad (27)$$

In Eq. (27), ε is the low frequency dielectric constant, λ_D is the Debye length, and L is the characteristic size of the 2-dimensional vortex cells. For the Octupole plasmas, L is the characteristic machine dimension, which is assumed to be approximately 5 cm, corresponding to the smallest dimension of the cell. For the plasmas under study, $\omega_{pi} \cong 1 \times 10^9$ sec^{-1}, $\omega_{ci} \cong 5 \times 10^6$ sec^{-1}, therefore, the low frequency dielectric constant, $\varepsilon = 1 + \omega_{pi}^2/\omega_{ci}^2$, is much greater than 1. For $\varepsilon \gg 1$, Equ. (27) becomes:

$$D_{\perp v} \propto \frac{1}{B} \left(\frac{T_e \omega_{ci}^2}{\omega_{pi}^2}\right)^{0.5} \propto \left(\frac{T_e}{n}\right)^{0.5} \qquad (28)$$

This is the diffusion coefficient used in the numerical modeling. The magnitude of $D_{\perp v}$ was calculated by Taylor and McNamara for thermally excited vortex cells. If there exists non-thermal fluctuations in the plasma, such as drift waves, which can enhance the vortex cell activity,[12] then, $D_{\perp v}$, as stated above, will underpredict the actual diffusion. The magnitude of $D_{\perp v}$ is enhanced by non-thermal fluctuations in the plasma. The level of these fluctuations can be noted as being

enhanced above thermal by the amount, $\frac{T^*}{T_e}$. T^* was obtained by taking the ratio of the observed magnitude of the diffusion to that calculated from the theoretical vortex diffusion model:

$$T^* = T_i \left(\frac{D_\perp \text{observed}}{D_{\perp v}}\right)^2 \qquad (29)$$

Diffusion Coefficients and Fluctuation Spectra

The microwave scattering diagnostic measures the density fluctuation spectrum, $\tilde{n}(\omega,\vec{k})$. It was desired to calculate the contribution that these density fluctuations made to the particle transport. To accomplish this, the types of fluctuations must be identified so that a relationship between $\tilde{n}(\omega,\vec{k})$ and the perpendicular diffusion coefficient, $D_\perp$, can be found.

Two approaches were used. One is referred to as the "linear drift wave" model. With this model the diffusion coefficient is calculated from the time averaged flux, $\vec{\Gamma}$:[13,14]

$$D_{\perp LDW} = \frac{-\vec{\Gamma}}{\vec{\nabla} n} = \frac{-\langle|\tilde{n}\tilde{v}|_k\rangle}{\vec{\nabla} n} \qquad (30)$$

The second method is labeled the "strong turbulence" model.

This technique estimates the perpendicular diffusion coefficient from turbulence theory:[15]

$$D_{\perp ST} = \left(\frac{a}{2d} \sum_k \frac{\langle|\tilde{v}|_k^2\rangle}{k^2}\right)^{1/2} \qquad (31)$$

where d = system dimensionality, and a = 1 or 2, depending on the choice of temperoral decay assumed for $\langle|\tilde{v}|_k^2\rangle$. If a is chosen to be 1, then no temporal decay is assumed to take place on the time scale of $(k^2D)^{-1}$. A value of 2 for a was used in the calculations in this experiment which indicated the velocity field, $\langle|\tilde{v}|_k^2\rangle$, was damping like exp $(-k^2Dt)$. This value was chosen since the autocorrelation time (calculated in Chapter 4) is approximately equal to $(k^2D)^{-1}$. In both cases, it is necessary to know the velocity-field spectrum of the modes in order to calculate $D_\perp$. It is for this reason that the modes must be identified so that a theoretical relationship between $\tilde{n}$ (which is measured by the microwave scattering diagnostic) and $\tilde{v}$ can be found.

The fluctuation spectra measured in the Octupole appear to have contributions from two types of modes, vortex modes and drift-wave-like modes. (See Chapter 4.) Once the portions of the wavenumber and frequency spectra attributable to each type of mode have been separated, the calculation of $D_\perp$ can be made.

The vortex modes contribute to the low frequency, long wavelength portion or $\tilde{n}(\omega,\tilde{k})$. It has been established in the past[16] that $\frac{\tilde{n}}{n} < \frac{e\tilde{\phi}}{T_e}$, where $\tilde{\varphi}$ is the fluctuating potential However, there exists no direct experimental or theoretical relationship between $\tilde{n}(\omega,\tilde{k})$ and $\tilde{\phi}(\omega,\tilde{k})$. This means that an estimate of the $D_\perp$ attributable to these modes cannot be made from the microwave scattering data.

The high frequency, short wavelength drift-wave portion of the spectrum can be used to calculate a diffusion coefficient since the relationship between $\tilde{n}$ and $\tilde{v}$ is well defined:[13,14]

$$\left(\frac{\tilde{n}}{n}\right)\omega \cong \omega_* \frac{e\tilde{\phi}}{T_e} \tag{32}$$

where the diamagnetic drift frequency is defined as:

$$\omega_* = \frac{-k_\perp C T_e}{eBn}\frac{\partial n}{\partial r} \tag{33}$$

The frequency of each component in the spectrum is ω. Equations (32) and (33) will be used extensively to relate $\tilde{v}$ to $\tilde{n}$ along with:

$$\tilde{v} = \frac{\tilde{E}\times B}{B^2} = \frac{-ik_\perp\tilde{\phi}C}{B} \tag{34}$$

Substituting Eqs. (32), (33), and (34) into Eq. (30) and also allowing for a possible phase shift, δ_k, between $\tilde{n}$ and $\tilde{\phi}$, gives the final form for $D_{\perp LDW}$ used to analyze the microwave scattering data:

$$D_{\perp LDW} = 2\, r_n^2 \sum_k \omega \sin\delta_k \langle|\frac{\tilde{n}}{n}|_k^2\rangle \tag{35}$$

where the density scale length is $r_n = \frac{n}{dn/dr}$. The brackets, $\langle\rangle$, indicate an ensemble average, which is a time average, since the integration time of the measuring system is greater than the correlation time for the modes. Further discussions regarding the use of Eq. (35) is found in Chapter 5.

The second method for estimating the perpendicular diffusion coefficient uses Eq. (31) derived by Salu and Montgomery in Reference 15. Substituting Eqs. (32), (33), and (34) into Eq. (31) yields:

$$D_{\perp ST} = \frac{r_n}{(2)^{0.5}}\left(\sum_k \frac{\omega^2}{k^2}\left(|\frac{\tilde{n}}{n}|_k^2\right)\right)^{1/2} \tag{36}$$

This is labeled the "strong turbulence" diffusion coefficient since it is being applied to data which appeared to indicate that the fluctuations present in the plasma were in the strongly turbulent regime. The turbulence coefficient, η, the energy in the fluctuating field to the thermal energy of the plasma:

$$\eta = \frac{W}{nT_e} = \frac{\varepsilon \langle |\tilde{E}|^2 \rangle}{8\pi nT_e} \tag{37}$$

has a value much less than 1. Even though η is very small, this does not always indicate that the turbulence is not strong.[17] An alternative definition of turbulence strength was used to evaluate the regime in which the data fell. The fluctuations present were defined to be strongly turbulent since the measured fluctuation spectra were broad, i.e., $\frac{\Delta\omega}{\omega} \sim 1$, $\frac{\Delta k}{k} \sim 1$. This indicated that the dispersion relations for the drift-wave-like modes were determined by the interactions between the modes present.

The data taken with the microwave scattering system was analyzed using Eqs. (35) and (36) by a series of programs written in VAMP language. These programs, SCAD, SCAT, CROSS, SPECTRA, etc., are discussed further in Reference 5.

Electron Energy Transport Equation

A technique similar to the one used to evaluate the particle diffusion was employed to study electron heat transport in the Octupole. First, electron temperature profiles were experimentally measured. Second, the electron heat transport was numerically modeled using the code, TEVOL, to solve for the time dependent electron temperature profiles. The electron energy transport equation:

$$\frac{3}{2}\frac{\partial n_e T_e}{\partial t} + \vec{\nabla} \cdot \vec{\kappa}_e \vec{\nabla} T_e = -Q \tag{38}$$

was solved in multipole coordinates. The electron heat transport coefficient is κ_e. The energy source and sink term is Q. The particle and energy transport along a field line is fast compared to the perpendicular transport. This, along with an adequate 1-dimensional model for all the terms in Q, indicated that Eq. (38) could be volume averaged and the problem reduced to 1-D. The electron heat transport coefficient was chosen to be of the form:

$$\kappa_e = C_1 n_e^{\delta} B^{\gamma} T_e^{\beta} \tag{39}$$

Rough calculations, previous to the development of the code,

indicated that the perpendicular heat transport was principally determined by the heat source and sink term, Q. These calculations also indicated that perpendicular heat diffusion would only play a minor role. For that reason, κ_e was chosen to have only one term with classical scaling, since it was expected to adequately model the experiment. Classical scaling of κ_e would have $\delta = 1$, $\gamma = -2$, and $\beta = 0.5$.

Inserting Eq. (39) into Eq. (38) and flux surface averaging yields:

$$\frac{3}{2}\frac{\partial n_e T_e}{\partial t}\oint d\chi + C_1 \frac{\partial}{\partial \psi}\left[n_e^{\delta} T_e^{\beta} \left\{\oint d\chi B^{\gamma} R^2\right\} \frac{\partial T_e}{\partial \psi}\right] = \oint d\chi Q \quad (40)$$

The integrals:

$$\oint d\chi \; B^{\gamma} \; R^2 \qquad \gamma = -1, -2, 0, 1, 2 \quad (41)$$

are tabulated functions of ψ. The sink and source term, Q, was chosen to be of the following form:

$$Q = Q_{ion} + Q_{H_2} + Q_H + Q_{impurity} \quad (42)$$

where:

$$Q_{ion} = 2\frac{m_e}{m_i}\tau_{ei}^{-1}(T_e - T_i)n_e \quad (43)$$

= electron-ion energy exchange

$$Q_{H_2} = R_{H_2}\, n_{H_2} \langle\sigma v\rangle_{H_2}\, n_e \quad (44)$$

= Excitation and Ionization of H_2

$$Q_H = R_H\, n_H \langle\sigma v\rangle_H\, n_e \quad (45)$$

=Excitation and Ionization of H

$$Q_{impurity} = 0 \quad (46)$$

$$R_{H_2} = .9498\, T_e^{1.096}[\exp(11.99\, T_e^{-.738}) - 1.036] \quad (47)$$

$$R_H = \exp(3.37\, T_e^{-1.001})$$
$$[205.7 + 89.19 \exp(-0.00107\, T_e^2)] \quad (48)$$

The equations for Q_{ion}, Q_H, Q_{H_2}, R_{H_2}, and R_H were taken from Reference 18. The Maxwellian averaged ionization rates, $\langle\sigma v\rangle_{H_2}$ and $\langle\sigma v\rangle_H$ are from Reference 19.

The inputs required for the code were the time dependent plasma density profile, the neutral H_2 background pressure (before the discharge), the starter electron temperature profile, the ion temperature profile (if different from the electron temperature profile), and parameters describing the surface conditions of the Octupole.

Ions which are lost from magnetic confinement region strike the wall and either stick there or reflux as fast neutrals. The number of ions lost as a function of time are determined from integrating the time dependent plasma density profile. The neutral transport model which calculates the neutral density profiles, $n_H(\psi,t)$ and $n_{H_2}(\psi,t)$, is discussed further in Chapter 6 and References 20 and 21.

The impurity term was set to zero. The numerical model therefore is limited to plasmas where impurity radiation plays an insignificant role. Developing an impurity transport model and testing its performance was impossible since no diagnostics existed on the Octupole which could measure the impurity density or the power radiated by the impurities. If the ionization and

excitation of H and H_2 and heat diffusion can account for the electron energy loss, this term can be justifiably ignored.

References for Chapter 3

[1]J. Sheffield, Plasma Scattering of Electromagnetic Radiation, Academic Press, New York, 1975. See also L.E. Sharp and S. Mrowka, Microwave Scattering from a Turbulently Heated Plasma, Culham Laboratory, CLM-P-429 (1975). See also H.R. Garner, Univ. of Wisconsin, PLP 813.

[2]M. Kerker, The Scattering of Light and Other Electromagnetic Radiation, Academic Press, New York, 1969.

[3]H.R. Garner, Design of Parabolic Microwave Antenna, Univ. of Wisconsin PLP (to be published).

[4]P. Bloomfield, Fourier Analysis of Time Series: An Introduction, Wiley & Sons, New York, 1976.

[5]Private communication with J. Twichell.

[6]Private communication with K. Karcher.

[7]H.R. Garner, Programs for Analyzing Microwave Scattering Date Using VAMP, Univ. of Wisconsin PLP (to be published).

[8]G.A. Navratil, Ph.D. Thesis, Univ. of Wisconsin, PLP 693 (1976).

[9]H. Okuda and J.M. Dawson, Phys. Fluids 16, 408 (1973).

[10]H. Okuda and J.M. Dawson, Phys. Fluids 16, 1456 (1973).

[11]J.B. Taylor and B. McNamara, Phys. Fluids 14, 1482 (1971).

[12]H. Okuda and C.Z. Cheng, Nuclear Fusion 18, 587(1978). See also PPPL-1316 (1977) and PPPL-1328 (1977).

[13]K. Miyamoto, Plasma Physics for Nuclear Fusion, MIT Press, Cambridge, MA, 1980.

[14]E. Mazzucato, Phys. Fluids 21, 1063(1978).

[15]Y. Salu and D. Montgomery, Phys. Fluids 20, 1(1977).

[16]A.B. Ehrhardt, H.R. Garner, G.A. Navratil, and R.S. Post, Phys. Fluids 24, 1859(1981).

[17]V.N. Tsytovich, Theory of Turbulent Plasma, Consultants Bureau, New York, 1977.

[18]J. Patau, Cross Sections and Rate Coefficients for Inelastic Collisions, Univ. of Wisconsin, PLP - 588(1974).

[19]R. Freeman and E. Jones, Atomic Collision Processes in Plasma Physics Experiments, Culham Laboratory, CLM - R - 137(1974), CLM - R - 175(1977).

[20]H.R. Garner and R.S. Post, Measurement of Low Energy Hydrogen Net Absorption Coefficient on Titanium in the Wisconsin Levitated Octupole, submitted to J. of Vacuum Science.

[21]H.R. Garner, Wisconsin Octupole Heat Transport, Univ. of Wisconsin PLP-844 (1980).

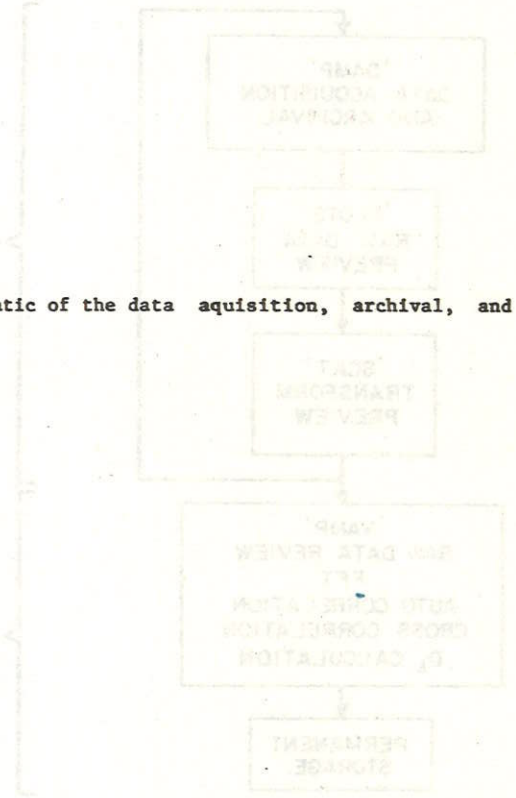

Fig. 1. Schematic of the data aquisition, archival, and analysis software.

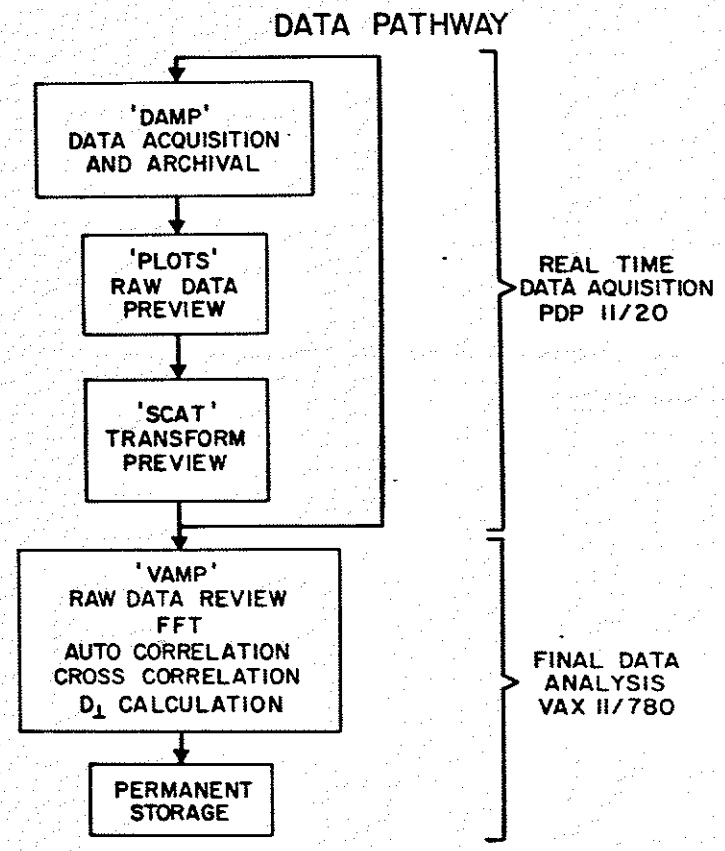

Chapter 4

Density Fluctuations

With the aid of the microwave scattering device and the 70 GHz microwave interferometer described earlier electron density fluctuations have been measured. These fluctuations were measured for a variety of plasma conditions. Since particle confinement times and density fluctuation measurements have been observed to depend on poloidal field strength, various values of poloidal magnetic field were used in the diffusion studies in an attempt to correlate fluctuation activity with particle confinement. Fluctuation spectra were measured for eight values of poloidal magnetic field strength from 200 Gauss to 1 kGauss. Particle confinement time was found to be the longest for the highest value of poloidal magnetic field strength (1 kG), and shortest for the lowest poloidal magnetic field (200 G). Recall from chapter two that many of the basic plasma parameters, such as density and temperature, are significantly different for these two cases as well. These two cases at either extreme were chosen to be documented thoroughly and will be described in this chapter. The effect of magnetic field shear on the measured fluctuation spectra will also be decribed.

Raw data:

Output of the microwave scattering apparatus was directly proportional to the density fluctuations which exist within the scattering volume. Thus, the relative strengths of the density fluctuations can be obtained by inspection of scattering signal. In the raw data, the continuous and small changes in behavior of the fluctuations with time can be seen. These details cannot be examined after the data is transformed into the frequency domain since doing so entails averaging over time. These data are being shown to familiarize the reader with the type of output which emerges from the diagnostic before being processed for use in transport calculations. The transformed data will be discussed in the next section.

Figure 1 shows three channels of computer output of the digitized data presented by the on-line data aquisition system as the data was being taken. Each data channel spans a total of 8 msecs. Each millisecond of which contains 1024 data points. Because of limited screen resolution, only every sixteenth data point was shown. Finer details, which usually represent higher frequency components, are not visually apparent.

This data was taken in the high field ($B_{p\text{-average}}(\psi = 4)$ 1 kG) case, with no toroidal field, in the absolute-minimum-B region of the Octupole. Diagnostic 40 is a recording of the fluctuations at a wavenumber, k_θ, of 2.04 cm^{-1}, corresponding to a toroidal wavelength of 3 cm. Fluctuations at this wavenumber contained little power when compared to other wavenumbers, such as $k_\perp = 4.23$ cm^{-1}. These fluctuations are shown to illustrate that very monochromatic modes were observed; but usually at low frequencies of approximately 1 kHz. Note that the instability was seen to suddenly increase in power, exist for several milliseconds, and then turn off. This was not the case for the bulk of the turbulence observed. That is, the strength of the fluctuations usually changed more slowly with time.

Fluctuations with a wavevector aligned with the poloidal magnetic field are given by diagnostic 41 in figure 1. The wavenumber of these fluctuations is $k_\perp = 1.3$ cm^{-1}. For this wavenumber, the fluctuations were seen to exist from the very beginning of the discharge. Power in the wave appeared to diminish and reappear on time scale of those fluctuations with a similar wavelength in the toroidal direction, given by diagnostic 40. One might conjecture these diagnostics have measured the same instability, which changes its ratio of $k_{perpendicular}$ to $k_{parallel}$ with time. The wavelength of this

fluctuation was approximately 2 to 3 cm, which was very similar to the sizes of potential cells previously observed in the Octupole[1]. The frequency of this mode was also very low, approximately 1 kHz, similar again to the frequency range over which potential (convective) cells have been seen to exist.

One of the most powerful scattering signals was seen at a perpendicular wavenumber of 4.23 cm^{-1}. Data for the first millisecond of the discharge for this wavenumber is shown in Fig. 2. The magnitude of the scattered signal for this wavenumber was an order of magnitude above that observed at the smaller k's just discussed. The fluctuation level was approximately constant for the duration of the experiment (8 milliseconds), as well as for this millisecond segment. Visual inspection indicates that the turbulence was much more broadband, containing significant frequency components far in excess of 1 kHz. The increase in fluctuation activity at higher frequencies for certain wavenumbers will become more apparent when the data is transformed into the frequency domain.

Frequency Spectra

To further characterize the density fluctuations in the Octupole, the time dependent output of the microwave scattering apparatus was transformed into the frequency domain. In this

way the frequencies observed in the measured spectra could be compared with those predicted by the dispersion relations for instabilities which should be present. Drift waves in Octupole plasmas are presumably driven by the omnipresent density gradients. The density gradients present in the plasma are maximized on or near $\psi = 4$ in the absolute-minimum-B regions, and on or near $\psi = 7$ in the average-minimum-B regions. It is at these locations where the drift wave turbulence is expected to have the largest growth rate.

Using digital fast Fourier transform[2] techniques, 1 msec, 1024 word blocks of raw data were transformed into frequency spectra. In this section, Fourier transformed data, which typlifies the spectra observed from shot to shot, will be presented. During the experiments, hundreds of shots were taken for each magnetic field configuration. A number of initial shots taken while the machine was stabilizing for a given set of operating conditions were ignored. Since only two balanced mixers were available to measure scattered power, but twelve different k's were measured to complete an experiment, a minimum of six shots for each different condition were necessary. Furthermore, for each k, at least ten "good" shots were necessary obtain a confidence level for the Fourier transform of 90%. This confidence level means that each component in the final periodogram (spectrum) approaches the true Fourier

transform spectrum for infinitely large data set to within 10%. In this way, the statistical uncertainties were reduced. To construct this final periodogram, the Fourier transforms from ten shots were averaged together. During the course of an experiment, only "good" shots, whose gross plasma parameters (separatrix density, total radiated power, oxygen III light, hydrogen beta light) fell within certain accepted norms, were retained. The accepted norm for the separatrix density was that a shot had to reproduce the time integrated density (1 msec < T < 10 msec) to within 10% of the time integrated density of a set of averaged, normalization shots. The remaining diagnostics were visually inspected on each shot. If their magnitude or temporal behavior deviated noticably from those in the normalization shots, then the data from that shot would be rejected. The deviation in the behavior of the plasma from shot to shot was caused by the abnormal behavior of the plasma source (gun).

The spectra which are shown here are not averaged spectra. Each spectra is a the three-point-smoothed transform which most closely resembles (in total power) the ten shot averaged spectra. While it is indeed true that the ten shot average more closely resembles the true spectrum of any given shot, there are statistically significant peaks which are washed out when averages are taken. Shot to shot variations in plasma

parameters cause minor shifts in spectral components, thus, significant peaks tend to be lost in averaging. In calculating the total fluctuation level, which is an integral calculation, the averaged spectrum was used.

The frequency spectra for each wavenumber were different, some k values had broader spectra. In general, as the field configurations were varied, the shape of the spectra for each k remained the same, but the magnitude of each frequency component was changed. The only spectra shown here are for the absolute-minimum-B region of the Octupole, where much more of k-space could be viewed by the microwave scattering system than in the average-minimum-B region. It should be noted that the frequency spectra for the corresponding k's which could be viewed in both regions were similar in shape and magnitude. It was therefore assumed that the character of the fluctuations could be understood by inspecting the nature of the frequency and wavenumber spectra for the scattering volumes which lie on the ring side of the separatrix, or absolute-miminum-B region. Also, ion saturation current and floating potential fluctuations were measured with probes in front (in the bridge region) and behind the rings (in the scattering volume). Although the fluctuations in front and behind the rings were not totally correlated, the fluctuation levels as indicated from the probe data were the same to within our ability to resolve them.

The oscillating magnetic field components of the fluctuations were measured with B-dot and Hall probes. The magnitude of the magnetic field oscillations, $\frac{\tilde{B}}{B}$, was less than 0.1%, much less than $\frac{\tilde{n}}{n}$. The magnetic field fluctuations were not correlated with $\tilde{I}_s$, $\tilde{V}_f$, or $\tilde{n}$. This indicates that all the fluctuations measured were predominantly electrostatic, even though the plasmas had a finite beta (β to 8%).

The fluctuations shown here are measured in the lab frame.

The first set of spectra shown in Fig. 3 are for a poloidal field strength of 1 kG and no toroidal field. These spectra were calculted from the data taken from 0.5 msec to 1.5 msec after plasma was injected. In can be seen in Fig. 3 that the spectral density function, S(f,k), which was calculated from the transform, peaked at or near the lowest frequency measurable by these techniques, 1 kHz, for all k_i's. The spectra were seen to die off exponentially at higher frequency. Recall that the bandwidth of the scattering system is set to 1 MHz by amplifier limitations, and thus no measurements were made above the 1 MHz frequency. Although the spectra pictured extend out to only 250 kHz, measurements were made out to 1 MHz for all experimental configurations to confirm that no significant fluctuations existed between 250 kHz and 1 MHz.

Only in the $k_i = 4.23 cm^{-1}$ was there statistically significant power in the spectrum out to 150 kHz. The $k_i = 4.23\ cm^{-1}$ spectrum is shown as a function of time in Fig. 4. This turbulence exhibited behavior which identified it most probably a drift wave. The drift frequency, calculated from the reduced data, $\omega_*^e = 5 \times 10^3\ sec^{-1}$(1 msec), is shown in Fig. 5, along with other relevant frequencies. The collisionless drift mode, the collisional drift mode, and the trapped electron mode were likely candidates for this type of drift instability for this parameter regime, $n > 10^{12}\ cm^{-3}$, $0.2\ eV < T_e, T_i < 30\ eV$. The electron mean free path is at most 25 cm for all the plasmas that were studied. The connection length between poloidal mirrors in the Octupole is about 100 cm. Since the connection length was greater than the electron mean free path, this indicated that the plasma was collisional, and that the trapped particles could not execute a complete bounce motion before having a collision. For these reasons, the collisional drift wave, and not the collisionless drift wave or the trapped electron mode, is expected to be present. The normalized growth rate can be calculated for the collsional drift mode using the following equation:[5,6]

$$\frac{\gamma}{\omega}\Big|_{\text{collisional}} = \frac{k_\parallel^2}{k_i^2}\frac{\Omega_e^2}{\omega_*^e}\frac{m_e}{m_i}\frac{1}{\nu_{ei}} \qquad (1)$$

where:

$$k_{\parallel} = \frac{2\pi}{L}, \; L = \text{Field line length} = 50 \text{ cm} \qquad (2)$$

For the first msec after plasma injection, for the high field cases, $B_{p\text{-average}}(\psi = 4) = 1$ kG, the collisional drift mode growth rate was maximum, with $\frac{\gamma}{\omega} \simeq .55$. For all plasmas that were studied, the normalized growth rate was at least 0.05. The total fluctuation level, $\frac{\tilde{n}}{n}$, was found not to be proportional to the linear collisional growth rate, calculated using Equ. (1) above.

At 1 msec into the shot, the ion temperature was 10 eV, which was used to calculate the ion gyroradius, $\rho_i = .3$ cm. It was seen that $k_\perp \rho_i \simeq 1$ at $k_\perp = 4.23$ cm^{-1}.

The turbulence was broad band and doesn't follow a linear dispersion relationship. The half-width-half-max, $\Delta\omega$, of the spectra was greater than the center frequency, $\frac{\omega}{2\pi} = f \simeq 1$ kHz, principally because the turbulence peaked at such a low frequency. The data and calculations for the $B_p = 1$ kG case will be shown, they are representative of data at all magnetic field strengths. The spectral width, $\Delta\omega$, was greatest for $k_\perp = 4.23$ cm^{-1}, as shown in Fig. 6. Shown in Fig. 7 is the

autocorrelation function of the data in Fig. 1, from which the correlation time, τ_c, can be read.

The frequency spectra retained their shape as a function of time during a discharge and spectra continued to peak at low frequencies. The width of the spectra changed slightly during a discharge. This effect was most pronounced for turbulence with wavenumber, $k_\perp = 4.23$ cm^{-1} (Fig.8). Note that the spectral width is a minimum at 5 msec into the discharge. This data is compared to the correlation time calculated from the autocorrelation function, as described above. As expected $\tau_c \simeq \frac{1}{\Delta\omega}$. However, the total power ($S_k = \int S_k(\omega)d\omega$) in the spectrum for this wavenumber ($k_\perp = 4.23$ cm^{-1}) continued to increase. In general, the frequencies at which instabilities contained within the oscillating spectrum varied, but in such a way as to maintain the total power at a set level. That is, at a given time, the spectral width was different from other times but the magnitude of the components still existing in the spectrum were excited to the appropriate level to keep S_k equal to a constant. The total fluctuation level for a given wavenumber, therefore appears to be set by the instantaneous experimental conditions, B_p, n, and T_e.

Receivers viewing fluctuations with a wavevector (k_χ) aligned along B have been used to determine the behavior of the turbulent spectra—in particular the distribution of power in all of the k-space and not just the power in $k_\perp$ space. There appears to have been an anistropy between the total fluctuation level for the k_χ values that were measured (k_χ = 2.04 cm^{-1}, k_χ = 1.30 cm^{-1}, k_χ =4.91 cm^{-1}), and the nearest $k_\perp$ values ($k_\perp$ = 2.2 cm^{-1}, $k_\perp$ = 1.12 cm^{-1}, $k_\perp$ = 4.23 cm^{-1}). This anisotropy,

$$\frac{\int S_{k_\perp}(\omega)d\omega}{\int S_{k_\chi}(\omega)d\omega} \simeq (0.5 \text{ to } 0.8) \qquad (3)$$

was in the low frequency (f < 5 kHz) portion of the spectra. Comparing the higher frequency portion of the spectra indicates that the turbulence level is constant for both k_χ and $k_\perp$.

The description of the frequency spectra for the case discussed above, B_p = 1 kG, B_T = 0 G, also represents the behavior of the turbulence for all other field configurations studied, with and without toroidal field. There were only a few differences which will be mentioned here. First, the frequency spectra for each k component retained the same shape; i.e., power falling off exponentially with frequency, as the poloidal

field strength was varied. For example, the frequency spectra, S(f), for a lower poloidal magnetic field value; B_p = 200 G, B_T = 0 G, is shown in Fig. 9. However, the magnitude of every frequency component at each measured value of k varied inversely with $B_{p\text{-average}}$. For completeness, the frequency spectra at B_p 200 G for $k_\perp$ 4.23 cm^{-1} as a function of time after plasma injection is shown in Fig. 10. Figure 11 presents the time behavior of the characteristic plasma frequencies for the B_p 200 G. Figures 9, 10, and 11 should be compared to Figs. 3, 4, and 5. Second, the addition of toroidal field modified the amount of "apparent" k-space anisotropy. It should be remembered though that the microwave receivers were mounted in the toroidal and radial directions in the vacuum vessel, which for poloidal field-only cases, is the perpendicular and parallel directions, respectively. As toroidal field was added and the average pitch of a field line was changed, the receivers were no longer correlated with purely the perpendicular or parallel parts of k-space. So, although the data emerging from the scattering system indicated slight changes in k-space anisotropy, once this data were corrected for the change in pitch of a field line, the anisotropy appeared to be independent of toroidal field strength.

Wavenumber spectra

By integrating the spectral density function, S(f), over all frequencies, the total spectral power for a given wavenumber at a given time was calculated. At each 1 msec window in time, the 10-shot averaged frequency spectra for each value of k was integrated to obtain the wavenumber spectra, S(k).

The behavior of S(k) as a function of time can be seen in Fig. 12 for $B_{p\text{-average}} = 1$ kG. Note that the wavenumber spectra peaked at $k_\perp = 4.23$ cm^{-1} for all times. The wavenumber spectra exhibited a minimum at $k_\perp = 3.27$ cm^{-1}. The spectra then rose again as k approached zero; that is, for long wavelength modes. This was also observed for $B_{p\text{-average}} = 200$ G spectra, which is shown in Fig. 13.

When toroidal field was added, and the resulting spectra corrected for field line pitch, the wavenumber spectra was found to be the same as the no toroidal field case to within 10%. The mirrors mounted in the Octupole receive scattered power in the toroidal (k_θ) and the radial (k_r) directions. With no toroidal field these directions correspond to the $k_\perp$ and the $k_\parallel$ directions, respectively. When toroidal field is added this direct relationship no longer exists. A k-space anisotropy existed in the no toroidal field case, as indicated by a difference in the magnitude of the scattered power received in the two sets of mirrors, one in the k_θ direction, and one in the

k_r direction. This anisotropy changed as the toroidal field was added in such a way as to indicate that the vectors $k_\perp$ and $k_\parallel$, associated with the density fluctuations, together were rotating relative to k_θ and k_r, associated with the receiving directions. This is also precisely the manner in which the field line (at $\psi = 4$ in the scattering volume) was rotating with respect to the poloidal plane. Once the power distribution in the k_θ and the k_r mirrors was unfolded to represent $k_\perp$ and $k_\parallel$ again, the wavenumber spectra and total fluctuation levels were found to be the same with toroidal field as without toroidal field.

In calculating the total fluctuation levels described in the next section, the wavenumber spectra was integrated over all k values measured. However, calculation of the diffusion coefficients, which also involved an integration over wavenumber, utilized only the portion of wavenumber space between $k_\perp = 3.27$ cm^{-1} and $k_\perp = 13.21$ cm^{-1}. There appeared to be clearly two sections to the wavenumber spectra. The section from $k_\perp = 0$ cm^{-1} to $k_\perp = 3.27$ cm^{-1} was identified as non-drift wave like turbulence since the wavelengths involved were large and were tentatiely identified at density fluctuations associated with vortex (convective) cell structures thought to exist in these plasmas. Since the second region of the wavenumber spectra centered on $k_\perp = 4.23$ cm^{-1} had characteristics of drift wave like turbulence and was obviously

distinctly separated from the long wavelength portion of the k-spectra, only this portion of the spectra was used to calculate the diffusion coefficients presented in the next chapter.

Total Fluctuation Level

The total fluctuation level, $\frac{\tilde{n}}{n}$, was calculated by integrating the spectral density function, S(f,k), over all frequency and wavenumber space. The integration over frequency space is easily done, and it was quite clear as to the range over which the integration was to be done. The frequency range chosen to represent the drift wave portion of the fluctuation spectrum was from 1 kHz to 250 kHz. Recall, no power existed in any of the spectra out past 250 kHz. The k-space integral was much more difficult to perform. There are two coordinate directions perpendicular to $\vec{B}$, $k_{\perp\theta}$ and $k_{\perp r}$, and there is one coordinate direction parallel to $\vec{B}$, k_χ. In this experiment, fluctuation measurments were made with wavenumbers oriented in the θ and the χ directions. It was assumed that the turbulence was isotropic in the perpendicular plane, $k_{\perp\theta}$ and $k_{\perp r}$. When other microwave scattering experiments have measured the $k_{\perp\theta}$ and the $k_{\perp r}$ components of the fluctuations they have found them to be isotropic.[4] The k_χ-space portion of the k-space integral must

also be done. We have data from the experiment which tells us how to do the integral. The data from the two k_χ's, which we measure in the absolute-minimum-B region of the Octupole (ψ = 4), indicated that the turbulence extended out to at least $k_\chi = 4.91\ cm^{-1}$. At that k_χ, the turbulence level was 1.25 to 2 times the level in the corresponding perpendicular wavenumber, $k_{\perp\theta} = 4.23\ cm^{-1}$. The frequency spectra of the fluctuation data taken at $k_\chi = 4.91\ cm^{-1}$ had the same shape as the $k_{\perp\theta} = 4.23\ cm^{-1}$ fluctuation data. Therefore, it appears as though the fluctuations present are propagating in a direction which has a large parallel component. From this data it was assumed that the k_χ portion of the wavenumber spectrum has the same shape as the $k_{\perp\theta}$ spectrum (see Figs. 12 and 13 for example). but at a different magnitude. Therefore, the k-space was much more isotropic than one would expect from linear drift wave theory. The scattering experiments on FM-1 saw similar results, when they measured both $k_{\perp\theta}$ and k_χ portions of the spectra.[4] What is normally expected is that the $k_\parallel$ portion of the spectrum would be very small in order to keep $v_{ti} < \frac{\omega}{k_\parallel} < v_{te}$, and thus the Landau damping of the modes small. Instead, we see the parallel phase velocity of the turbulence, $v_\phi = \frac{\omega}{k_\parallel}$, lies in the middle of the ion velocity distribution function, $\frac{\omega}{k_\parallel} < v_{ti} < v_{te}$. Other scattering experiments done on tokamaks have never measured the $k_\parallel$ (which in the Octupole is k_χ) portion of the wavenumber spectrum, and

have, instead, assumed that the amount of k_ξ-space necessary to properly do the integral was set by some other means, such as setting the bounds on k_ξ through, $v_{ti} < \frac{\omega}{k_\xi} < v_{te}$.[6,7] Our results indicated that this assumption is questionable, at least to the extent that the turbulence found in tokamaks is similar to that found in the Octupole. Surko, Slusher, and Mazzucato did the k-space integral, setting the bounds on the k_ξ integration using linear drift wave theory, and got small values of $\frac{\tilde{n}}{n}$, only a few percent in the centers of ATC, PLT, and Alcator A.[5] If we were to do the k-space integral in a similar manor, ignoring the k_χ results, then the our calculated values of the fluctuation level would also be only a few percent. Correspondingly, the diffusion attributable to the drift wave portion of the spectrum would be less than that stated herein.

It was found that the total fluctuation level rose continuously during the discharge at high magnetic fields, B_p = 1 kG (Fig. 14). However, $\frac{\tilde{n}}{n}$ was seen to reach a maximum of 60% at 4 msec into the shot, after which $\frac{\tilde{n}}{n}$ declined, for the low field cases (B_p < 500 G). This is best seen for the lowest poloidal magnetic field strength of 200 G (Fig. 15). It is not understood why the fluctuation level increased during a shot. This is especially a concern since the density gradient, which is the driving force for the drift wave turbulence, relaxed as time progressed during a shot. The mean plasma density, n,

decreased with time. Some insight might be gained by looking at $\tilde{n}$, the total amount density fluctuation, instead of $\frac{\tilde{n}}{n}$. Shown in Fig. 16 is the quantity $\tilde{n}$ as a function of time. For B_p-average of 1 kG, $\tilde{n}$ was constant ($\tilde{n} \sim 6 \times 10^{11}$ cm^{-3}) through the first 5 msec after plasma injection which may indicate that $\tilde{n}$ was at a saturated level. In the B_p = 200 G case, $\tilde{n}$ peaked at 6×10^{11} cm^{-3} at 3 msec. Indeed, for all plasmas investigated, $\tilde{n}$ never exceeded 7×10^{11} cm^{-3}.

References for Chapter 4

[1]A. B. Ehrhardt, Ph.D. Thesis, University of Wisconsin, 1980.

[2]P. Bloomfield, Fourier Analysis of Time Series: An Introduction, Wiley, 1976.

[3]A. A. Rukhadze and V. P. Silin, Soviet Physics Uspekhi 11, 659(1969).

[4]M. Okabayashi and V. Arunasalam, Nuclear Fusion 17, 497(1977).

[5]R. E. Slusher and C. M. Surko, Phys. Fluids 23, 472(1980). See also E. Mazzucato, Phys. Fluids 21, 1063(1978).

Fig. 1. Diagnostics 40 and 41 are examples of data taken in a single shot with the microwave scattering system. Diagnostic 42 is the ion saturation current measured at the center of the scattering volume. This data was displayed by the on-line data aquisition system.

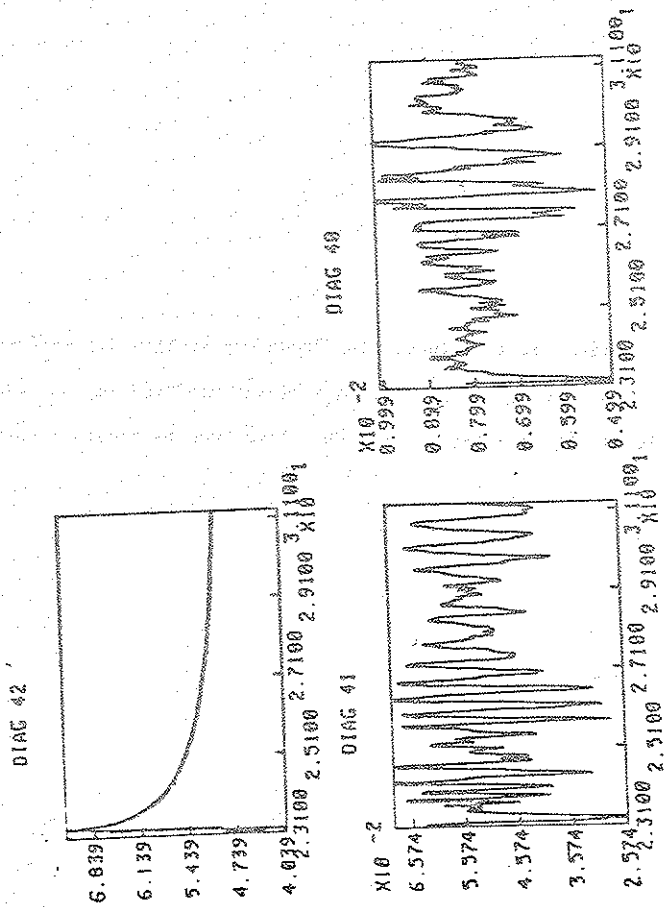

Fig. 2. The magnitude of the scattered signal corresponding to $k = 4.23\ cm^{-1}$ is shown here for 1 msec of data. The plasma was injected at 23 msec. The units on the scattered power, P(t), are arbitrary.

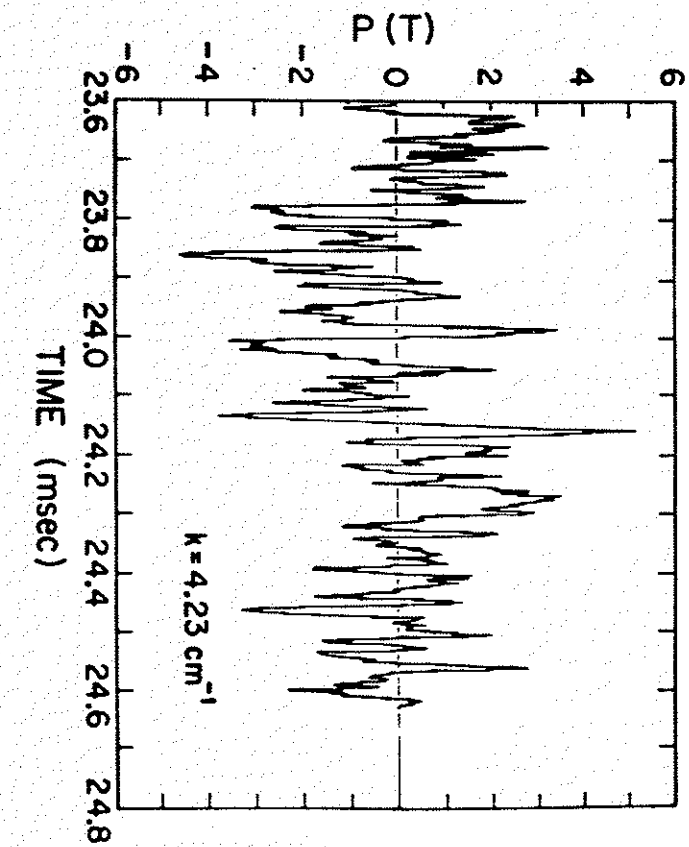

Fig. 3. The fluctuation frequency spectra for various k's are shown in this figure for the plasma confined in an average poloidal field strength of 1 kG. There was no toroidal field.

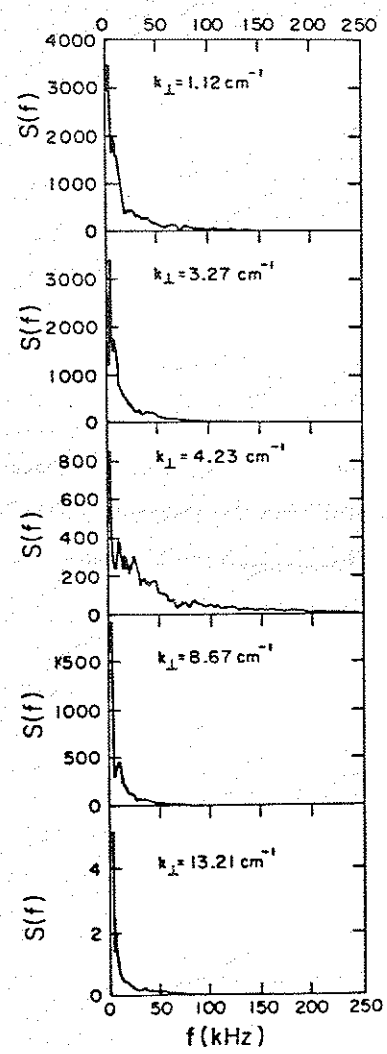

Fig. 4. The time dependence of the fluctuation spectra for $k = 4.23\ cm^{-1}$, which is the k value which had the most power, is shown here for the $B_{P\text{-average}}(\Psi = 4) = 1$ kG case.

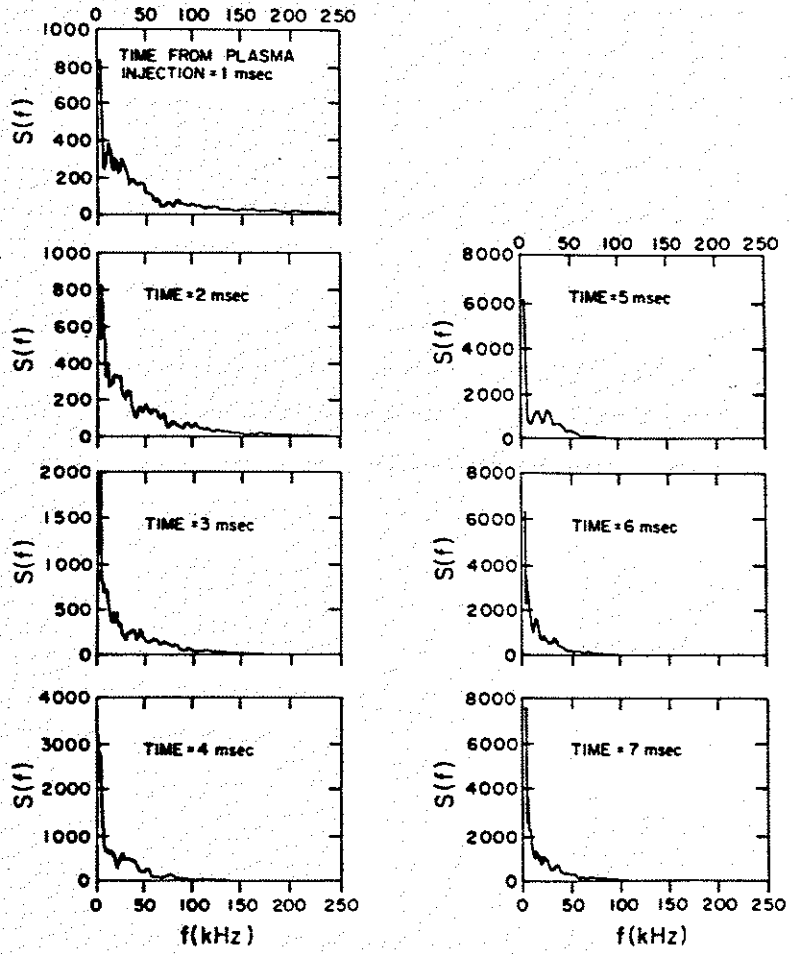

Fig. 5. The time dependent characteristic plasma frequencies calculated from the measured plasma parameters is shown here for the $B_{p\text{-average}}(\psi = 4) = 1$ kG case.

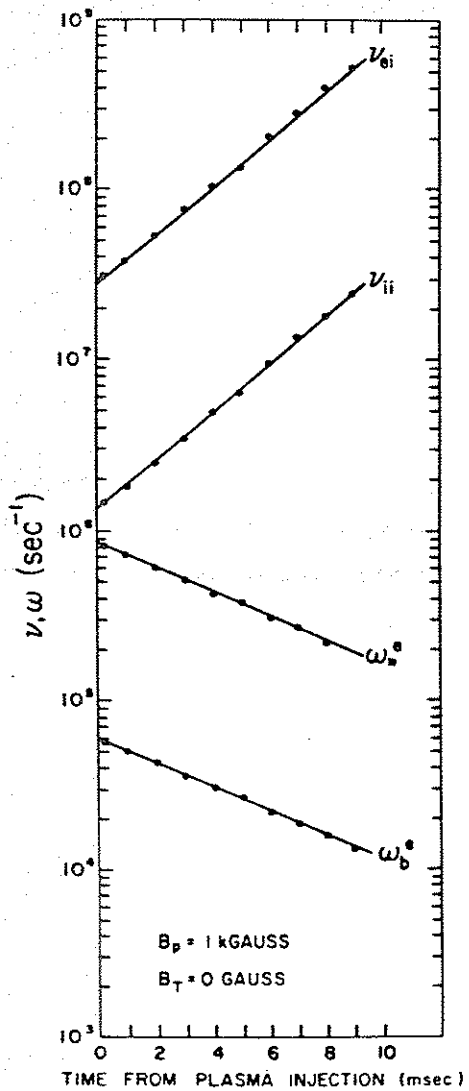

Fig. 6. The spectral width, $\delta\omega$, is maximum at $k = 4.23$ cm^{-1}. The spectral width is taken directly from the frequency spectra (full width at half maximum).

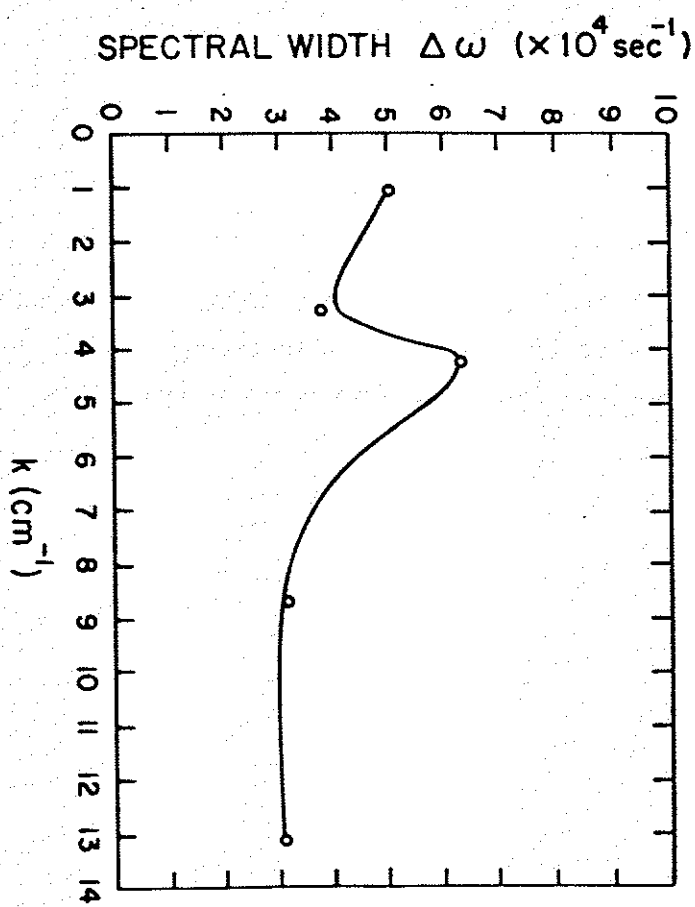

Fig. 7. The autocorrelation function of the raw data in Fig. 1 is shown in this figure. The autocorrelation time (taken at $A(\tau) = 0.5$) can be seen to be 0.1×10^{-4} sec.

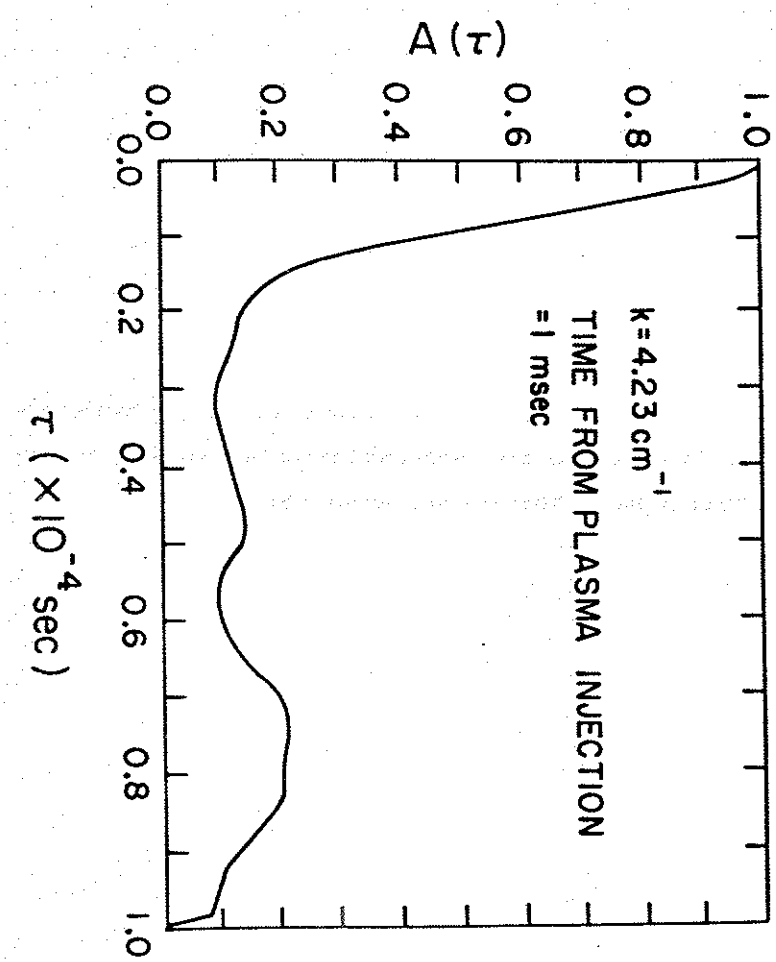

Fig. 8. The autocorrelation time, and the inverse of the spectral width, are compared here as a function of time after plasma injection, for the $B_{p\text{-average}}(\psi = 4)$ case.

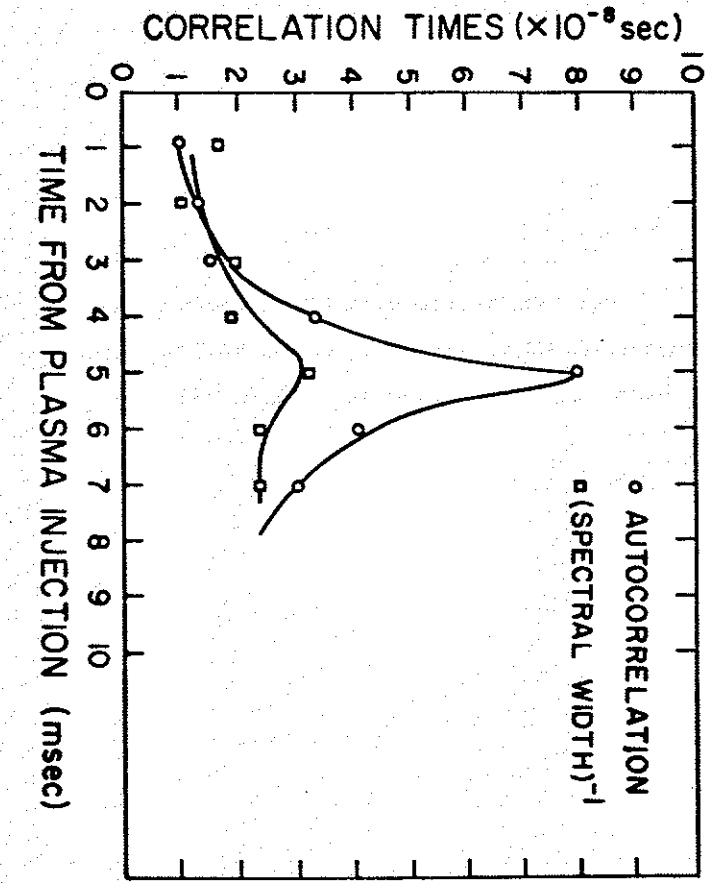

Fig. 9. The fluctuation frequency spectra for various k's are shown here for the plasma confined in an average poloidal field of 200 G. There was no toroidal field.

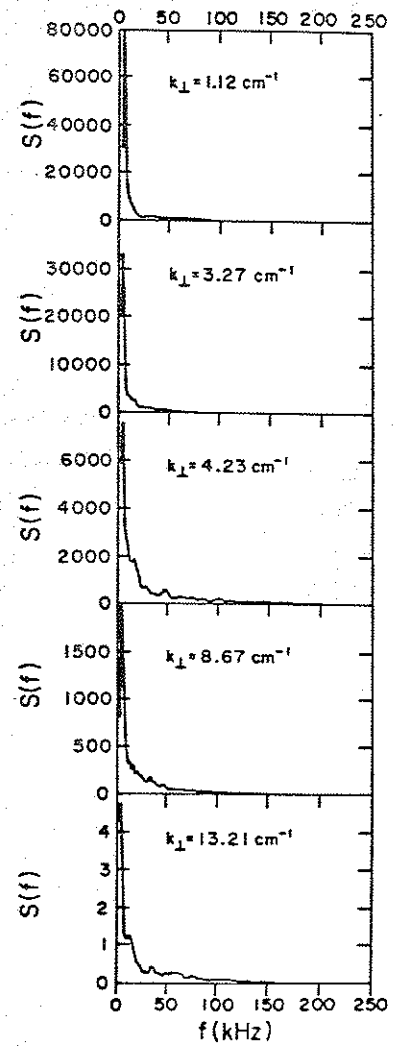

Fig. 10. The time dependence of the fluctuation spectra for k = 4.23 cm^{-1}, which is the k value which had the most power, is shown here for the $B_{P\text{-average}}(\psi = 4) = 200$ G case.

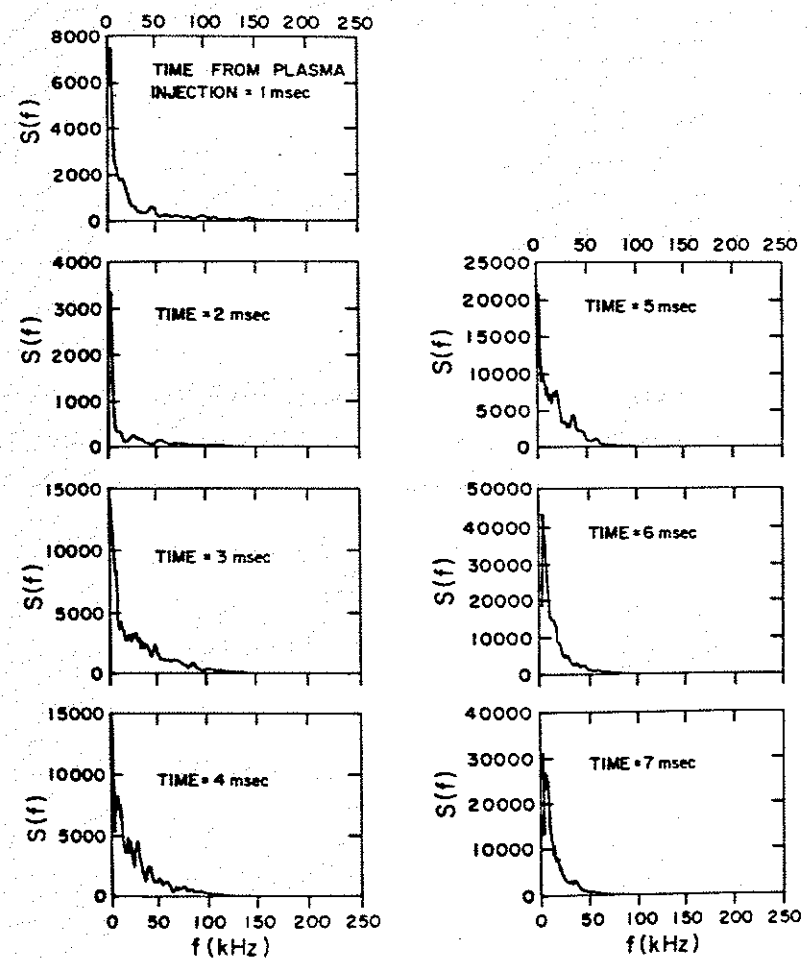

Fig. 11. The time dependent characteristic plasma frequencies calculated from the measured plasma parameters is shown in this figure, for the $B_{P\text{-average}}(\bar{\psi} = 4) = 200$ G case.

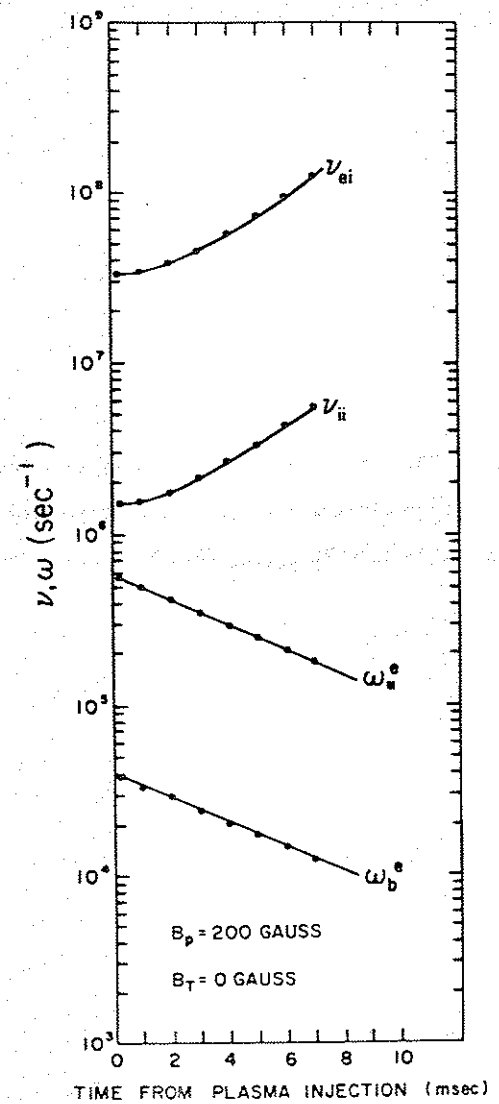

Fig. 12. The behavoir of S(k) as a function of time, calculated from integrating the frequency spectra, is shown in this figure, for the $B_{P\text{-average}}(\psi = 4) = 1$ kG case.

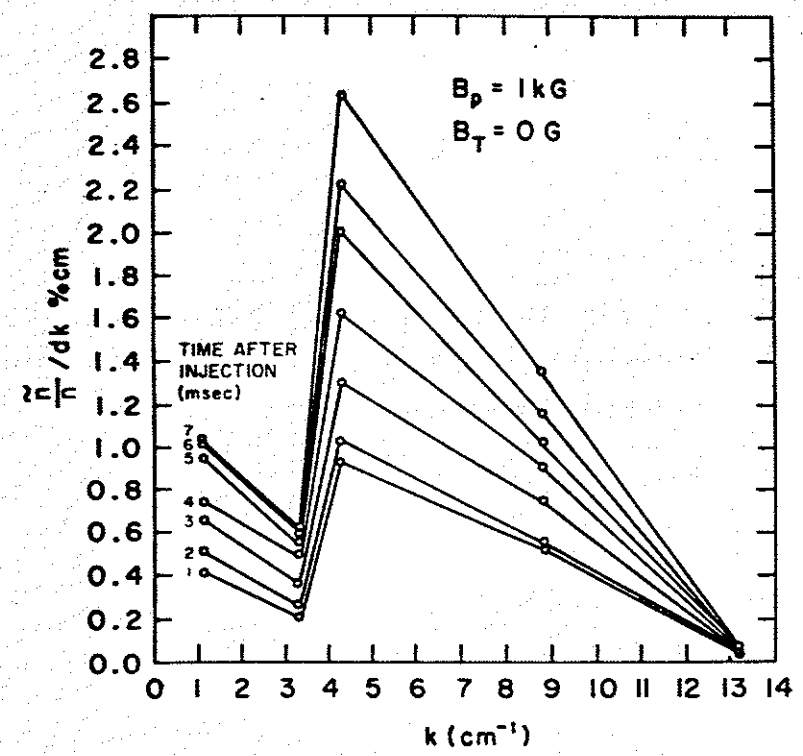

Fig. 13. The behavoir of S(k) as a function of time, calculated from integrating the frequency spectra, is shown in this figure, for the $B_{P\text{-average}}(\Psi = 4)$ = 200 G case.

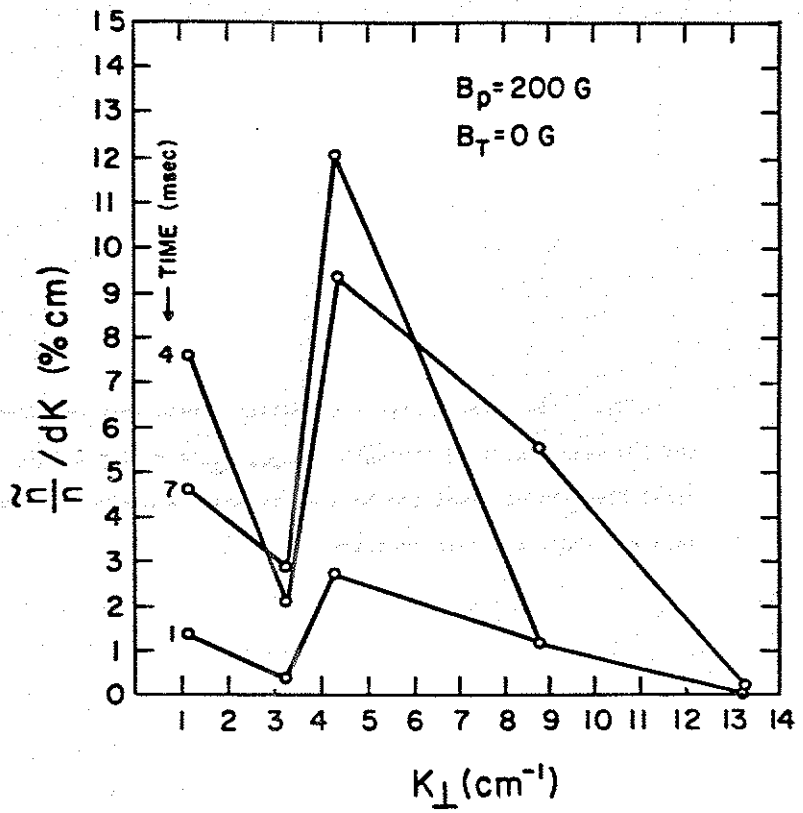

Fig. 14. The total fluctuation level, $\frac{\tilde{n}}{n}$, was calculated from integrating the spectral density function, S(f,k), over all frequency and wavenumber space. The total fluctuation level increased with time during a shot, at this magnetic field strength, $B_{p\text{-average}}(\psi = 4) \approx 1$ kG.

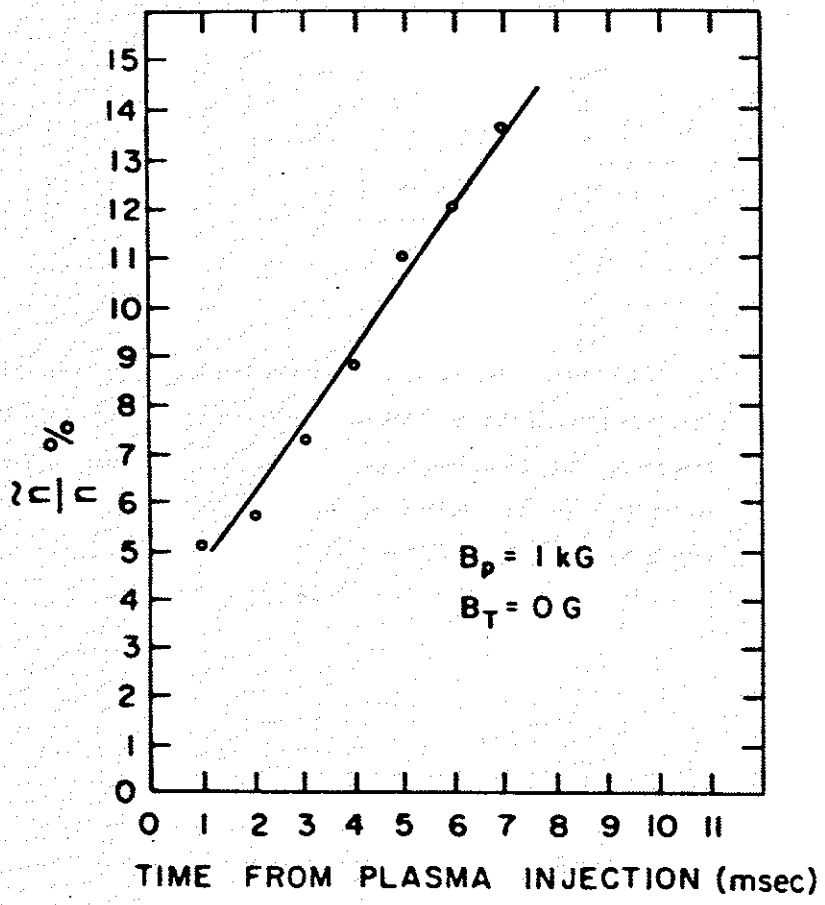

Fig. 15. Very high fluctuation levels were measured at the low magnetic field strength, $B_{P-average}(\psi = 4) = 200$ G. The total fluctuation level can be seen to reach a maximum at 4 msec into the shot, and then decrease.

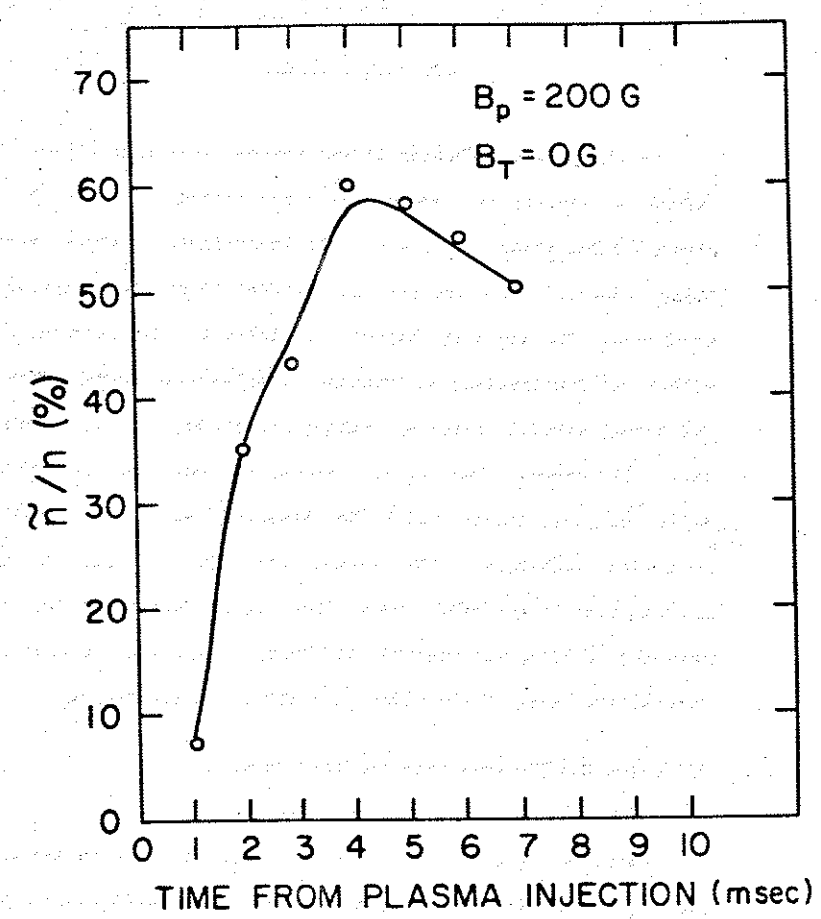

Fig. 16. The total fluctuating density, $\tilde{n}$, which has not been normalized to the plasma density, n, is shown in this figure. Note that $\tilde{n}$ does not vary greatly for the two magnetic field strength cases shown.

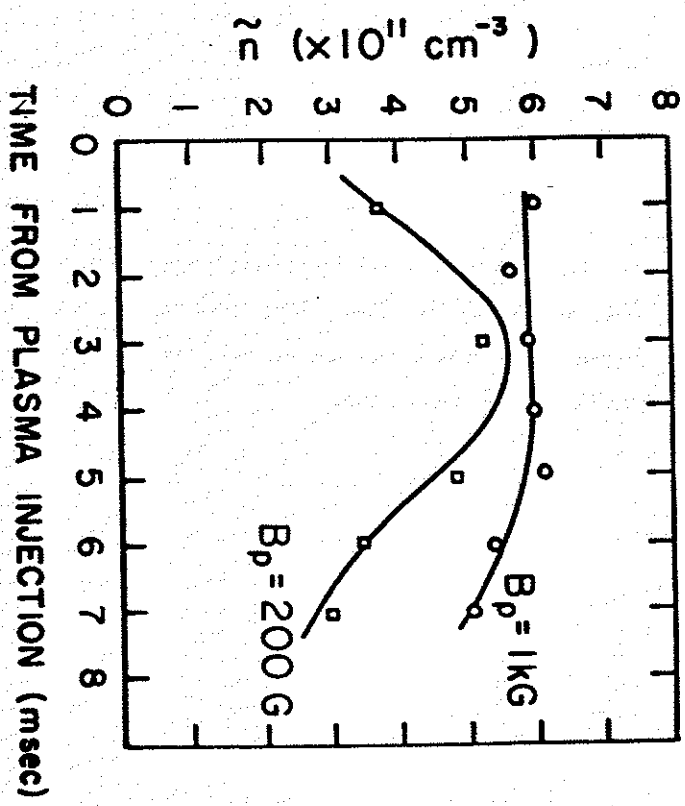

Chapter 5

Particle Transport

In the previous chapter it was demonstrated that there is indeed a significant amount of wave activity present in the plasmas under study. We now wish to investigate to what extent these observed fluctuations contribute to the total particle transport. The approach that will be taken to demonstrate the effect of fluctuations on transport involves two parts. First, the actual particle transport taking place due to all causes will be shown. The actual transport and the associated diffusion coefficients will be measured using a profile evolution technique. The second part is to calculate the contribution of the drift wave like modes contained in the measured fluctuation spectra using various theories to link the fluctuation level of the modes to a diffusion coefficient.

Diffusion Coefficients from Profile Evolution

Particle transport studies on the octupole have in the past used two techniques to measure a diffusion coefficient. The profile evolution technique entails measuring the time dependent plasma profile with Langmuir probes and microwave interferometers. Then this profile information is used to compare to the output of a numerical solution to the diffusion

equation. The diffusion coefficient scaling (with plasma density, magnetic field, and plasma temperature) and magnitude are then adjusted to make this numerically predicted profile fit the measured density profile. This technique was used to measure the spatially dependent perpendicular diffusion coefficients given in this thesis. The second technique for measuring the perpendicular diffusion coefficient entails measuring the particle flux ($\vec{\Gamma}$) to a wall surface and the plasma density gradient ($\vec{\nabla}n$) near the wall. From this information a diffusion coefficient can be calculated using $D_\perp = -\frac{\vec{\Gamma}}{\vec{\nabla}n}$. The principal reason for not using the latter technique is that the particle collectors[1] mounted on the internal rings used to measure the particle flux have been removed.

Time dependent ion saturation current profiles were measured for each of the plasmas of interest. An entire time dependent profile was constructed from many plasma discharges. Each spatial position represents one or more discharges averaged together. In order to insure that the profile was insensitive to shot to shot variations in plasma conditions not only was multiple shot averaging done, but also the data was normalized to the signal from a stationary probe located far ($\sim$ 25 cm $\gg \rho_i$) from the movable probe. When the signal from the stationary probe deviated from the accepted normalizing shot (taken before the profile scan was started) by more than 10% then that shot was automatically rejected and was not used in constructing the profile. Barring major problems; field prefires, timing problems, and vacuum accidents, the shot to shot reproducibility was strongly governed by performance of the plasma source, the coaxial Marshall gun. The "intermediate density" gun is a very well behaved plasma source, and it reproduces the peak injected density to within 5% on almost all discharges.

The profiles shown were taken in the bridge region of the octupole (i.e., the region between the surface of the lower outer ring and the vacuum vessel wall along a major radius). In this way all flux surfaces between $\psi = 2.5$ (the ring surface) and $\psi = 7.25$ (near the last MHD stable surface, the critical surface) were sampled by physically moving the probe tip location.

Profiles were taken for various experimental conditions; with and without toroidal magnetic field, at high and low poloidal field magnetic strengths. Before displaying any profiles more should be said about the actual plasma parameters. Plasma parameters were displayed for each discharge by the on-line data aquisition computer. Shown in Fig. 1 are the diagnostics normally monitored. Plasma is injected at 23.4 msecs following the firing of the magnetic fields (which are

crowbarred at 23 msec). The plasma density on the separatrix ($\psi = 5.5$) is seen to be 1.2×10^{13} cm^{-3} at 200 μsec following injection. The other three diagnosics, barrier total radiated power bolometer (TRP), hydrogen beta light, and oxygen III light are not absolutely calibrated but do give indications of shot to shot changes in plasma impurity content and fuel reflux. These diagnostics are sensitive to both the density of neutrals and electron temperature so interpreting their exact meaning is difficult.

The first ion saturation profile shown was for an average poloidal field strength of 1 kG and no toroidal field (i.e., no shear). This ion saturation profile is shown in Fig. 2. Ion saturation current in amps is along the vertical axis and probe position in octupole coordinates in units of Dories[2] is displayed on the horizontal axis. The first profile was taken at 0.25 msec following gun injection before the plasma has reached "equilibrium" (i.e., the plasma had stabilized and the large potentials fluctuations present immediately after gun injection have disappeared). In succeeding 0.25 msec spaced overlays the profile was seen to decrease since both the density and temperature were decreasing. Note that for approximately the first msec the profile shape was concave upward on either side of the separatrix ($\psi = 5.5$). After a msec the profile shape had changed to no longer be concave upward.

In order to unfold the density profile from the ion saturation current ($I_s \propto n (T_e)^{0.5}$) profile, the electron temperature profile had to be measured. The electron and ion temperatures were measured using admittance probes and gridded energy analyzers, respectively. To within the accuracy of the measurements the ion and electron temperatures were equal. This is reasonable since the ion-electron equlibration time was shorter than the particle confinement time for all cases studied. The temperature decay time was approximately 3 msec after 0.5 msec. For these particle confinement experiments the spatial temperature profile was flat to within the accuracy of the measurements and was therefore assumed constant in space. During the profile scan, the normalization probe was monitored (see Fig. 3, left graph). Note how well the normalization signal for this discharge matches the normalization shot overlay. On the right side of Fig. 3, the ion saturation current as a function of time for one position is displayed.

As the magnitude of the poloidal field was reduced the shape of the ion saturation current profile was changed. At an average poloidal field strength of 200 G the profile had a shape immediately following plasma injection which had no sections which were concave upward (Fig. 4).

When toroidal field was added to the poloidal field, only small changes in the profile shape were noted. At high poloidal magnetic fields ($B_{P-average}$ = 1 kG) , the ion saturation current profile was only 10% wider at half maximum (Fig. 5). It still exhibited the concave upward shape off the separatrix that was found in the B_T = 0 G, $B_{P-average}$ = 1 kG. No change in the time evolution of the profile, and consequently the overall particle confinement time was detected when B_T was added. At low poloidal fields, $B_{P-average}$ = 200 G, no changes in profile shape or time decay were noted. That is, at low poloidal field values the profile shapes were broad and no broadening was seen when toroidal field was added.

The profile shape was governed by the spatially varying particle diffusion coefficient when no external sources or sinks (see chapter 6) for particles are present. The source and sink term in the particle diffusion equation was, therefore, set to zero in the calculations. By solving the transport equation (Eq. 22, chap 3) in octupole coordinates and matching this solution to the measured ion saturation current profile which has been previously measured, the time and space dependent diffusion coefficient can be calculated. As described in chapter 3, the diffusion coefficient was constructed from two terms. Adding more terms in the equation for the diffusion coefficient would obviously make the predicted profiles more

closely match the observed profiles. However, the addition of more terms would not necessarily lead to enlightenment as to the mechanisms involved in the diffusion.

There are experimental, theoretical, and historical reasons for selecting the scaling laws used in the transport calculations. Previous work[3,4] showed that profile shape at any moment was governed by the magnitude of the diffusion coefficient at each spatial point. That work demonstrated theoretically that density profile shapes which were concave downward everywhere in space were indicative of a diffusion coefficient which scaled like classical, $D_\perp \propto \frac{n}{B^2}$. It was also shown that for a diffusion coefficient with a different scaling; i.e.; $D_\perp \propto \frac{1}{\sqrt{n}}$, that density profiles exhibited shapes that had regions which were concave upward. At that time experimental density profiles showing both shapes and associated diffusion coefficient scalings were seen in the octupole for the low plasma density regimes, $n < 5 \times 10^{11}$ cm^{-3}.

The particle confinement time, $\tau_p \propto \frac{1}{D_\perp}$, at various plasma densities is shown in Fig. 6. This data was taken on plasmas made from several plasma sources over a period of many years. For all data shown in Fig. 6, except the "intermediate density" gun data, the particle confinement time is also the normal mode decay time. For the "intermediate density" gun data, the

profile shape was not decaying as a normal mode when the particle confinement time shown, was calculated. The ion and electron temperatures varied, but in all cases was never above 15 eV. The poloidal magnetic field strength was 1 kG for all data shown. The diffusion coefficient scaling which indicates the profile shape is also noted. The two data points at $n \sim 10^{12} cm^{-3}$ and $n \sim 10^{13} cm^{-3}$ were taken from data found during the course of this research. The remaining data was constructed from references 2 and 3.

Upon inspection of the density (ion saturation current) profiles that were taken while using the intermediate density gun to make higher density plasmas ($n > 10^{12}$ cm^{-3}) both types of scaling of the diffusion coefficient as indicated by the profile shape were seen to exist. It was possible to continuously go from one shape ($D_\perp \propto \frac{1}{\sqrt{n}}$) to the other shape ($D_\perp \propto \frac{n}{B^2}$) by lowering the poloidal magnetic field. This behavior, therefore, indicated that the diffusion coefficient used in the numerical solution to the transport equation should contain the essence of both types of scaling. Thus, the reasoning behind the choice for diffusion coefficient $D_\perp = \frac{C_1 n}{B^2\sqrt{T_e}} + \frac{C_2\sqrt{T_e}}{\sqrt{n}}$ used in the transport code, NEVOL (see chapter 3), can be seen.

The values assigned to the constant coefficients determine the relative importance of each term in $D_\perp$. The values of C_1 and C_2 were adjusted to make the profiles predicted by NEVOL for a high poloidal magnetic field strength (B_p = 1 kG) agree with the experimental profile to within 20%. C_1 and C_2 are constants which are independent of time. This was true for each spatial grid point for the 10 msec following plasma injection over which time comparisons were made. This field strength was chosen because during the course of time in a discharge the profile changed from one shape ($D_\perp \propto \frac{\sqrt{T_e}}{\sqrt{n}}$) to the other shape ($D_\perp \propto \frac{n}{B^2\sqrt{T_e}}$). Once C_1 and C_2 were found, they were held fixed for further runs using NEVOL for other poloidal field strengths. Only the measured starter profile, and the measured time dependent electron temperature needed to be changed from run to run at different poloidal field strengths in order to accurately watch the numerically predicted profiles to the experimental time dependent profiles.

The profile evolved for the $B_{p\text{-average}}$ = 1 kG case contains characteristics of both types of scaling. The graphic output of NEVOL for that case will now be shown. Similar calculations for the other values of B_p for which profiles have been taken will be summarized in the last section of this chapter. The ion saturation current profile that was predicted by NEVOL for the B_p = 1kG case is shown in Fig. 7. The corresponding density

profile shown in Fig. 8 does not contain the $\sqrt{T_e}$ multiplicative factor present in the ion saturation current profile. The spatially dependent magnitude of the two components of the diffusion coefficient is shown in Fig. 9 for the time 7 msecs after plasma injection. Each component is displayed separately to emphasize how each varies across the profile. The numerical "best fit" to the experimentally measured profile indicated that the value of C_1 was such that that portion of the diffusion coefficient had a magnitude equal to 10 times classical. There is no theoretical justification for a diffusion coefficient which scales like classical but at an enhanced magnitude. The magnitude of the portion of the diffusion coefficient which scaled like $D_\perp \propto \frac{\sqrt{T_e}}{\sqrt{n}}$ was that predicted by Okuda and Dawson[5] for a thermal vortex cell spectrum but with an effective temperature, T*, equal to 10^5 eV. (See chapter 2, vortex diffusion section.)

To illustrate how well the numerically calculated profile predicted by NEVOL matches the actual profile magnitude on the sepratrix as a function of time, the predicted density was compared to the density measured with the 70 GHz microwave inteferometer (Fig. 10).

For completeness, the initial conditions (the starter ion saturation current profile) were evolved in time under the influence of each term of the diffusion coefficient used in the program, NEVOL. This will demonstrate the effect each term has on the profile when taken individually. It will also show the "normal" mode shapes that the density profile assumes under the influence of each choice for the diffusion coefficient scaling. Shown in Fig. 11 is the density profile that would be evolved from the starter profile if the diffusion coefficient was $D_\perp \propto \frac{n}{B^2\sqrt{T_e}}$. Figure 12 shows the density profile generated if the diffusion coefficient scaled like $D_\perp \propto \frac{\sqrt{T_e}}{\sqrt{n}}$.

The actual diffusion taking place in the Levitated Octupole has, therefore, been measured for each plasma and magnetic field configuration of interest.

Diffusion Calculated from Density Fluctuations

The contribution of the fluctuation induced particle transport due to drift wave modes to the total particle transport was then calculated from the fluctuation spectra measured with the microwave scattering diagnostic. Once the turbulence has been identified as drift wave like in nature, various theories can be applied relating the fluctuating quantity, $\tilde{n}(f,k)$, to a diffusion coefficient.

Two different approaches were used to calculate the perpendicular particle transport coefficients. The first approach entails invoking strong turbulence theory to calculate a diffusion coefficient. Recall from chapter 3 that the turbulent diffusion coefficient can be calculated from:

$$D_\perp = \langle \bar{v}_k^2 \rangle \langle e^{-t/\tau_k} \rangle = C \langle \bar{n}_k^2 \rangle \langle e^{-t/\tau_k} \rangle \qquad (1)$$

The density fluctuations that were measured with the microwave scattering system have a broad frequency spectra indicating that strong turbulence theory can be used to evaluate the unknown τ_k, the decorrelation time. This implied that waves contained in one portion of the spectrum could interact with waves in the other portions of the spectrum thereby causing their decorrelation. The decorrelation time for the spectra can then be estimated:

$$\tau_k = \frac{1}{k^2 D_{T.P.}} \qquad (2)$$

where $D_{T.P.}$ = test particle diffusion coefficient.

The correlation function was taken to find the correlation time, τ_c, for the actual data. The decorrelation time τ_k was then compared with the correlation time calculated directly from the time dependent data in order to evaluate whether the use of

strong turbulence theory was justified. If $D_{T.P.}$ was set equal to $D_\perp$, the actual diffusion due to these modes, then τ_k was approximately equal to $\frac{1}{k^2 D_\perp}$. For example, refer to Fig. 6 of chapter 4 which graphically displays the autocorrelation function for 1 msec of the density fluctuation data for $k_\perp = 4.23\ cm^{-1}$. The half width half maximum point indicates that the correlation time, τ_c, was 0.01 msecs. To look ahead a little, the strong turbulence diffusion coefficient (to be given in the next section) has a value $0.4 \times 10^3\ cm^2/sec$. Calculating the decorrelation time from $\tau_k = \frac{1}{k^2 D_{\perp ST}}$ yields a value of 0.011 msecs. Since the correlation times are similar, a diffusion coefficient of the form:

$$D_{\perp ST} = \frac{r_n}{\sqrt{2}} \left\{ \int \frac{\omega_k^2}{k^2} \left(\frac{\bar{n}_k}{n}\right)^2 d\vec{k} \right\}^{0.5} \qquad (3)$$

can be used to estimate the true particle diffusion. For our typical density profiles the density gradient scale length, r_n, is approximately 9 cm.

The second theory applied to the density fluctuation data was a linear drift wave diffusion theory. The fluctuation level, $\frac{\bar{n}}{n}$, summarized in chapter 4, was seen to usually increase as a function of time during a shot. This indicated that the drift wave like fluctuations were still growing and had not

saturated. One could also say that because the frequency spectra were broad that a linear diffusion theory may not have been valid since linear drift wave theory in general predicts only single modes to be present. This was not indicated in the data. Other research groups [6] have used a linear theory to calculate the diffusion even when its validity was questionable. It was for these reasons that linear diffusion theory was also used to calculate $D_\perp$, and this will be refered to as $D_{\perp LDW}$:

$$D_{\perp LDW} = 2\, r_n^2 \int \omega_k \sin(\phi_k) \langle (\tilde{\frac{n}{n}})^2 \rangle \, d\vec{k} \qquad (4)$$

Since it is desired to calculate the maximum amount of diffusion attributable to the drift wave modes the phase factor, $\sin(\phi_k)$, was assigned a value 1, thus giving the maximum amount of transport.

Summary of Diffusion Calculations

It is now possible to compare the actual diffusion present as measured by the profile evolution technique to the diffusion induced by fluctuations in plasma density. The profile evolution technique enabled us to measure the spatial magnitudes of the total diffusion coefficient for all times. The fluctuation measurements were made by aiming the microwave transmitter-receiver pairs such that the scattering volumes were

centered at $\psi \approx 4$ and $\psi = 7$. The most comprehensive scan of wavenumber space was available for $\psi = 4$. Therefore, the diffusion calculations shown in this section were for fluctuations localized at $\psi = 4$. This was also where the density gradient was maximum. The $\psi = 4$ value for the ψ-space resolved diffusion coefficient claculated with NEVOL was compared to the transport coefficients calculated from the fluctuation spectrum. Identical calculations made at $\psi = 7$ in the average-minimum-B region of the octupole indicated that the actual and fluctuation induced transport were very similar to that calculated for $\psi = 4$. That data is not displayed since only 3 wavenumber values can be measured at $\psi = 7$ and only 2 of those were for perpendicular wavenumbers above $k_\perp = 3$ cm^{-1} which was considered as the dividing line between drift wave turbulence and convective cell turbulence. Five k space values contributed to the calculations at $\psi = 4$.

The time resolved diffusion coefficients for three magnetic field configurations; $B_P = 1$ kG, $B_T = 0$ G; $B_P = 200$ G, $B_T = 0$ G; and $B_P = 1$ kG, $B_T = 300$ G will be shown in Figs. 13, 14, and 15, respectively. It was difficult to assign error bars to these values since there were many steps involved in the calculation of the diffusion coefficient from the fluctuation data. The scattering system was calibrated to within 10%. Only estimates can be made about the accuracy of the k-space

integration and the diffusion theories themselves. It certainly appears as though the calculations should be accurate to within a factor of two.

In the high field case (B_p = 1kG, B_T = 0 G) it was seen that the magnitude of the fluctuation induced transport calculated with both strong turbulence and linear drift wave theories made up at most 30% of the actual transport (Fig. 13). The strong turbulence diffusion coefficient, $D_{\perp ST}$, was seen to have a value of 0.4×10^3 cm^2/sec ($\psi = 4$) at 1 msec into the shot and increased in magnitude by a factor of 2 by 7 msecs. Linear drift wave theory calculated a value for the perpendicular diffusion coefficient, $D_{\perp LDW}$, consistently less than that calculated by strong turbulence theory. The actual diffusion coefficient maximized at a value of 2.8×10^3 cm^2/sec at 6 msecs into the shot. This behavior was quite reasonable considering that there were two diffusion mechanisms, one scaling like $D_\perp \propto n$ and one like $D_\perp \propto n^{-1/2}$, that together made up the total diffusion. The profile initially had a $D_\perp \propto n^{-1/2}$ shape. The diffusion which was porportional to $n^{-1/2}$ was maximum near the plasma edge at ψ =2.5 and at $\psi = 7.5$. Similarly, the part of the diffusion coefficient which scaled like n was maximum near the separatrix ($\psi = 5.5$) where the density was greatest. In time, as the two diffusion mechanisms competed, the profile shape changed and thus the value of $D_\perp$ at

$\psi = 4$ changes. By 6 msecs the profile shape had assumed a classical shape indicating that the diffusion taking place after that time scaled like $D_\perp \propto n$. The density, n, was decreasing with time and therefore one would expect that the diffusion which scaled like n should decrease. The value of the classical diffusion coefficient (not the diffusion coefficient which was enhanced above classical) was approximately 200 cm^2/sec and remains almost constant with time because the density and electron temperatures are decreasing in such a way as to keep it constant.

When 300 G of toroidal field was added to a poloidal field of 1 kG, no change in the value of the diffusion coefficient calculated from profile evolution was seen(Fig. 14). Recall, the profile shape was seen to not change dramatically but only increase in width by 10%. The particle confinement time on this separatrix (measured with the 70 GHz interferometer) also did not change with the addition of toroidal field. Thus, since the profile evolution program was accurate to only 20%, no change in the diffusion coefficient was detectable, as expected.

It is not understood why shear stabilization of the convective cell modes which contribute heavily to the observed diffusion has been defeated in this instance. In this case; B_p = 1 kG, B_T = 300 G, the average shear length, L_s, at $\psi = 4$

was approximately 100 cm. This amount of shear should be sufficient to damp out the convective cell activity[7]. The damping time, τ_d, was calculated in the short mean free path (compared to shear length) limit:

$$\tau_d = (k_{\parallel} D_{\parallel})^{-1} = \frac{L_s^2 \nu_{ei}}{v_e^2} \qquad (5)$$

For $L_s = 100$ cm, $v_e = 1 \times 10^8$ cm/sec ($T_e = 6$ eV), and $\nu_{ei} = 1 \times 10^7$ sec^{-1} the damping time should have been approximately 0.01 msec. The diffusion is indicative of convective cell activity which persisted throughout the experiment (10 msec), even though the cell should have been strongly damped.

The basic behavior of $D_{\perp ST}$ and $D_{\perp LDW}$ was the same as the case without toroidal field; i.e., without shear. Comparing the magnitude of the diffusion coefficients with their corresponding value with no toroidal field, it can be seen that they are slightly larger when toroidal field was added. As toroidal field was added, the field lines tilted such that $k_{\parallel}$ was no longer $k_{\perp}$. When the slight k-space anisotropy, which has been preserved with the addition of toroidal field, was taken into account, the magnitude of the diffusion coefficients ($D_{\perp ST}$, and

$D_{\perp LDW}$) were reduced to their previous values when no toroidal field was present. This then demonstrated that the addition of shear has had no effect on the diffusion attributable to the drift wave portion of the fluctuation spectrum.

A different time dependent behavior of the actual diffusion coefficient was seen at lower poloidal magnetic field values, specifically at $B_p = 200$ G, with and without toroidal field. At this magnetic field value the initial profile shape indicates that the diffusion mechanism which goes like $D_{\perp} \propto n$ was dominant. Since $D_{\perp}$ was falling just like n in time, this was an additional confirmation of the scaling. This was precisely the behavior that was expected since the two mechanisms represented by the two parts of the diffusion coefficient differ in the magnetic field scaling by a factor of B^2. It should also be noted that the magnitude of $D_{\perp}$ was greater by a factor of 5 when compared to the high field case.

The calculations of the fluctuation induced transport shows that it made up at most 50% of the total diffusion.(Fig. 14) Linear drift wave theory (with $\sin(\phi_k) = 1$) predicts a larger value for the diffusion coefficient than does strong turbulence theory at these low poloidal field magnitudes. This can be understood when one recalls the scaling for the two calculations: $D_{\perp ST} \propto \frac{\omega}{k} \frac{\tilde{n}}{n}$, $D_{\perp LDW} \propto \omega \left(\frac{\tilde{n}}{n}\right)^2$; and notices that the

fluctuation level $\frac{\tilde{n}}{n}$, was much higher (to 60%) at this lower field than at higher magnetic field strengths.

When toroidal field was added to this low poloidal field, no effect was seen in the profile shape or the separatrix confinement time. Similarly, as described in chapter 4, there was no change in S(f,k) and therefore no change in $D_{\perp ST}$ or $D_{\perp LDR}$.

The total effect on confinement by varying the poloidal field strength is shown in Figs. 16 and 17. Figure 15 indicates the profile averaged particle confinement time. The plasma beta is also displayed. A finite beta existed in these plasmas, but no direct correlation, other than what is illustrated in Fig. 16, with the particle transport was observed. The time at which all data in Fig. 17 was taken was 3.5 msecs after plasma injection. It should be noted that as the magnetic field strength was varied, the resulting trapped plasma densities and temperatures varied. The calculations used to generate Figs. 16 and 17 reflect this, and do not represent the behavior of the transport with respect to $B_{P\text{-average}}$ only, because other parameters (n, T_e) were not held constant as $B_{P\text{-average}}$ was varied. The actual diffusion coefficient at (ψ = 4) varies as $B_{P\text{-average}}^{-1}$. Note that as $B_{P\text{-average}}$ was lowered the drift wave contribution to the total (actual) diffusion increases.

This would indicate that at lower fields the vortex diffusion contribution ($D \propto n^{-1/2}$) was being reduced. This was consistant with the change in the profile shape seen at injection from concave upward near the plasma edge to a profile where $D \propto n$. This behavior was expected since the viscous damping time for or 5 cm wavelength fluctuations (typical convective cell size) increased as $B_{P\text{-average}}$ was decreased. As shown in Fig. 18, both the viscous damping time and the turbulent damping time are greater at B_p = 1 kG than at B_p = 200 G. The magnitude of the viscous damping time indicated that the vortex cells and their resulting contribution to the diffusion should have damped out quickly in time if they were generated only by the initial conditions (i.e. the turbulent injection process). However, the vortex diffusion was present in the experiment for times much longer than the damping time indicating that they were driven. It was possible that energy was being supplied to the vortex cells by higher frequency, shorter wavelength turbulence. The mechanism for inverse cascading energy in k-space between drift wave turbulence and convective cell modes has been studied theoretically.[8] No experimental proof exists for this effect other than the anomolously long time over which vortex cell diffusion scaling was seen. Through this mechanism, the drift wave turbulence may have been contributing more to the diffusion indirectly than it did directly as calculated with strong turbulence or linear drift wave theories.

References for Chapter 5

[1]A. J. Cavallo, Ph.D. Thesis, University of Wisconsin, 1975.

[2]R. Dory, Ph.D. Thesis, University of Wisconsin, 1962.

[3]G. A. Navratil, Ph.D. Thesis, University of Wisconsin, 1976.

[4]J. R. Drake, J. R. Greenwood, G. A. Navratil, and R. S. Post, Phys. of Fluids 20, 148(1977).

[5]H. Okuda and J. M. Dawson, Phys. Fluids 16, 408(1973).

[6]W. Horton, R. D. Estes, Nuclear Fusion, 19, 203(1979). see also E. Mazzucato, Phys. Rev. Letters 36, 792(1976).

[7]H. Okuda and J. M. Dawson, Phys. of Fluids 16, 1456(1973).

[8]C. Z. Cheng and H. Okuda, Formation of Convective Cells, Anamalous Diffusion and Strong Turbulence due to Drift Instabilities, PPPL-1316, 1971.

Fig. 1. The plasma parameters normally monitored by the on-line data aquisition system are shown in this figure. The plasma density was measured with the 70 GHz microwave inteferometer. The other diagnostics, the total radiated power (TRP), the hydrogen beta light, and the oxygen III light are not absolutely calibrated. These diagnostics are monitored from shot to shot and are used as an indicator of the overall plasma reproducibility.

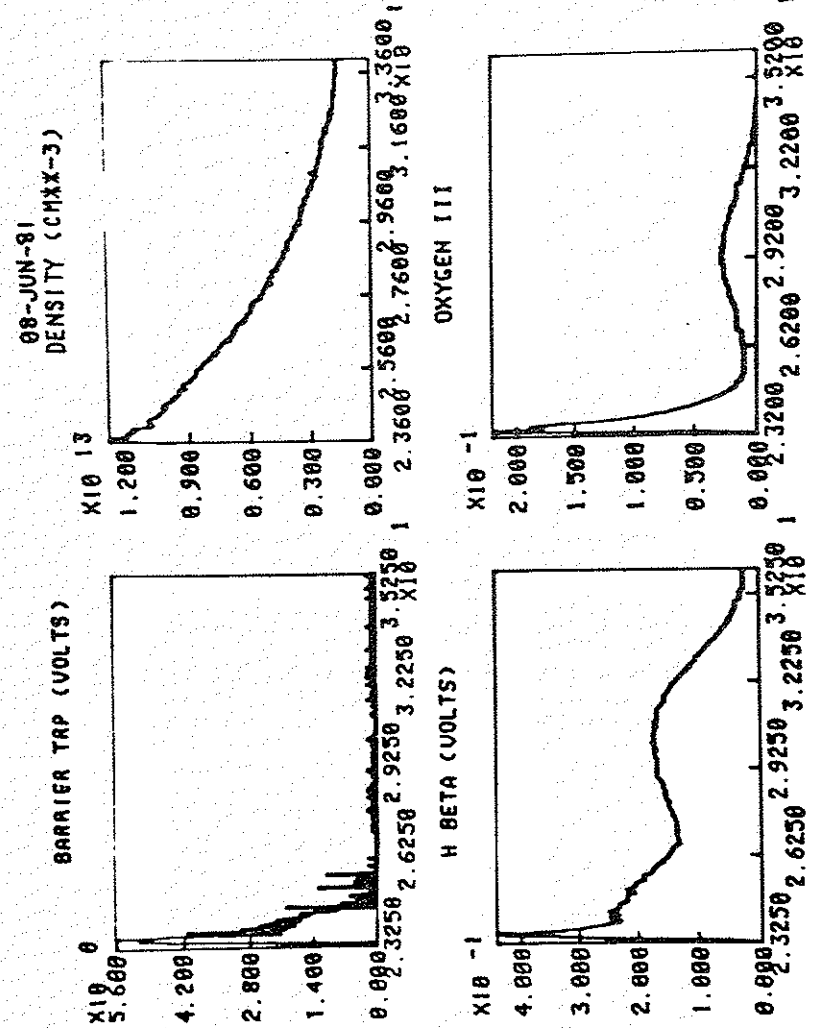

Fig. 2. The ion saturation current profiles as a function of time are shown in this figure, for $B_{P\text{-average}}(\Psi \approx 4) \approx 1$ kG. The first profile (the one with the largest magnitude) was taken at 0.25 msec after plasma injection. Each of the following profiles were taken at 0.25 msec intervals.

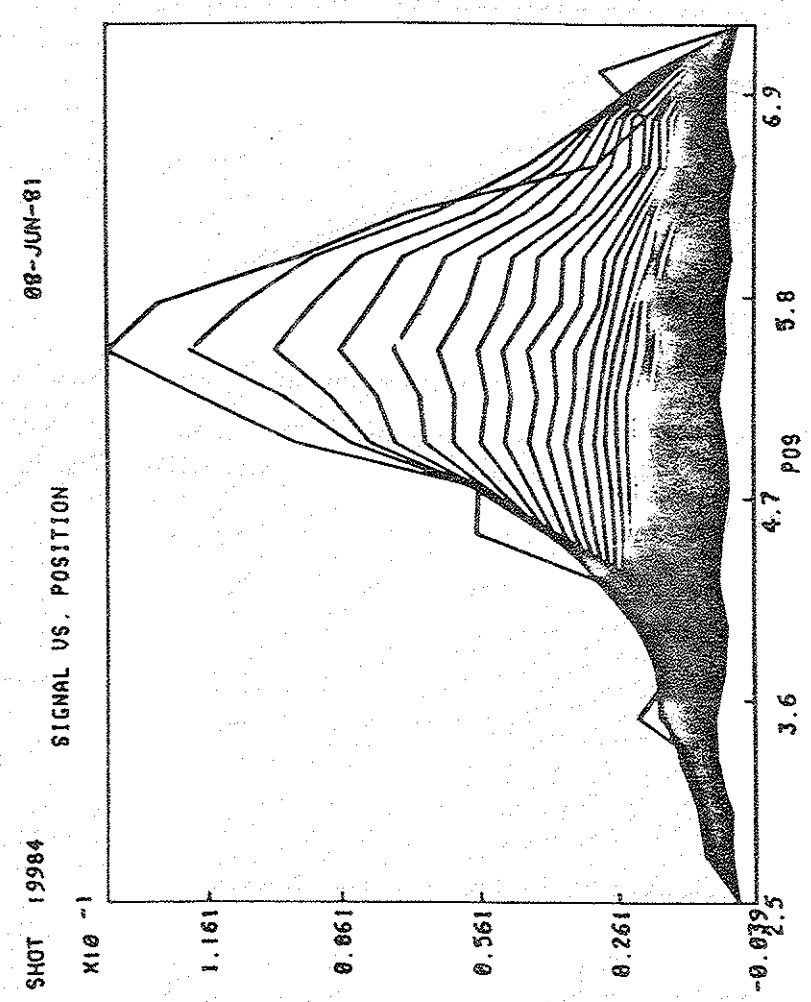

Fig. 3. The left graph is an overlay of the ion saturation current from the normalization (stationary) probe for a shot, and the normalization trace taken before the profile construction was started. The degree to which these traces overlay is an indicator of how well the plasma was being reproduced from shot to shot. The right graph is the ion saturation current taken with the moveable probe which was actually used in the construction of a profile.

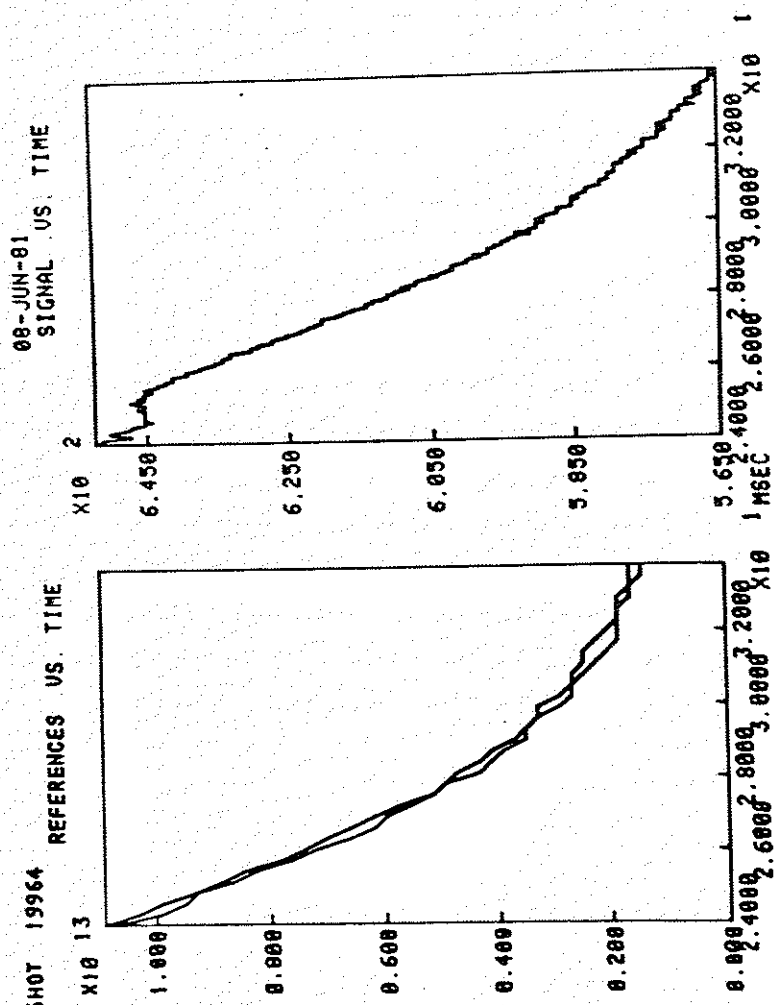

Fig. 4. This is the measured profile for the low poloidal field strength, $B_{P\text{-average}}(\psi = 4) = 200$ G. This profile was taken in the same way that the profile in Fig. 2 was taken.

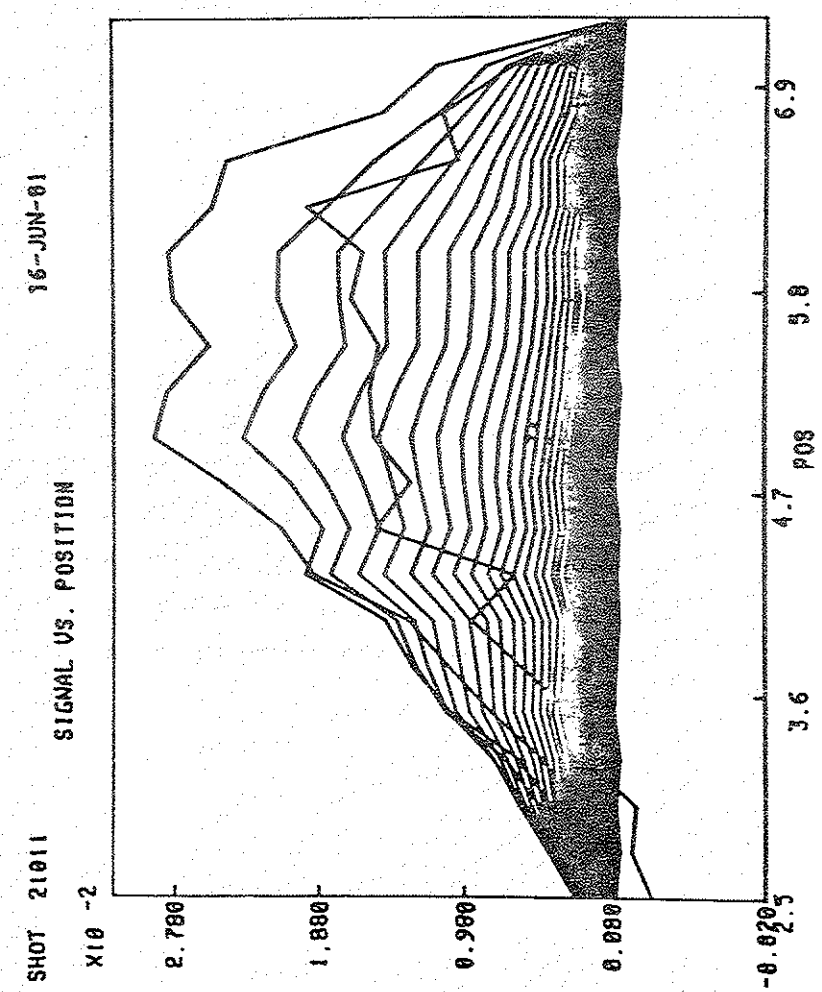

Fig. 5. This profile, with $B_{P\text{-average}}(\psi = 4) = 1$ kG and B_T(at the midcylinder) = 300 G, retains the basic shape and time behavoir that was seen in the no toroidal field case (Fig. 2).

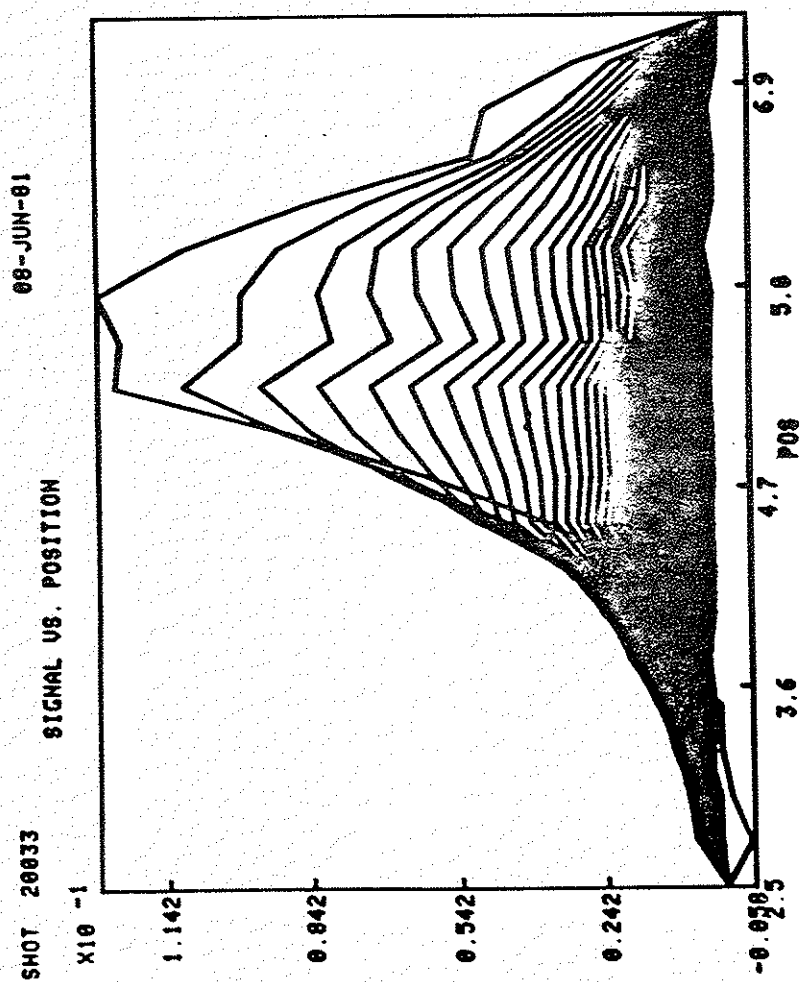

Fig. 6. The particle confinement times for plasmas made with various plasma sources is shown here to illustrate its dependence on plasma density. This data was for an average poloidal field of 1 kG and no toroidal field. All data, except for the "intermediate density" gun data, was for the plasma decaying in a normal mode. The "intermediate density" gun particle confinement times are the profile averaged confinement times.

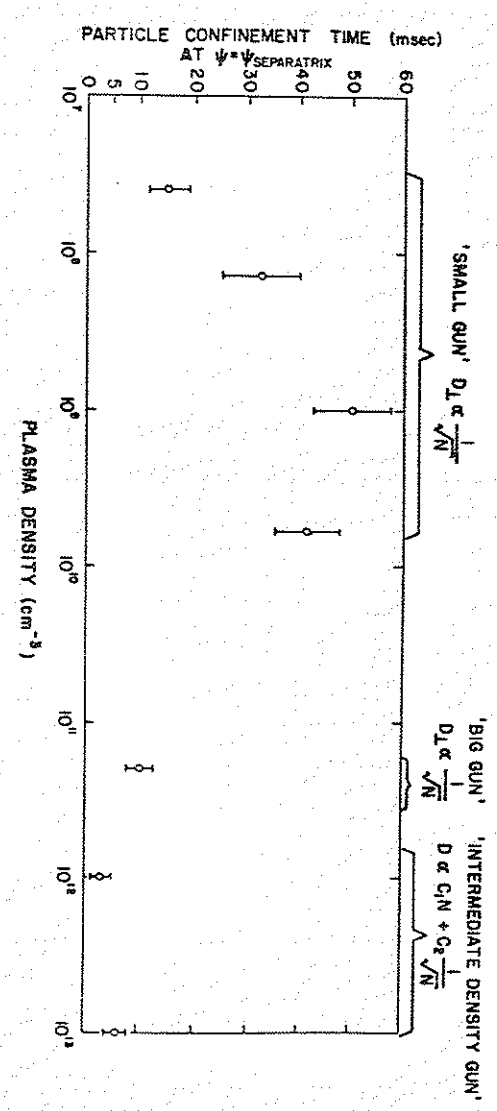

Fig. 7. This is the ion saturation current profile predicted by the diffusion equation profile evolution program, NEVOL. This profile is a simulation which should be compared to the data in Fig. 2.

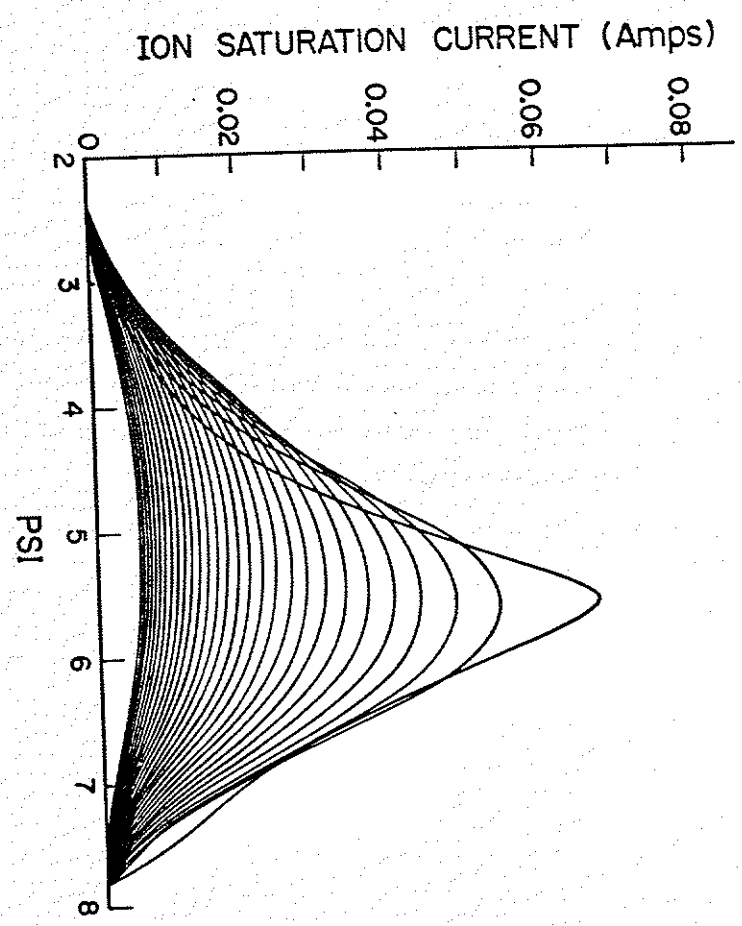

Fig. 8. The corresponding density profile predicted by NEVOL, again for the high magnetic field case, is shown here.

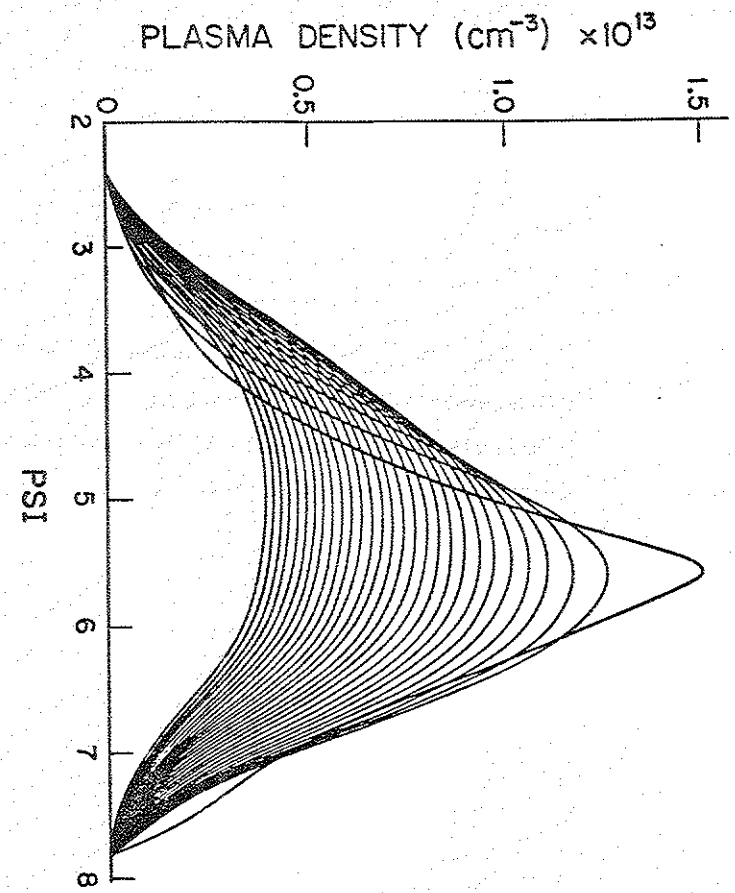

Fig. 9. The spacially dependent components of the diffusion coefficient used in NEVOL, are shown here for the case in Fig. 2, 7, and 8, at 7 msec into the shot. The dependence of the scaling of each of the diffusion coefficient components on density can easily be seen in this figure.

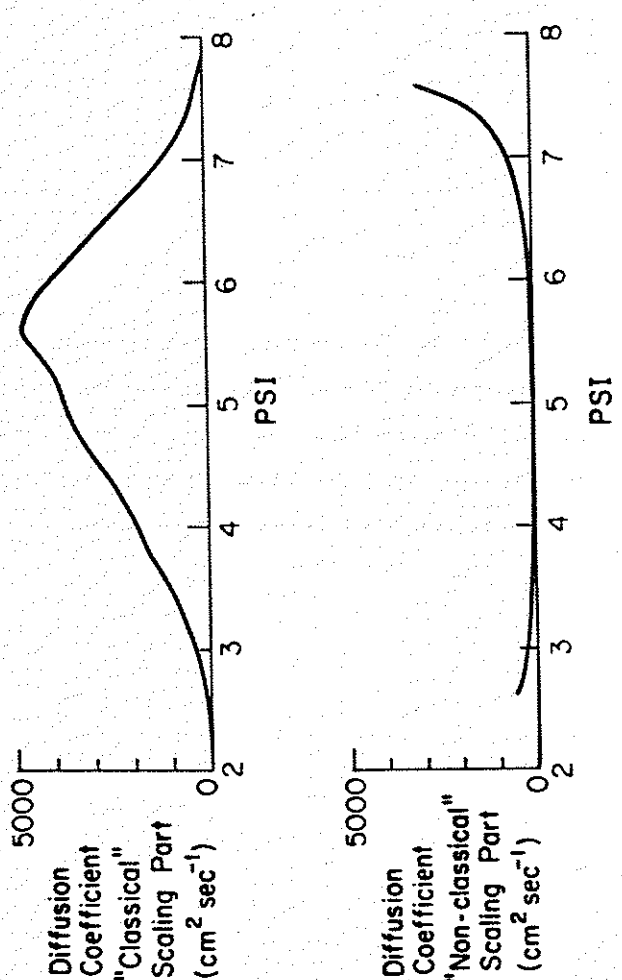

Fig. 10. The density measured with the 70 GHz inteferometer, and the output of the code, NEVOL, are compared in this figure. The dots are the sepratrix density predictions by NEVOL for the high field data.

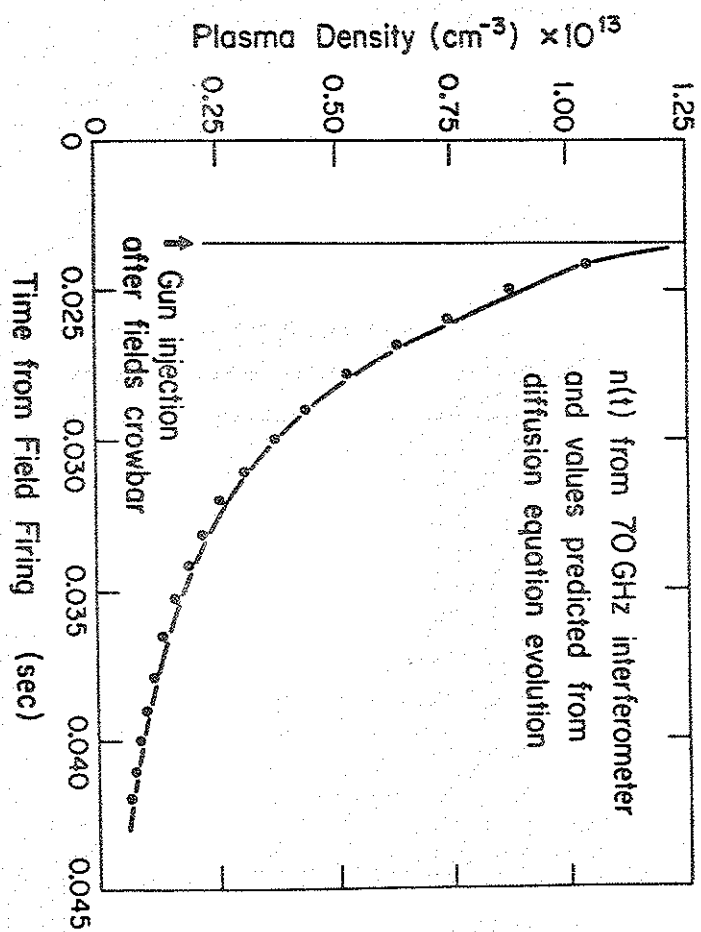

Fig. 11. Shown here is the density profile that would have been evolved from the initial starter profile if the diffusion coefficient only had one term. That term was equal to 10 times classical.

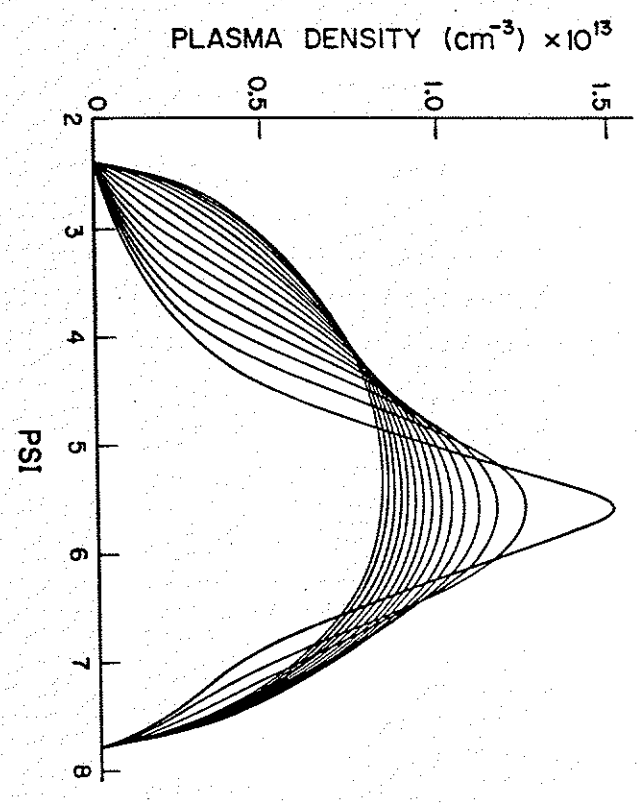

Fig. 12. This is the set of profiles that would have evolved from the initial starter profile if the diffusion coefficient only had one term which had vortex scaling.

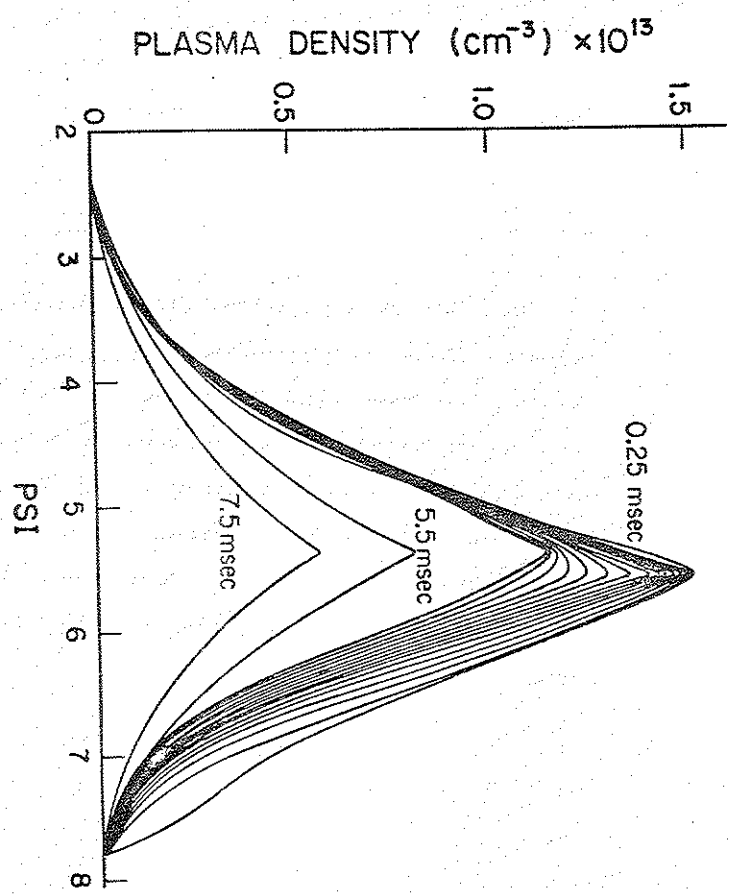

Fig. 13. The time resolved diffusion coefficients for the magnetic field configuration: $B_{p\text{-average}}(\psi = 4) = 1$ kG, $B_T = 0$ G is shown here. The diffusion coefficient calculated from the profile evolution was the actual diffusion coefficient governing the plasma transport at $\psi = 4$. The other diffusion coefficients are shown to indicate to what extent the drift wave portion of the fluctuation spectrum contributes directly to the diffusion. The classical diffusion coefficient is shown for a reference.

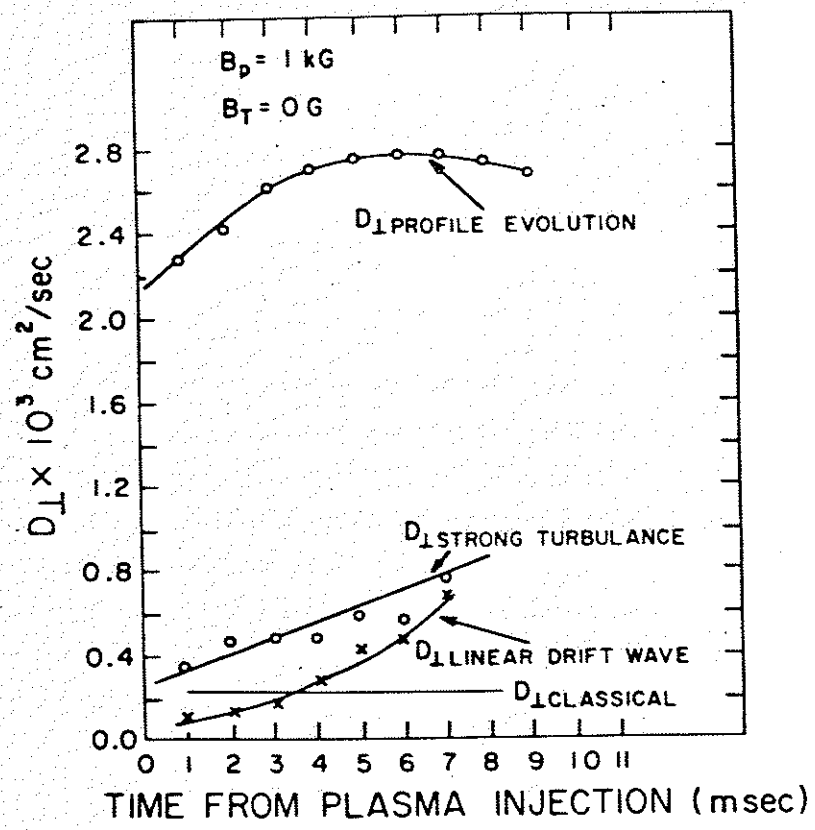

Fig. 14. The time resolved diffusion coefficients for the magnetic field configuration: $B_{p\text{-average}}(\psi = 4) = 200$ G, $B_T = 0$ G is shown here. The diffusion coefficient calculated from the profile evolution was the actual diffusion coefficient governing the plasma transport at $\psi = 4$. The other diffusion coefficients are shown to indicate to what extent the drift wave portion of the fluctuation spectrum contributes directly to the diffusion. The classical diffusion coefficient is shown for a reference.

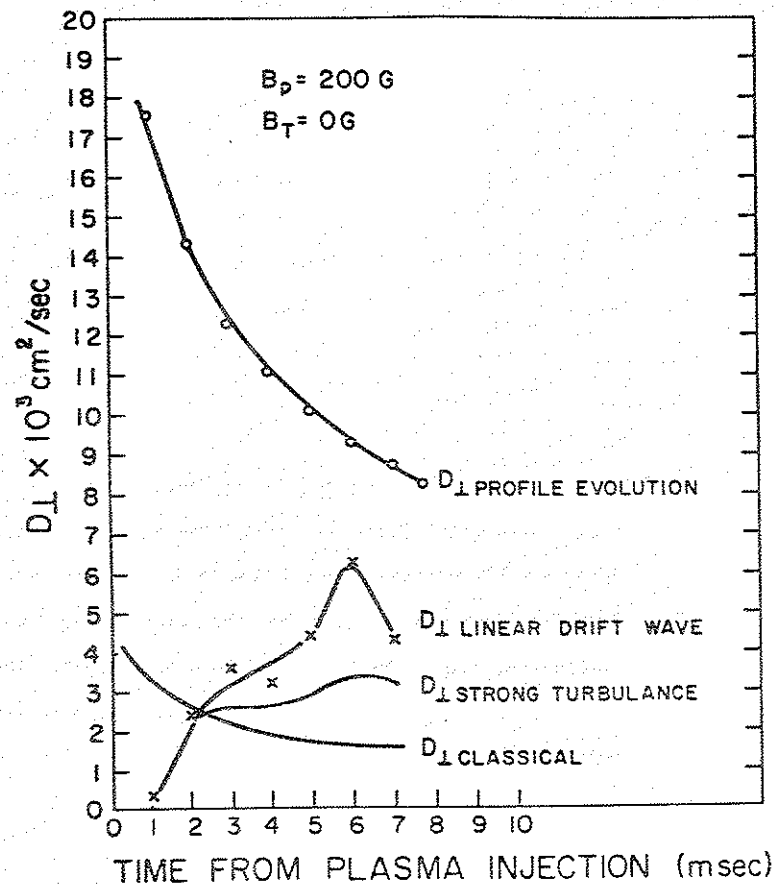

Fig. 15. The time resolved diffusion coefficients for the magnetic field configuration: $B_{p\text{-average}}(\psi = 4) = 1$ kG, $B_T = 300$ G is shown here. The diffusion coefficient calculated from the profile evolution was the actual diffusion coefficient governing the plasma transport at $\psi = 4$. The other diffusion coefficients are shown to indicate to what extent the drift wave portion of the fluctuation spectrum contributes directly to the diffusion. The classical diffusion coefficient is shown for a reference.

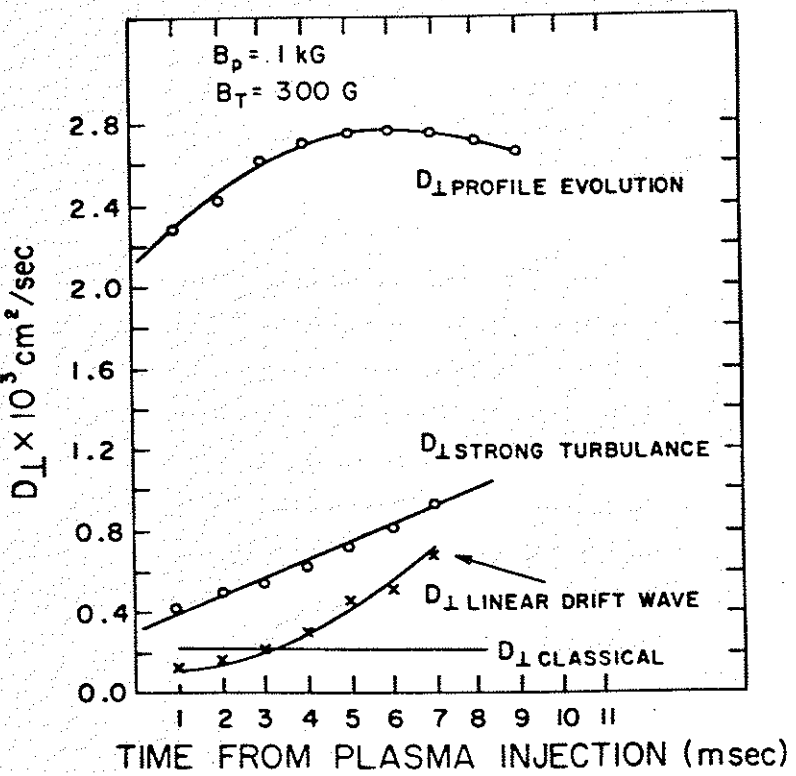

Fig. 16. The magnitude of transport at different magnetic field strengths (and the associated differing trapped plasma density and temperature) are summarized in this figure. The particle confinement time is the profile average particle confinement time. The plasma β is also displayed. The time at which these calculations were made was 3.5 msec after plasma injection.

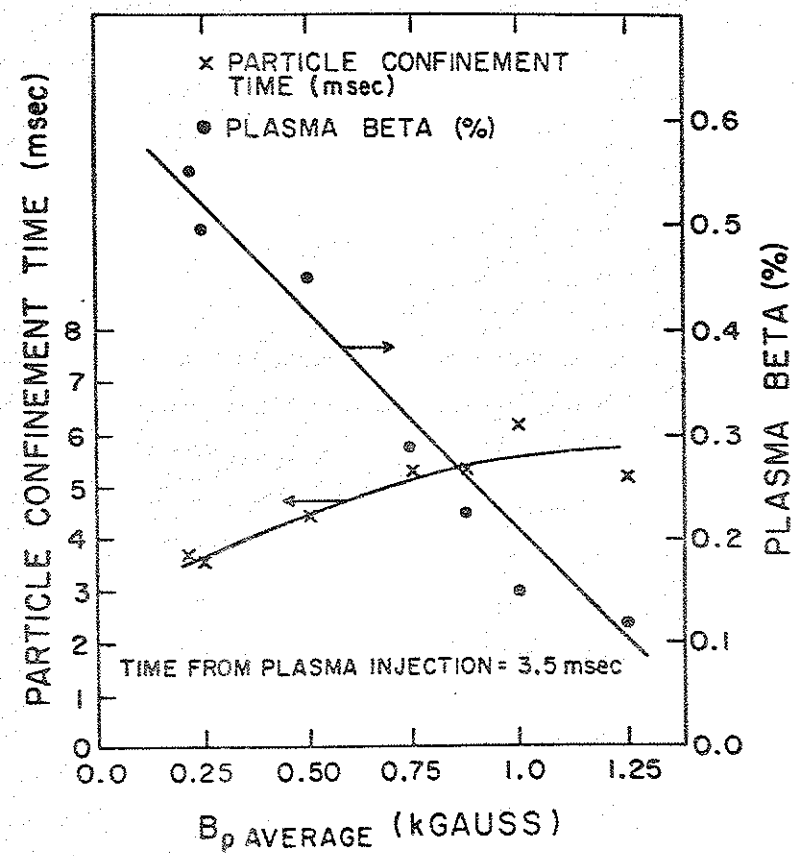

Fig. 17. The magnitude of the diffusion attributable to the drift wave turbulence is compared with the actual diffusion coefficient at various poloidal magnetic field strengths. The magnitude of the classical diffusion coefficient is shown for a reference. Note, as the strength of the poloidal magnetic field was changed the initial trapped plasma density and temperature changed. This data was taken at 3.5 msec after plasma injection.

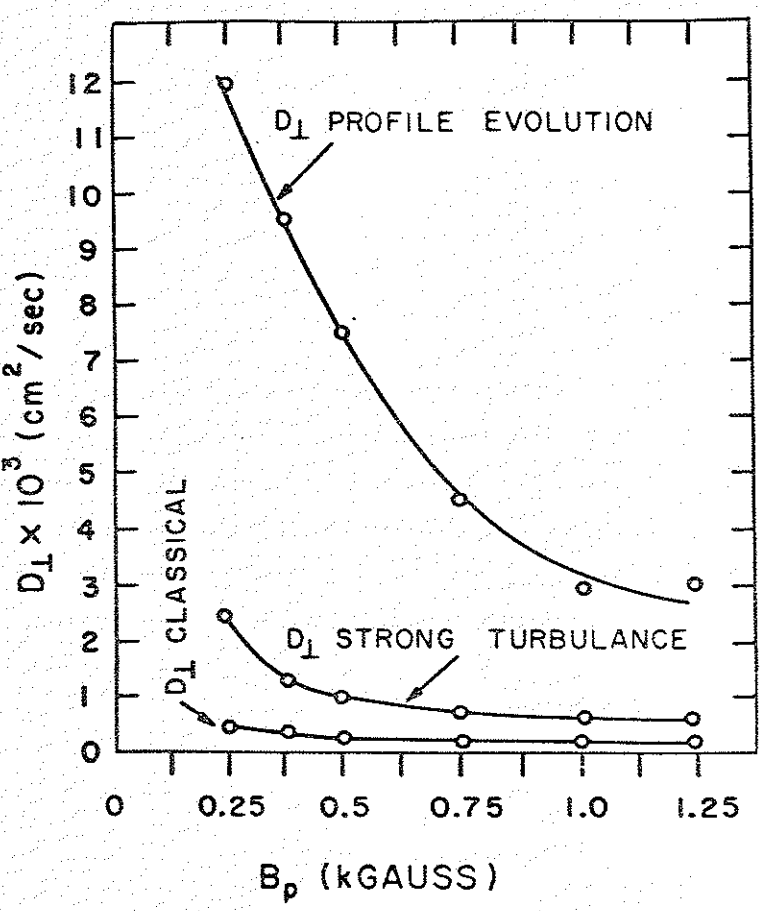

Fig. 18. The turbulent and viscous damping times are shown here as a function of time for the two magnetic field strengths, $B_{P\text{-average}}(\psi = 4) = 200$ G, and $B_{P\text{-average}}(\psi = 4) = 1$ kG. There was no toroidal field.

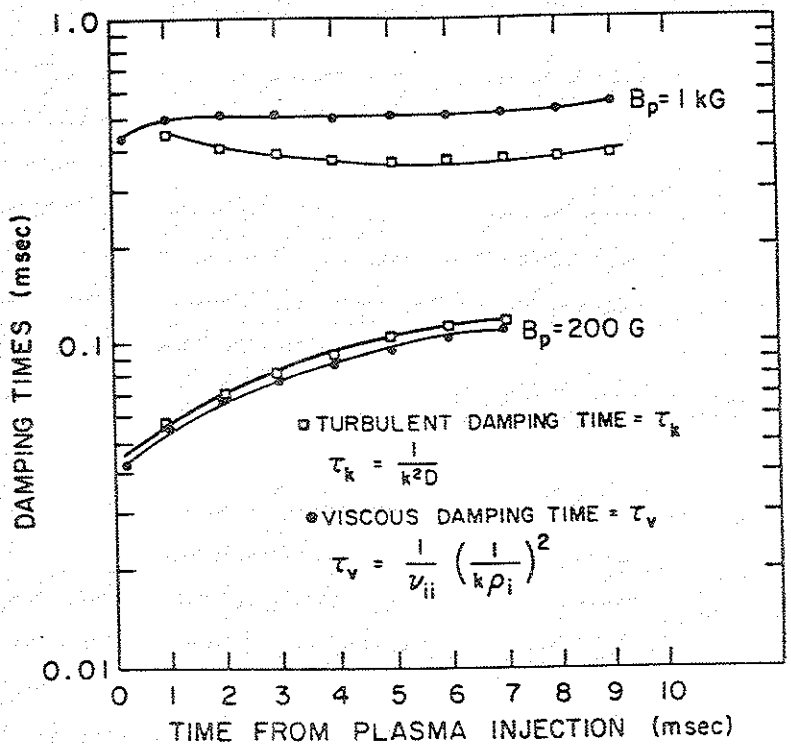

Chapter 6

Electron Heat Transport

Plasmas, which have a measurable radial electron temperature gradient, have been produced in the Octupole. The plasmas produced by the "intermediate density" gun, $n = 5 \times 10^{12}$ cm^{-3}, $T_e \sim T_i \sim 30$ eV, were seen to cool more slowly ($\tau_{T_e} > 2$ msec) on the separatrix than near the plasma edge. With the installation of the "intermediate density" gun, came, for the first time, plasmas with sufficient energy--density (nT_e) to burn through the neutral hydrogen refluxing from the walls. This behavior was attributed to the fact that the "intermediate density" gun was designed to have a much higher gas-conversion efficiency. The gun converts greater than 90% of the gas puffed into the gun into plasma.

Prior to the installation of the "intermediate density" gun, two other Marshall guns were used to inject plasma into the Octupole. Plasmas produced by these guns were never observed to have a radial electron temperature gradient[1]. The "small" gun, mounted atop a drift tank, produced plasmas in the 1×10^{10} cm^{-3} density range. These plasmas had hot ions ($T_i \sim 10$ eV) and cold electrons ($T_e \sim 2$ eV). The neutral mean free path was large compared to the plasma dimensions. Therefore, no neutral

density gradients existed. The plasma cooled down uniformly by neutral ionization and excitation of hydrogen. The "big" gun produced higher density plasmas, $n > 1 \times 10^{12}$ cm^{-3}. It's plasmas were cold, $T_e \sim T_i \sim 1$ eV, and were, therefore, unable to sufficiently ionize the background gas produced by neutral hydrogen refluxing from the walls so as to form an electron temperature gradient. This plasma also cooled uniformly from excitation and ionization of the background hydrogen.

The high energy--density plasmas produced by the "intermediate density" gun opened up a whole new avenue of research. The existence of temperature gradients indicated that this plasma was very near to breaking through the neutral cooling barrier, at least in the central core of the plasma, on the separatrix. This encouraged research to attempt to understand the creation and maintenance of the temperature gradient, to observe diffusive and convective electron heat transport, and to see if any heat loss effects could be correlated with the density fluctuations. This research eventually necessitated the development of a neutral transport code and an electron heat transport code, which were used to accurately model these new plasmas. Results from the heat transport modeling also allowed a closer estimate of the affect of neutral refueling on the measured density profiles used in the particle transport studies.

The same technique employed to analyze the actual particle transport was used to analyze the electron heat transport. As before, the analysis procedure has two parts. First, the time-dependent electron temperature profiles and the time dependent ion densities were measured in the machine. Second, the electron heat transport equation was solved in one dimension using the numerical code, TEVOL.[2] The parameters within the code were adjusted to make the numerically predicted electron temperature profile, and other associated outputs, agree with the actual data taken in the Wisconsin Levitated Octupole.

Electron Temperature Profiles

The electron temperature profiles were measured with admittance probes. A platinum-tipped double probe, located in the bridge region of the lower outer hoop of the Octupole, was moved radially to measure the electron temperature on different Psi (ψ) surfaces. As described in Chapter 2, the double tipped probes measured the ion saturation current with one tip and the sheath admittance (reciprocal of sheath resistance) with the other tip. From this information, the electron temperature was calculated. As an independent check, a single Langmuir probe's bias voltage was swept to trace out the I-V curve. The electron temperature calculated from simple Langmuir probe theory agreed with that obtained from the admittance probe.

Ion temperatures were taken on the separatrix with a gridded energy analyzer. The ion temperature was equal to the electron temperature to within an 1 eV, which was the experimental error, for all plasmas under study. This result was expected, since the equilibration time, which is approximately ν_{ei}^{-1}, was less than 10 μsecs.

Two different plasmas were studied extensively. One plasma was contained in a 1.25 kG poloidal field (average at $\psi = 4$) with no toroidal field. This plasma was made with the "intermediate density" gun operated in its hot plasma mode and is designated a "low β" plasma (Fig. 1). The plasma had a $\beta = nT_e/B^2 < 1\%$ on the separatrix in the bridge region of the machine. The hot plasma mode, also called the gas-starved mode, was achieved by adjusting the amount of gas puffed in the gun, and the time between when the gas was puffed in and when high voltage was applied to break down that gas within the gun. This mode injected plasma which once trapped in the 1.25 kG poloidal field, had electron and ion temperatures to 30 eV but at relatively low densities, $n = 1.7 \times 10^{12}$ cm^{-3} (at 1.0 msec after injection).

Note that the electron temperature peaked inside the separatrix, and that, at 1 msec, a large ($\Delta T_e = 15$ eV) temperature gradient existed between $\psi = 4.75$ and the internal

ring surface. The ring surface is at $\psi = 2.5$, in close proximity to the plasma. The outer wall boundary can be closely approximated by $\psi = 9.0$. From the standpoint of a neutral refluxing from a wall or ring, the plasma was physically situated closer to the ring. This, combined with the fact that particle loss rate, the flux tube volumes, and other geometric factors were different on the inside and outside of the separatrix, accounted for the difference in temperature gradient magnitudes on either side of the separatrix. This plasma was the most interesting from a heat transport point of view since it exhibited high temperatures and large temperature gradients.

The second plasma, whose heat transport characteristics were studied was designated a "high β" plasma since it had a beta on the separatrix in the bridge region of 8%. (Fig. 2). This value of β was achieved by lowering the poloidal magnetic field as much as possible while keeping the trapped plasma as dense and hot as possible. This plasma was characterized by electron temperatures to 14 eV and densities to 6×10^{12} cm^{-3} at 0.5 msec after injection. The poloidal magnetic field strength was 160 G. There was no toroidal field.

The high β plasmas were injected by the "intermediate density" gun operated in a mode which differed slightly from the standard operating mode. The modified mode produced higher

density plasmas compared to those produced in the standard operating mode, for a given poloidal magnetic field strength. This was done by puffing in more gas than normal and running the gun at higher voltages (i.e., higher power input into plasma during breakdown in the gun).

The "high β" plasma closely resembled the low field (B_p = 200 G) plasma studied in Chapters 4 and 5. Only mild temperature gradients were measured in this plasma. The plasmas, whose particle transport properties were studied, were injected by the intermediate density gun in its standard operating mode. Statements made about the particle balance (in particular, refueling) in these "high β" plasmas, mentioned in the previous paragraph, and to a large extent in the "low β" studies, can, therefore, be applied to the plasmas upon which particle transport and fluctuation induced transport experiments were conducted.

The profiles just displayed were taken at a 45° toroidal angle in the bridge. The machine was being well gettered; i.e., fresh layers of titanium were being deposited by the six symetrically located (toroidally), evaporable getters.[3] The titanium atoms deposited on the walls between shots was 10 times the number of hydrogen atoms injected per pulse. Profiles were taken at other asimuthal locations around the machine for the

same operating conditions. Electron temperatures measured near the plasma boundary ($2.5<\psi<3.5$, $6.5<\psi<7.0$) varied by as much as 3 eV at different asimuthal angles. Temperatures near the plasma interior were constant at different asimuthal angles. This temperature variation was correlated with the local surface conditions in the Octupole. In regions where the titanium deposition was greatest, the temperature on the flux line near that region was highest. This behavior was further confirmed by selectively turning off the getters in certain quadrants of the machine. After many shots the local temperature profile, taken in the quadrant where the getters had been shut off, became more peaked, i.e., the temperature near the boundary would drop by approximately 3-5 eV. This behavior was seen for each of the 3 asimuthal angles in which measurements were made: 45°, 225°, and 330°. The profiles just shown are therefore approximately equal the asimuthally averaged profiles within 3 eV. This is especially true when the machine has been symmetrically coated with titanium.

The non-asimuthally symmetric temperatures near the plasma edge were reduced to less than 1 eV (error bar for comparing temperatures from two probes for a given shot) when a small toroidal field was added. A toroidal field strength of 50 G was sufficient. It is presumed that the local surface asymmetries, and thus the local neutral reflux rate asymmetries still

existed. However, good thermal connection around the machine was established by opening up the poloidal field lines, converting them into surfaces. Opening up the field lines changed the response time for heat transport, among the local electron temperature non-uniformities, from perpendicular drift or diffusion time scales to parallel diffusion time scales, which are much faster.

For all plasma conditions, with and without toroidal field, to within the accuracy of measurement, it was confirmed that no electron temperature gradients existed along field lines.

All the above mentioned characteristics indicated that perpendicular (radial) electron heat transport and profile formation was not principally due to direct heat diffusion. Instead, it showed that the electron temperature profile formation was still dominated by cooling from neutral ionization and excitation. The results also strongly suggested that the profile shape was governed by local wall conditions which determined the neutral reflux rates. The lower temperatures near the plasma boundary were attributed to a class of neutrals, i.e., slow, low energy H and H_2 neutrals, which had mean free paths shorter than or approximately equal to the plasma size. These neutrals caused a greater heat loss near the plasma edge where their density was greatest.

A neutral transport model was developed since neutral ionization and excitation was determined to be the dominant heat loss pathway for the electrons. This model was used to calculate the spatially dependent H and H_2 densities, in order to calculate the heat loss rate.

Neutral Transport Model

The arguments made above regarding the preservation of axisymmetry during heat loss through symmetric titanium depostion were used to justify ignoring the θ coordinate in the modelling. This reduced the neutral transport problem to two dimensions, but also restricted its direct applicability to well gettered, symmetrically titanium-coated machines. As mentioned above, in a well gettered machine, only temperature gradients in the radial, $\hat{\nabla}_\psi$, direction were observed. Since neutral ionization and excitation were apparently responsible for the temperature gradient formation, the neutral transport will be further reduced to one dimension by averaging along the poloidal projections of the trajectories of neutrals backscattering from a surface. The angular distribution for backscattering neutrals from a surface is known. The results of the averaging will be discussed shortly. Since no electron temperature gradients along field lines were seen, or expected, and since the neutral

transport problem could be modeled in one dimension, the whole heat transport problem could be reduced to one dimension.

The neutral hydrogen population was broken up into three groups in the numerical model. The three groups, the fast atomic hydrogen, the slow atomic hydrogen, and the slow molecular hydrogen; and their interactions with themselves and the plasma are pictorally represented in Fig. 3. This chart can be best understood by following a neutral from the time it is born, until it either sticks to the wall, or is reionized by the plasma.

Plasma ions that are lost from the magnetic confinement regions, either during injection (i.e., plasma which is not trapped), or due to perpendicular diffusion strike the walls of the Octupole. The distribution of ions striking the wall at different positions in the Octupole has been measured by A. Cavallo, using striped particle collectors.[4] All but a few collectors have been removed from the machine, so a complete scan of the ion flux to the walls was not possible. With the few collectors remaining, a comparison of particle fluxes in these high density plasmas ($n > 10^{12}$ cm^{-3}) to the fluxes observed in low density ($n < 10^{10}$ cm^{-3}) plasmas studied by Cavallo, indicated that the ions lost to the walls had not redistributed themselves to different wall sectors. The plasma

was still lost principally to regions in the Octupole which can be thought of as "limiters" (see Fig. 4). These "limiters" are regions where magnetic field lines intersect the wall. In the limiter regions, the surfaces were well gettered. That is, more than 90% of their surface area was coated with titanium in sufficient amounts to guarantee they were never saturated with hydrogen during the course of these experiments. The energy and particle backscatter coefficients as a function of particle impact energy were known. For our ion temperatures, approximately 50% of the ions striking the titanium coated surface backscattered as neutral atomic hydrogen, the remainder stuck to the surface.[5]

The neutral transport code used in this heat transport experiment was fashioned similar to the neutron transport multi-group codes used to study reactor physics. The fast neutrals, whose mean free paths were large compared to the plasma dimensions, had no spacial dependences. The fast neutrals do, however, change their energy significantly as they slow from plasma energies. At each time step in the code the ions backscattering from the wall as fast neutrals, and the succeeding backscatter and charge exchange events determine the partitioning of the energy space since the energy of a neutral at any time can be calculated because its starting energy and number of interactions with the wall were known. When the fast

neutrals (followed in a 1-D energy space) backscattered from the wall with an energy less than or equal to 1 eV, then they were moved into the slow neutral group. The slow neutrals, on the other hand, had a spacially varying density, but did not change their energy significantly on impact with the wall. The slow neutrals were, therefore, assumed to have an energy of 1 eV (i.e. they were single speed) and their density was calculated on a 1-D grid.

The ions which were lost from the plasma were assumed to have an energy, $E = T_i$. They were also assumed to be distributed on the various wall surfaces in the same proportions as measured with collectors by Cavallo.[4] This information was necessary since the titanium surface coating is not uniformally distributed. This would affect the value of the backscatter coefficients of the ions for their first interaction with the wall. The fast neutrals which backscatter were assumed to be able to go to any surface after this first interaction. This means that the number of fast neutrals striking any surface area was assumed to be constant (with respect to area, not time).

The 1 D grid for the slow neutral group was subdivided into 0.25 Dory units in Psi (ψ). The grid points had different physical spacings (Δx in cm) between each point. The value of Δx was calculated from the graphic averages of rays (neutral

trajectories) emerging from each surface. Each of the rays, one every 10 degrees of arc (18 total per position), drawn from up to three positions on a surface, were weighted by the surface area and by a cosine(θ) distribution. Theta (θ) is measured from the surface normal, and cosine(θ) represents the distribution of particles backscattering from the surface.[5] Up-down symmetry of the Octupole was assumed.

Trajectories (rays) for the neutrals were made in both the toroidal and poloidal planes of the Octupole from flux plots and machine drawings. These were then averaged together and mapped into two groups, representing neutrals moving in the two corresponding directions, away from the hoop surfaces and away from the wall surfaces, in the 1-D space. From this, tabulated averages were made for the quantities necessary to physically represent the neutral motion in 1-D. These were: the average velocity dotted into the vector, $\nabla\psi$, (the 1-D space direction) which represents the speed that a 1 eV slow neutral has in that direction; finally, the average spacial distance, Δx, between each of the grid points.

Using this 1-D grid and averages, the slow neutral density can be calculated at each point. The slow neutrals are produced at the wall and lost at each grid point due to ionization or charge exchange. This is the essence of the slow neutral

transport sections of the code, TEVOL. This code will be discussed further in the next section.

The neutral, fast atomic hydrogen backscattered from the wall had an ionization mean free path which was large compared to the plasma dimensions. Therefore, its density was uniform throughout the vacuum chamber. The average mean free path for these fast neutrals was several meters, compared to the average plasma dimension of approximately 10 cm. As the fast atomic hydrogen neutrals bounced between the titanium coated walls (Fig. 5), they had a probability for sticking to the wall on each interaction. This probability was proportional to their impact energy. The fast neutrals which have backscattered from the walls have lost a known amount of energy during the backscatter process.[5] Fast neutrals which have backscattered can then enter the plasma containment region, where they either pass through the plasma unaffected, or are ionized or charge exchanged by the plasma.

The numerical subroutine, SLOW, calculated the relative probabilities that a lost plasma ion would stick to the wall, would emerge from the wall as a neutral and be reionized or charge exchanged, or would lose energy and become part of the slow hydrogen group.[6] For our typical plasmas, a summary of the functional dependence of each of the three above mentioned

pathways, averaged over the lost plasma ion lifetime, is shown in Figs. 6 and 7. The total probability that a "plasma ion" neutral will stick to the titanium coating during its many interactions with the surface as it loses energy, from plasma energies ($E \sim T_i \sim T_e$) to 1 eV was called the net absorption coefficient. It should be noted from Figs. 6 and 7, for our typical plasma parameters, $T_e \sim T_i \sim 25$ eV, $n \sim 2 \times 10^{12}$ cm^{-3}, that approximately 80% of the ions lost from the plasma stick to the wall. The remainder of the ions which have backscattered as neutrals were either reionized or slowed down to thermal speeds (1 ev). Less than 1% of the neutrals survive the energy loss process and slowed down to less than 1 eV. The remaining 20% of the lost ions recycled. It is this figure, 20%, which was used as the uncertainty in the particle confinement time calculations in Chapter 5. Although recycle occurred from all three neutral groups, the fast H group was responsible for greater than 90% of the recycle.

The slow atomic hydrogen group had two sources. The first, as has already been mentioned, was the group of fast hydrogen atoms which survived slowing down. The second group consisted of Frank Condon neutrals created at an energy of approximately 1 eV during the ionization of an atom in a H_2 molecule. There were three sinks for the slow hydrogen atoms. Most of the hydrogen atoms picked up a second, loosely bound atom on the

surface, and became a member of the slow H_2 group. Some of the atomic hydrogen stuck to the wall. The remainder was reionized or charge exchanged, then becoming a member of the fast hydrogen group. The slow atomic hydrogen atoms had mean free paths which were approximately equal to the plasma dimensions, so they contributed to the radially uneven electron heat loss and thus to the temperature gradients which were observed.

The slow molecular hydrogen group also had two sources, one being the H_2 evolving from the surface when a slow atomic hydrogen atom interacted with the surface. The other was background H_2 gas remaining from the previous shots. Only 55% of the vacuum volume of the Octupole was filled with plasma upon injection. The background gas in the plasma containment region was quickly burned through; i.e., almost completely ionized in less than 1 msec after injection. The remainder of the background gas, in the vacuum volume, where no plasma was contained, could then enter the plasma containment region and contribute to the formation of the temperature gradient immediately after plasma injection. The slow H_2 group had two sinks. One was ionization by the plasma, which was accompanied by the creation of a Frank Condon neutral. The second was sticking to the titanium-coated wall.

It was assumed that this neutral transport model reasonably calculated the time-dependent, radial neutral populations. The neutral density at the wall, outside the plasma confinemnent region, was measured using fast ionization gauges. For each case studied, this measured neutral density was equal to the value predicted by the neutral transport code, at that position, to within 5%. The results from the neutral transport code were used to calculate the neutral ionization and excitation heat loss rate term in the electron heat transport equation.

Solutions to the Energy Transport Equation

The electron heat transport equation was solved numerically using the computer code, TEVOL. The inputs necessary to run the code were: the initial temperature profile, the background pressure before plasma injection, and the time dependent, experimentally measured density profile. The initial temperature profile was chosen to be flat, as one would expect upon injection. A "tailor made" profile would have yielded better agreement with the first experimental temperature profile, but this would have required changing the initial conditions for each case, which could not be justified. There were many unknowns regarding the plasma injection, trapping, and equilibration processes. What was considered more important was not how well the code predicted the first profile, immediately

following injection, but how well the model fit for all times following. Even so, the profiles predicted for 0.5 msecs, i.e. the first profiles, were in quite good agreement with the experiment.

The electron heat transport equation described in Chapter 3 has been flux surface averaged and applied to an axisymmetric Octupole. The effects which may contribute to the electron energy balance are shown in Fig. 8. The code, TEVOL, solved the heat transport equation in octupole coordinates with all these effects except impurity radiation included. The plasmas that could be accurately modeled were therefore limited to clean, sufficiently cold plasmas, where impurity effects can be ignored.

There were several reasons for leaving out impurity effects. Initial calculations indicated that the dominant electron cooling mechanism was ionization and excitation of hydrogen, for the new high density plasmas, as well as the low density plasmas made in the past. Secondly, the Octupole was not equipped with sufficient diagnostics to allow for more than a guess about the impurity effects. Thirdly, the plasmas were sufficiently cold, $T_e < 30$ eV, as to indicate that, though impurity radiation may have played a role, it was not expected to totally wash out the heat loss from the hydrogen neutral

effects. Some investigations of impurity effects were made with the output of the code. For example, $\langle Z \rangle$ was calculated by assigning any unaccounted energy loss to the impurity channel.[7]

The perpendicular heat diffusion and convection coefficient was chosen to scale like classical, $\chi_\perp \propto \frac{n T_e^{0.5}}{B^2}$, but with a multiplier that could be used to change its overall magnitude. For the cases which will be shown, the multiplier was 1.0 corresponding to classical heat diffusion in scaling and magnitude. This choice for $\chi_\perp$ gave the closest fit to the experimental profiles and the computer-predicted, time-dependent temperature profiles. It was possible to vary the scaling of $\chi_\perp$ in TEVOL as well. Computer runs were made for different scalings and overall magnitudes for $\chi_\perp$. For low values of the multiplier, ~ 1.0 times classical (in magnitude) at the separatrix, reasonable choices ($-2 \leq \beta \leq 2$, $-1 \leq \delta, \gamma \leq 1$) for the scaling did not effect the predicted profile. This was as expected, when heat diffusion was small compared to heat loss through the other channels. The data gave no indications for the selection of one scaling above another, so classical scaling was used on all further modelling. When the multiplier was increased so that $\chi_\perp > 5\, \chi_{\perp \text{classical}}$, the predicted profiles did not match the experimentally measured profiles well in shape, and the overall heat loss rate was over predicted (i.e., the temperature containment time, τ_{T_e}, was too small). This allowed

us to set bounds of the maximum value for $\chi_\perp$ at $\chi_\perp = 5\,\chi_{\perp\,classical}$ for these experiments.

Results of the modeling with TEVOL will now be shown for the two cases described earlier in this chapter.

The results of the modeling for the high field, high temperature, low density "low β" case are shown in Figs. 9, 10, and 11. These figures correspond to different times following plasma injection, 0.5 msecs, 1 msecs, 2 msec, respectively. At each time the plasma density profile, the electron temperature profile, the H_2 density profile, and the H density profile are shown. The spatially dependent diffusion and convection coefficients for $\chi_\perp = \chi_{\perp\,classical}$ are shown (labeled χ_D and χ_C, respectively). The diffusion portion of the heat transport coefficient is defined as the coefficient associated with the term, $\frac{\partial^2 T_e}{\partial \psi^2}$, in the heat transport equation. The convection portion of the heat transport coefficient is defined as the coefficient associated with the term, $\frac{\partial T_e}{\partial \psi}$, in the heat transport equation

These terms come about when the Psi (ψ) differentiation is done on the second term of Equ. 40 of Chapter 3. The spatially dependent heat loss rates (watts/cm^{-3}) for neutral ionization

(and excitation) and diffusion (and convection) are also displayed, labeled Q_n and Q_χ, respectively.

It is important to note how well the experimental and theoretical predicted time dependent profiles agree. This verifies the earlier assumption that ionization and excitation of neutrals were the dominant heat loss mechanism and that impurities play an insignificant role. The maximum unaccounted for energy loss from the electrons was calculated by taking the worst case for all the errors in the calculations. From that, a maximum $\langle Z \rangle$ for impurities was computed to be $\langle Z \rangle < 1.1$.

The computer simulation indicated that, for this plasma, the slow neutral H_2 density was reduced in the interior of the plasma to 10% of its edge density, as expected. Recall, the measurements of the electron and ion temperatures indicated that they were equal, but associated with those measurements is a possible error. The electron-ion energy coupling term (Equ. 43 of Chapter 3), Q_{ion}, was calculated, assuming the maximum error in the measurements of the electron and ion temperatures, $(T_e - T_i)$, was 3 eV. These calculations indicated that the contribution of this term was small (less than 10%), compared to the electron ionization (and excitation) term, and was therefore set to zero in the calculations. This decoupling of the electron and ion energy balances is also making a statement

about the ion energy losses. In order for the ion and electron temperatures to be equal, while the electron-ion energy exchange is small, the ion energy loss term, charge exchange, must also be equal to the electron-neutral ionization and excitation term in the electron energy balance. This is not that unreasonable when one notes that the electron ionization rates and the ion charge exchange rates are equal to within a factor of 2-3 (with the charge exchange rate being higher) in the parameter regime in which these studies were done, i.e. $5\ eV \lesssim T_e \sim T_i \lesssim 100\ eV$.[5] Also, in the parameter regime in which these studies were done, $T_e \lesssim 30$ eV, the energy necessary to do one ionization is 2-3 times T_e, while the energy loss in one charge exchange event is approximately T_i. So, for the temperature range of interest, the combination of the rate coefficients and the energy loss per event, yields ion and electron heat loss rates which are similar. The spatial averaged electron energy confinement time, over the 10 msec following plasma injection in which the experiment was being done, was approximately 3 msec. The electron energy confinement time was calculated directly from the temperature profile relaxation. The particle confinement time for this hot, low density plasma varied from 3 msec, at 1 msec. into the shot, to 5 msec. later in time (at 10 msec).

The second case, the high β case, that is shown in Figs. 12, 13, and 14 more closely resembled (in n_e and T_e) the plasmas whose particle diffusion properties were studied in Chapter 5. These figures correspond to 1 msec, 2 msec, and 4 msec after plasma injection. For this case, the poloidal magnetic field was 160 G. As expected for this high density, $n \sim 6 \times 10^{12}\ cm^{-3}$, plasma, the density profile shape was indicative of $D_\perp \propto D_{\perp\,classical}$. The electron energy confinement time for this plasma was approximately 1 msec, which was much less than the 3 msec just given for the case displayed in Figs. 9, 10, and 11. The plasma and neutral densities, and the electron temperatures were such that the ionization and excitation rates, at a given time after plasma injection, were much larger than in the low density, hot plasma case. A comparison of the density profiles of H and H_2 for the two cases showed that they had similar shapes. However, in the latter case, the neutrals were burned out (at $\psi = \psi_{sepratrix}$) to only 50% of the wall neutral density, indicating their mean free path in this plasma were longer than in the previous case. This accounts for the small temperature gradients which were observed, $\Delta T_e < 5$ eV. Again in this case, $\chi_\perp \approx \chi_{\perp\,classical}$.

Due to the insensitivity of the electron heat transport to $\chi_\perp$ (due to the relatively small amount of energy which is actually diffused away), any search for correlation of $\chi_\perp$ with

the measured plasma fluctuations would be futile. The perpendicular diffusion coefficient may have been enhanced above $\chi_{\perp\,\text{classical}}$ by plasma fluctuations to a value as high as $5\,\chi_{\perp\,\text{classical}}$, but certainly no more than that.

The major results of the heat transport studies should be reemphasized here. It was found that the major heat loss channel was ionization and excitation of H and H_2 neutrals. The perpendicular diffusion coefficient, $\chi_\perp$, is less than $5\,\chi_{\perp\,\text{classical}}$. And, lastly, impurities play an insignificant role in these plasmas.

References for Chapter 6

[1]G. A. Navratil, Ph. D. Thesis, University of Wisconsin PLP - 693(1976).

[2]H. R. Garner, University of Wisconsin PLP - 844(1980).

[3]H. R. Garner and R. S. Post, "Measurement of Low Energy Hydrogen Net Absorption Coefficient on Titanium in the Wisconsin Levitated Octupole", submitted to Journal of Vacuum Science.

[4]A. Cavallo, Phys. Fluids 19, 394(1976).

[5]G. McCraken and B. Stott, Nuclear Fusion 19,889(1979).

[6]H. R. Garner, University of Wisconsin, PLP (to be published), see also reference 3.

[7]R. Conn, et. al., University of Wisconsin UWFDM - 112(1975), pages II - A - 26 through II - A - 29.

Fig. 1. The time dependent electron temperature profiles that were measured using an admittance probe are shown in this figure for the low β, high magnetic field case, $B_{P\text{-average}}$ = 1.25 kG.

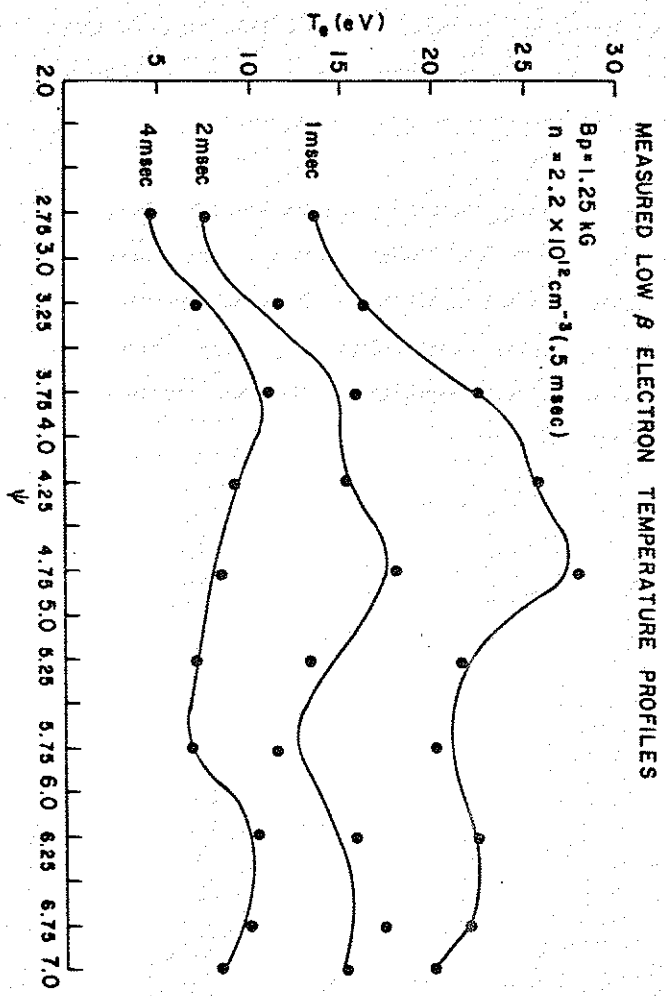

Fig. 2. The time dependent electron temperature profiles are shown in this figure for the high β, low magnetic field case, $B_{p\text{-average}}$ (ψ = 4) = 200 G.

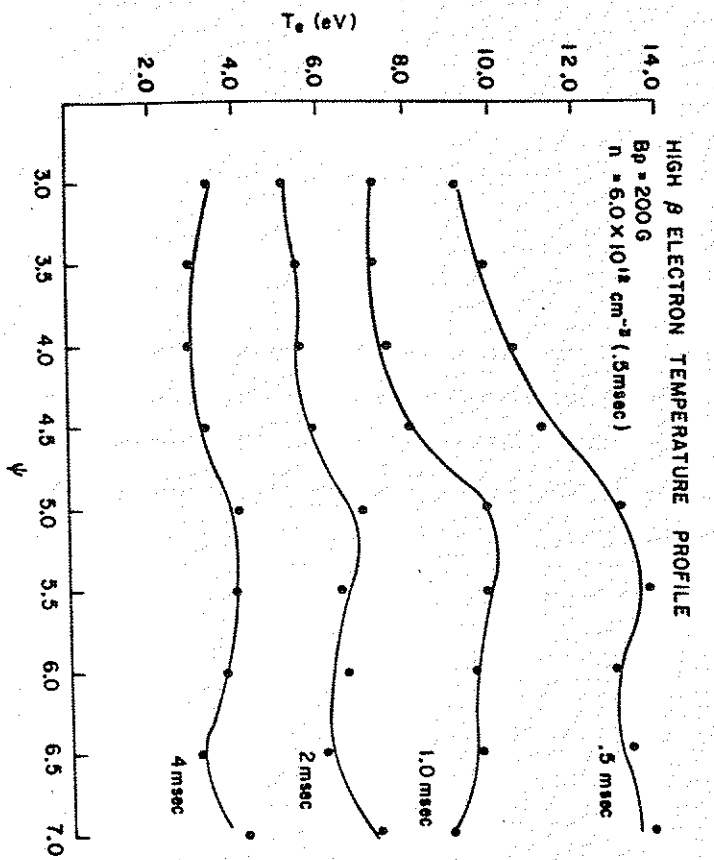

Fig. 3. This is a schematic representation of the interactions which take place among each of the neutral species (which are represented in the neutral and electron heat transport code, TEVOL), the plasma density profile, and the vacuum vessel wall.

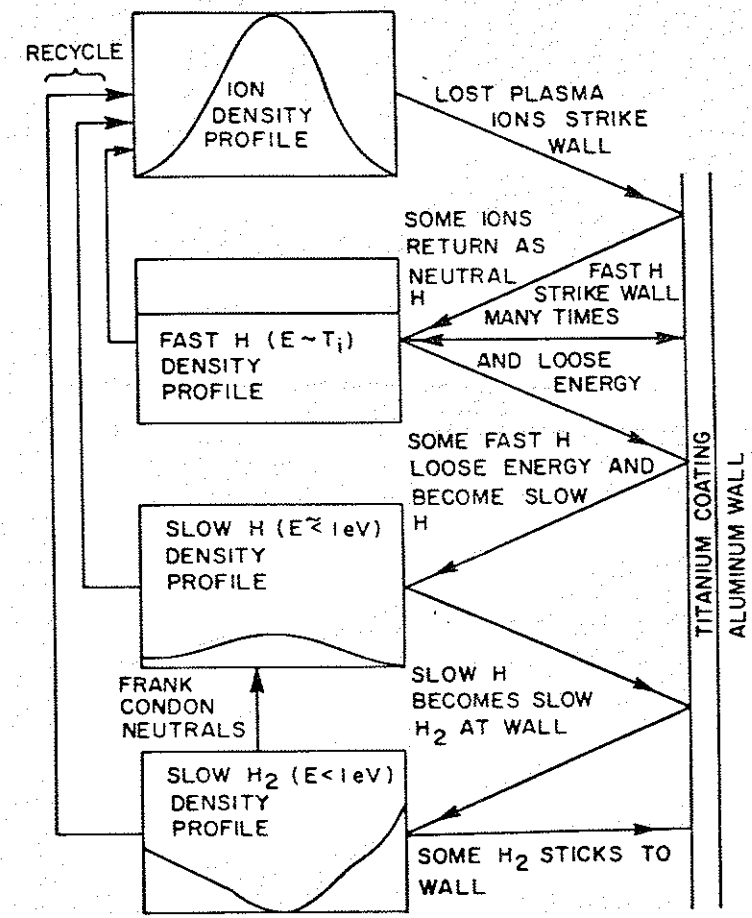

Fig. 4. This is poloidal cross section of the Octupole showing the magnetic field lines, the "limiters", and the location of the titanium getters.

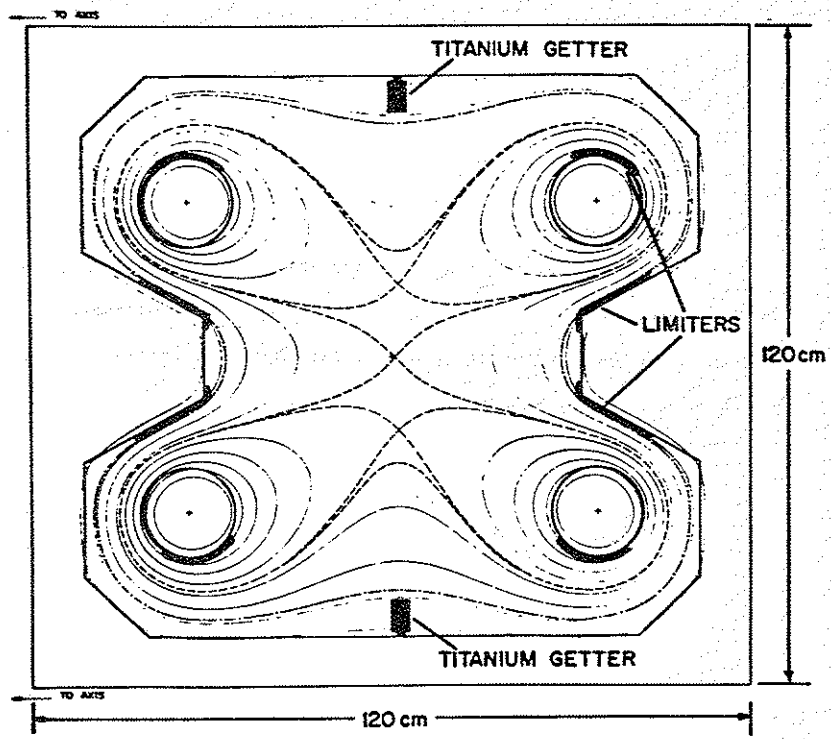

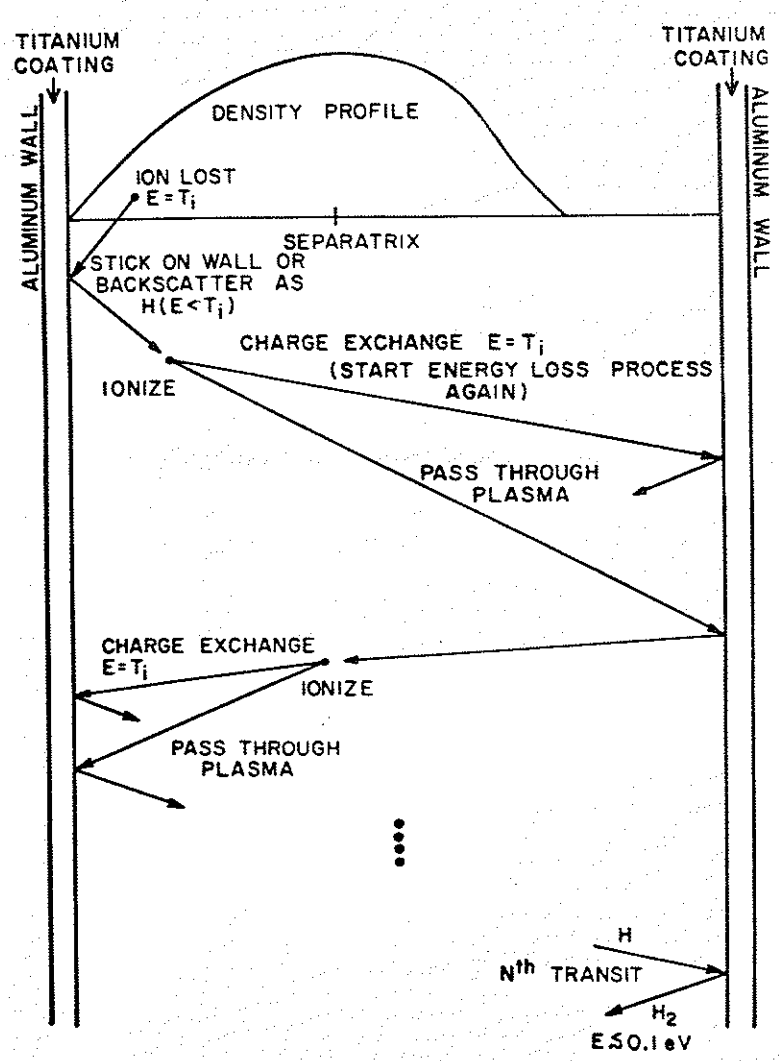

Fig. 5. This is a graphic representation of the energy loss process that an ion which was lost from the confinement region undergoes, after it becomes a fast hydrogen neutral upon striking the vacuum vessel wall.

Fig. 6. This figure gives the total probability that an ion lost from confinement in the magnetic field of the Octupole, will stick to the titanium coated walls of the torus. Note, at large densities, $n \geq 1.5 \times 10^{13}$ cm^{-3}, that most ions which strike the wall and backscatter, are reionized by the plasma on their next pass through it, and thus, an asymptotic behavior is seen.

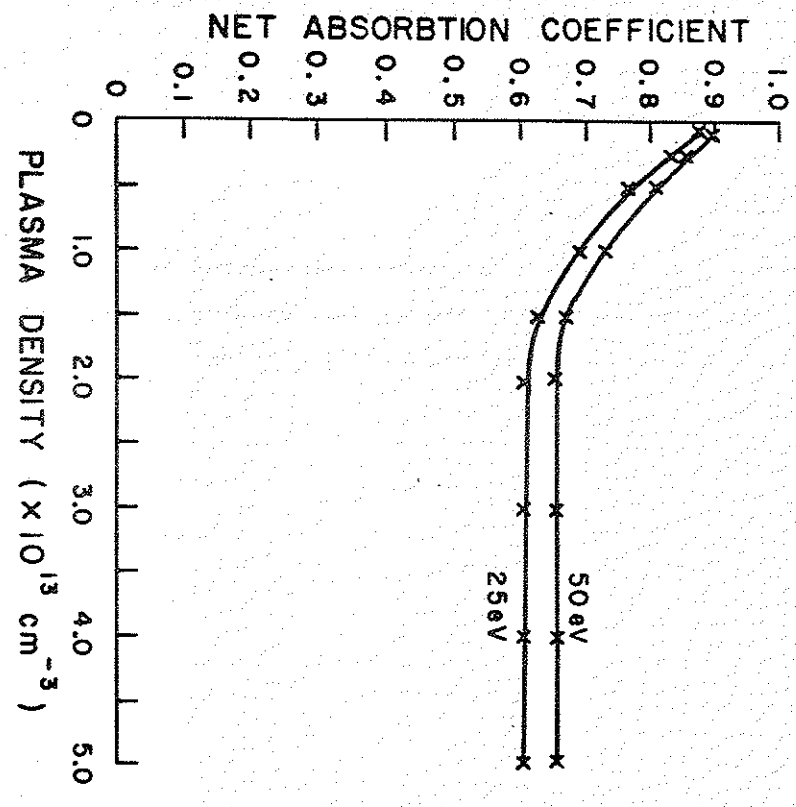

Fig. 7. This is a graphic representation of the net absorption coefficient, showing its dependence on electron temperature, for a plasma density of 5×10^{12} cm^{-3}.

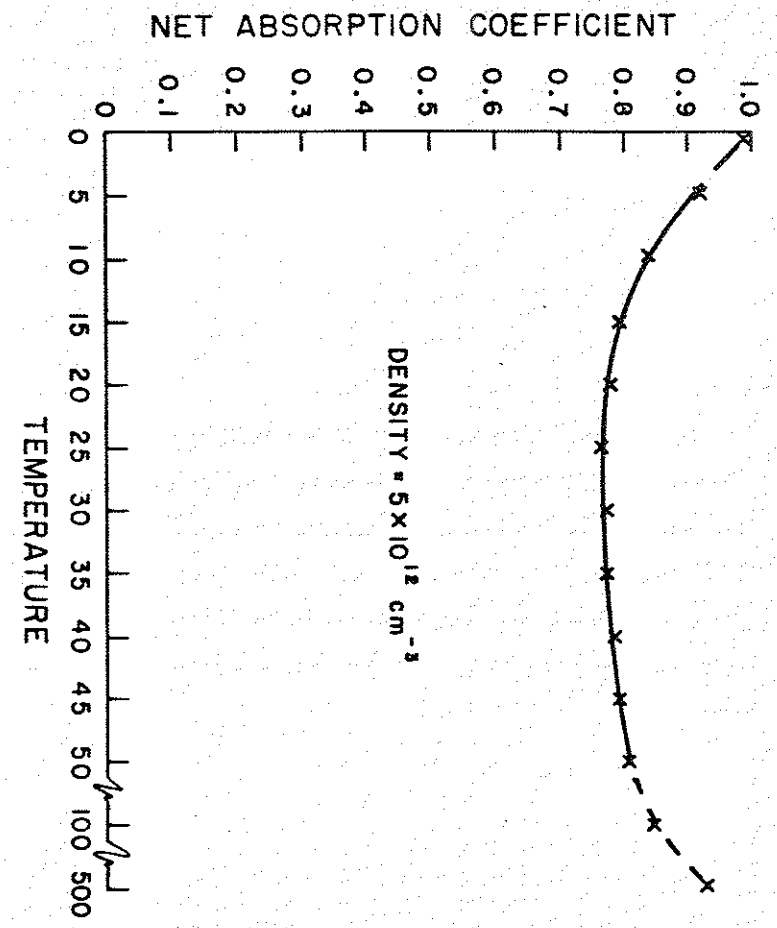

Fig. 8. This is a graphic representation of the various processes which are involved in the electron energy balance. All effects shown in this figure, except impurity radiation, are included in the calculations using the code, TEVOL.

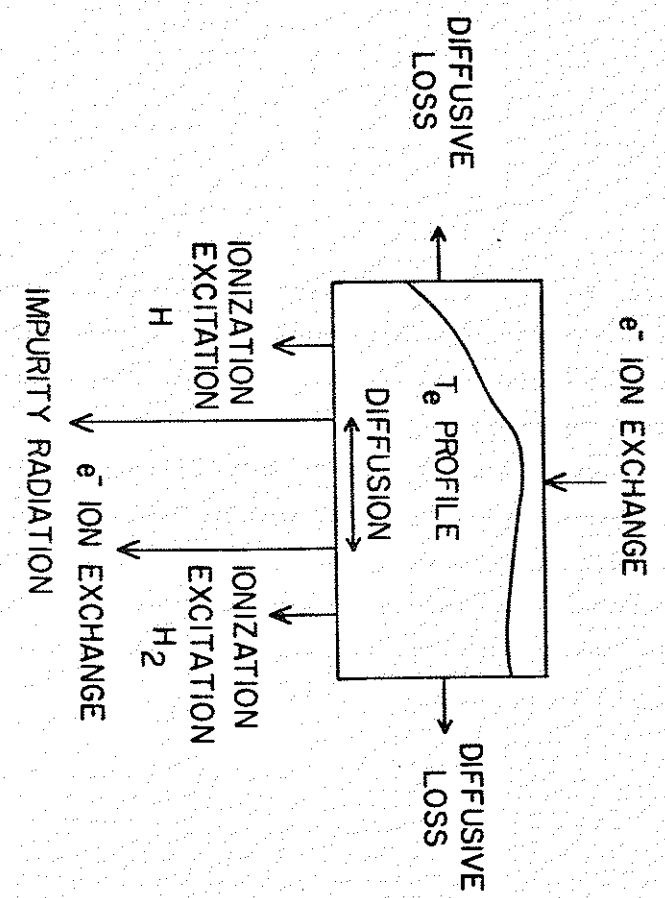

Fig. 9. Shown here are the inputs and the outputs of the code, TEVOL, for the low β, high poloidal field case which was studied. This time step corresponds to 0.5 msec after plasma injection. The ion density profile is an input. The outputs are the neutral H and H_2 density profiles, the predicted electron temperature profile, and the associated heat loss rate from neutral ionization and excitation, Q_n. The other outputs are the convective and diffusive parts to the classical heat transport coefficient (κ_c and κ_d, respectively) used in these calculations and the associated heat loss rate, Q_x.

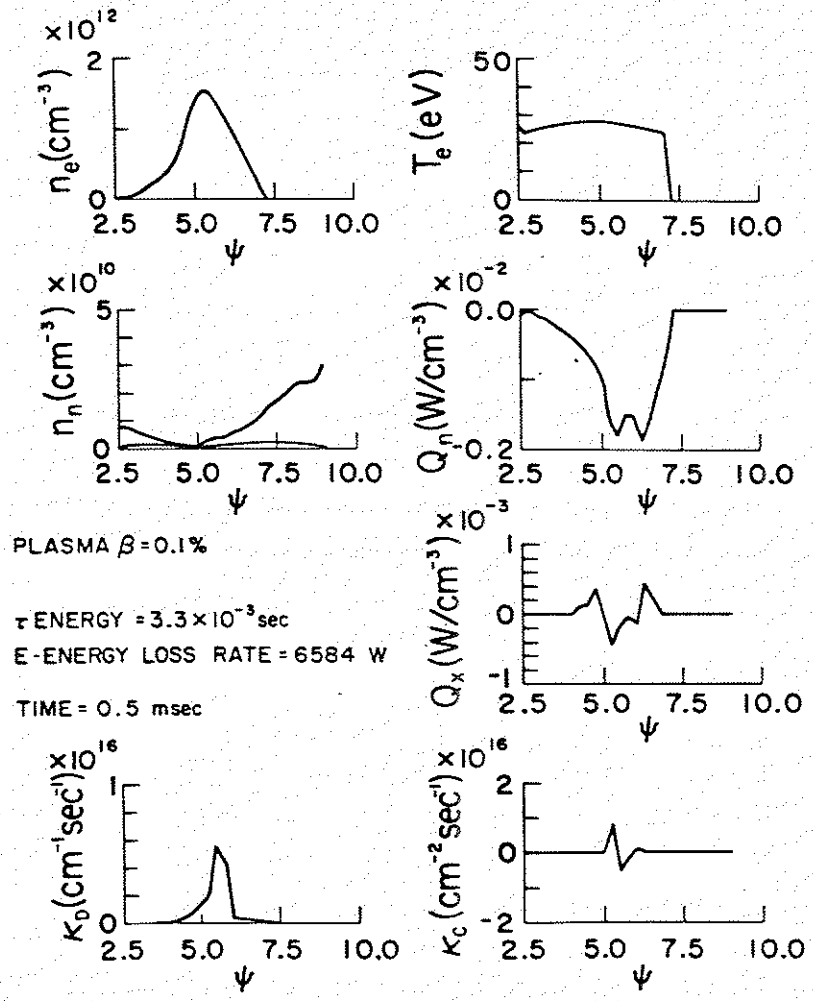

Fig. 10. This figure is for the same case as Fig. 9, but at a later time, 1 msec after plasma injection. Note the match that is made between the predicted electron temperature profile and the experimentally measured profile.

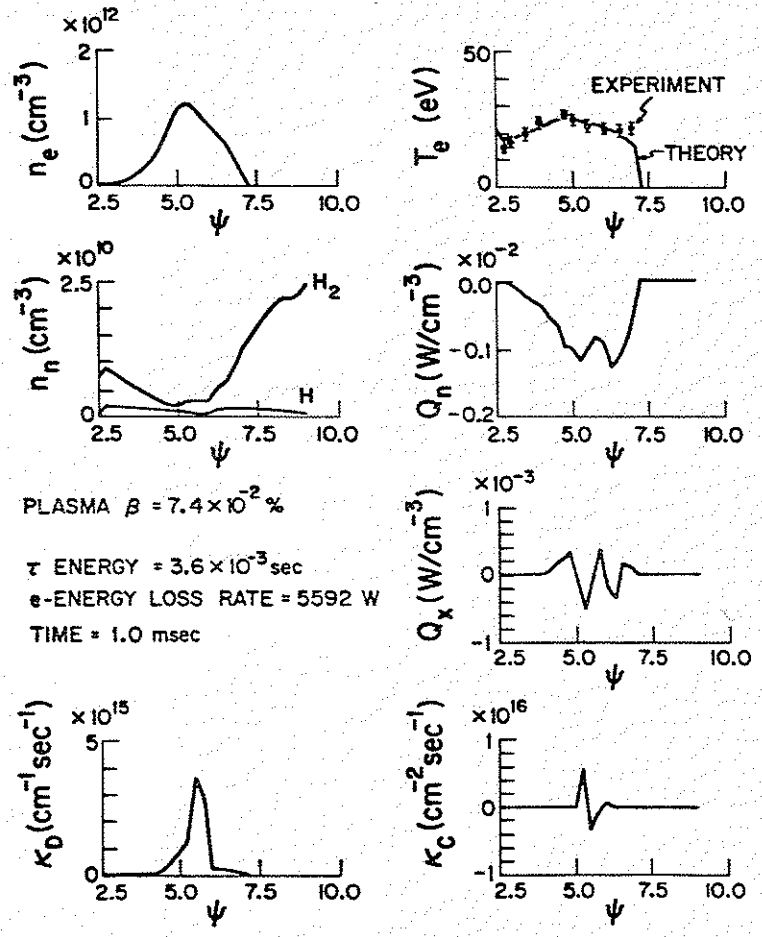

Fig. 11. This figure is for the same case as in Figs. 9 and 10, but at an even later time, 2 msec after injection.

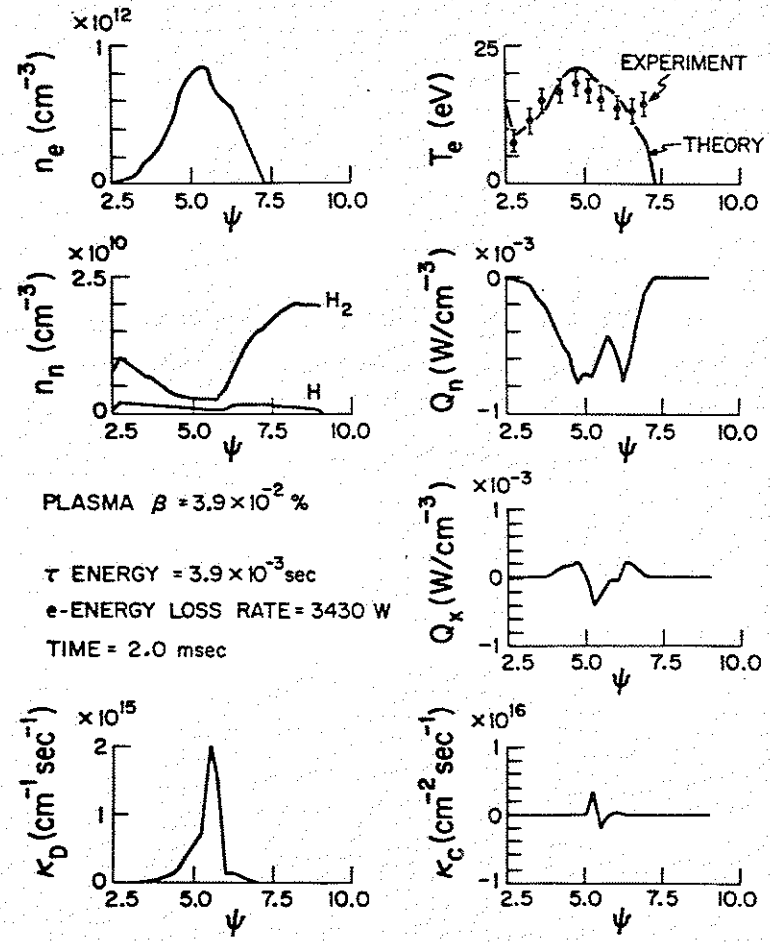

Fig. 12. These are the profiles predicted for the high β, low magnetic field case. The time step corresponds to 0.5 msec after plasma injection.

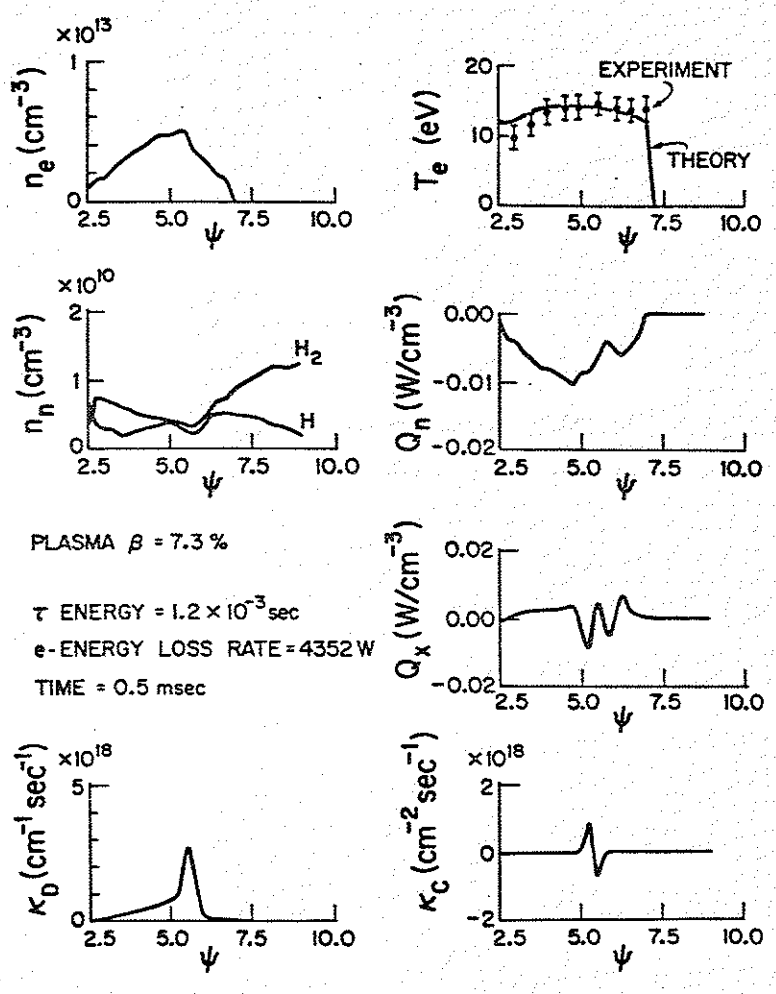

Fig. 13. This figure is for the same case as in Fig. 12, but for a later time, 1 msec after plasma injection.

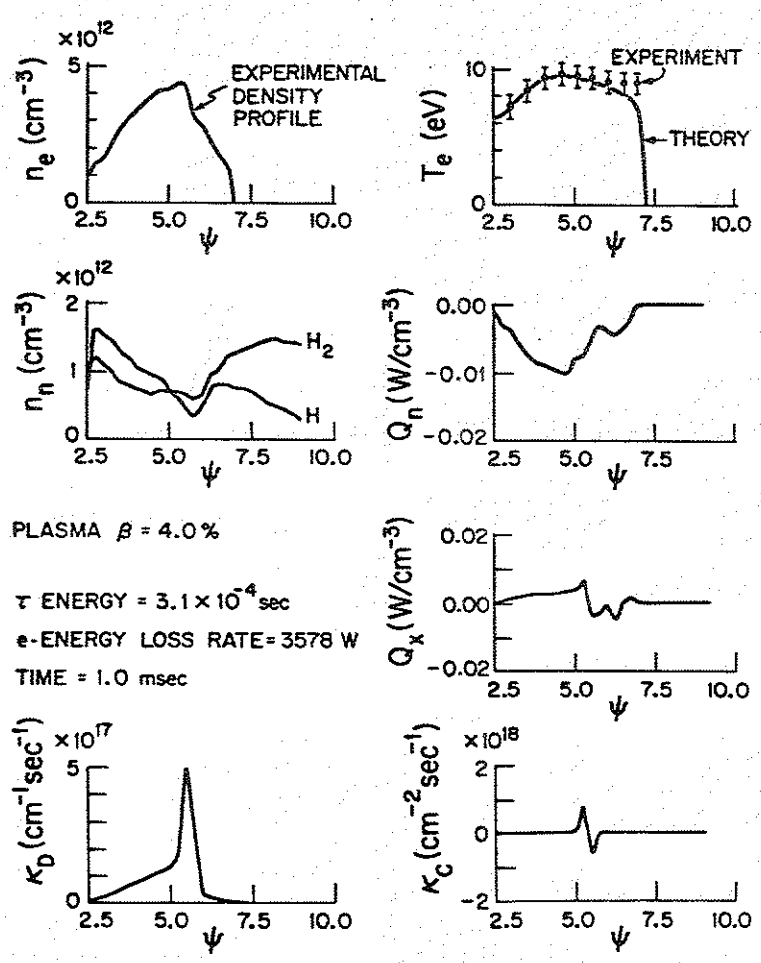

Fig. 14. This figure is for the same case as in Figs. 12 and 13, but for an even later time, 4 msec after plasma injection.

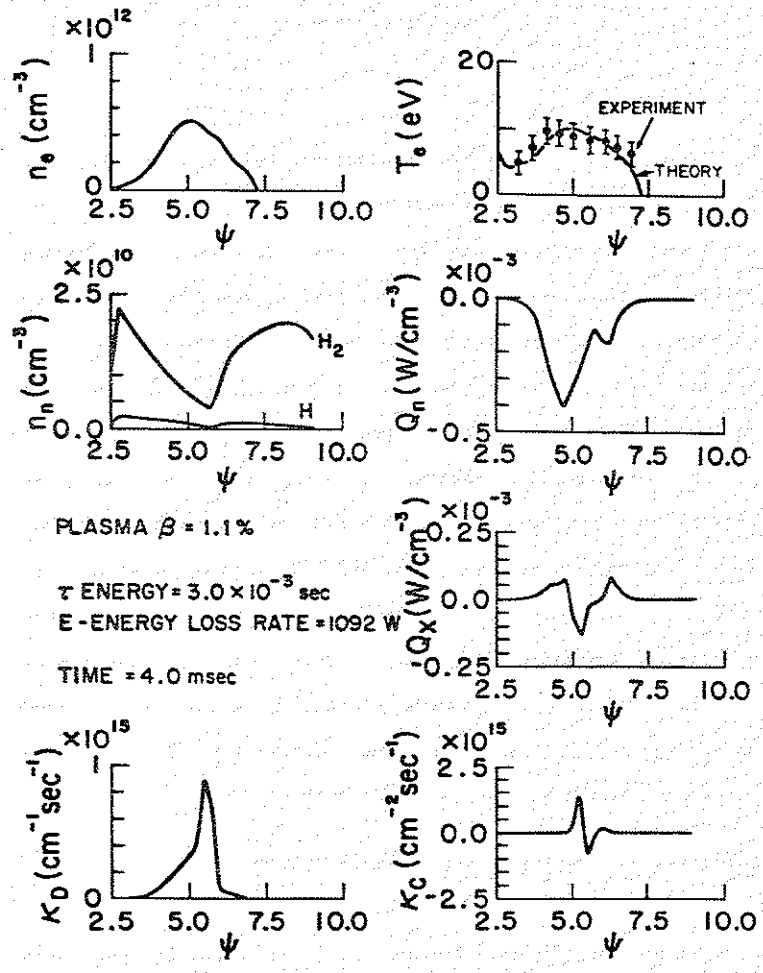

Chapter 7

Other Studies

Studies were undertaken to compare the results obtained from the Wisconsin microwave scattering diagnostic with those obtained from probes and from other microwave scattering systems. The oscillating quantities, $\tilde{I}_s$ and $\tilde{V}_f$ were measured simultaneously with $\bar{n}$ at the same spacial location in an attempt to see how well each agreed. In a different experiment the octupole was operated as an octupole-tokamak hybrid where the plasma was ohmically heated. This experiment was done in an attempt to compare the results obtained by microwave and CO_2 laser scattering systems operating on other toroidal devices with those obtained for a similar operating mode for the Wisconsin Levitated Octupole. This was an additional confirmation that the microwave scattering system was indeed operating properly and that the results were not strictly a signature for the plasmas in the Octupole.

Comparison of Scattering and Langmuir Probes

It was verified that a probe could be inserted into the center of the scattering volumes without changing the magnitude or the spectra or the density fluctuations as measured with the

microwave scattering system. The presence of a probe inside the scattering volume only caused a slight offset on the D.C. (0 frequency) output of the balanced mixers (detectors), and did not modify the operation of the system at non-zero frequencies. The typical scattering volume was approximately 100 cm^3. The probe volume within the plasma confinement region was less than 1 cm^3. Therefore one would expect that the probe should only interfere in the performance of the scattering system to a small amount ($\sim$ 1%) providing the probe does not modify the plasma oscillations.

The measurement of the ion saturation current fluctuations with probes demonstrated that the fluctuation spectrum varies both in magnitude and spectral component content, when compared to the measurements of the density fluctuations with the microwave scattering system. Furthermore, the same behavior was seen for the comparision of $\tilde{V}_f$ to $\bar{n}$. The fluctuation spectrum of the floating potential oscillations more closely resembled the fluctuation spectrum of the density fluctuations than did the spectra of the ion saturation current oscillations. Figure 1 shows a comparison of typical $\tilde{V}_f$, $\tilde{I}_s$, and $\bar{n}$ ($k_\perp = 8.67\ cm^{-1}$) frequency spectra for a poloidal field strength of 1 kGauss. The floating potential fluctuations most resembled the fluctuations having a wavelength of 0.8 cm ($k_\perp = 8.67\ cm^{-1}$). Note that there are several statistically significant peaks

which appear in both the floating potential frequency spectrum and in the density frequency fluctuation spectrum.

Fluctuation levels measured with probes were not in agreement with those measured with microwave scattering. (See Fig. 2.) Until now fluctuations in ion saturation current have been assumed to be similar or equal to density fluctuations. Only in the high magnetic field cases were the density fluctuation levels less than the ion saturation current fluctuation level. One could make the statement that the microwave scattering system was not measuring all the fluctuations, due to the finite coverage of wavenumber (k) space. However, at low magnetic fields the level of density fluctuations far exceeds the levels recorded with probes indicating that indeed an adequate coverage of k-space was made. At least one other experiment, the FM-1 spherator[1] measured fluctuation activity with both probes and microwave scattering. In all but one case, they also found that the two methods gave different results. Only when FM-1 was operated in very high shear configuration, where only one mode (at one wavelength) was unstable, did the two methods give similar results. Even then probes indicated that the fluctuation level was twice that indicated by the microwave scattering system. The results from FM-1 also demonstrated that 'the response of a probe is a sensitive function of wavelength even when the probe tip size

was small compared to the wavelengths of fluctuations under study.'

Some enlightenment can be gained by comparing Fig. 2 with Fig. 16 of chapter 5. From the latter figure it can be seen that as the magnetic field was raised, while the corresponding trapped plasma density and temperature was allowed to vary with $|B_{p\text{-average}}|$, the particle confinement was improved. If it was assumed that the high frequency, short wavelength, modes, measured with probes and the microwave scattering system, contributed to the diffusion by providing energy into low frequency, long wavelength, turbulence, one would have expected to see stronger fluctuations at lower fields where the diffusion was greater. The fluctuation level as measured with the microwave scattering diagnostic was smallest at high fields. This was consistent with the diffusion picture. Probes measured higher fluctuation levels where the diffusion was smallest which was contrary to what was expected.

In absolute magnitude of the fluctuation levels it appears that not only do the microwave scattering measurements disagree with the probe measurements, but the two measurements ($\bar{V}_f$, $\bar{I}_s$) made with the probes were different. There were indications that this was due to the unequal response of the probe to fluctuations of different wavelengths. It is generally assumed

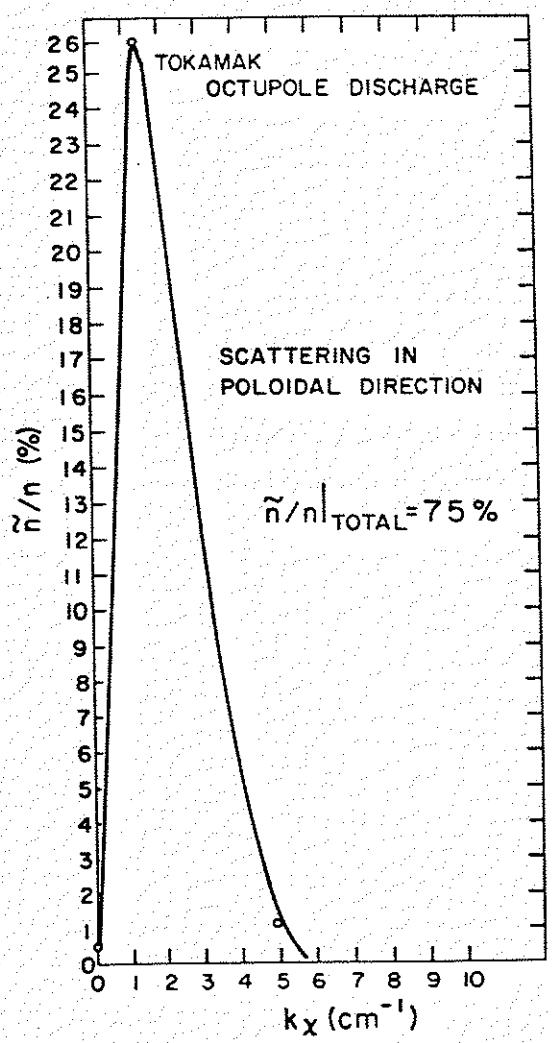

Chapter 8

Conclusions and Recommendations for Future Work

It is apparent from the data presented in Chapters 4 and 5 that the particle diffusion attributable to the measured drift wave portion of the fluctuation spectra is not enough to account for the observed diffusion. At high magnetic fields, $B_p = 1$ kG, the profile shape and its time evolution indicate that the diffusion occurring immediately after gun injection is similar to the vortex diffusion which has been observed in the Octupole in the past. The turbulent and viscous damping times for those vortex modes with a 5 cm wavelength is approximately 1 msec. Yet these modes survive for at least 10 msec, indicating that they are driven. The drift wave portion of the fluctuation spectrum directly contributes at most 20% to the diffusion. However, drift waves driven by the plasma density gradient may be indirectly responsible for the diffusion by providing energy to the longer wavelength modes (vortex modes) where it can do the most harm. At lower magnetic fields the magnitude of the diffusion is greatest. The profile shape implies classical scaling of the diffusion coefficient, $D_\perp \propto \frac{n}{B^2}$, with a magnitude enhanced above the classical value by an order of magnitude. The damping times for the vortex modes is less than 0.5 msec, indicating that they are even more strongly damped. The amount

of diffusion which can be directly assigned to the non-vortex modes (drift waves) is at most 50%. There must be vortex activity which is doing the remainder of the transport.

Unlike previous measurements on lower density plasmas ($n \sim 10^9$ cm^{-3}), the plasmas under study here, with densities $n \sim 10^{12}$ cm^{-3}, showed no improvement in confinement when shear was added. The magnitude of the diffusion coefficient was unaffected and only a 10% increase in the density profile width was noted. To within our ability to measure the frequency, the wave number and total amplitude of the drift wave portion of the fluctuation spectra were also unchanged.

The total fluctuation level, $\frac{\tilde{n}}{n}$, was measured at (ψ=4), where the density gradient was maximum. The fluctuation level ranged from 5% (at high fields) to 60% (at low fields). At high field strengths, $\bar{n}$ was constant in time. Thus $\frac{\tilde{n}}{n}$ was growing, since n was falling. At low magnetic fields, $\tilde{n}$ and $\frac{\tilde{n}}{n}$ maximized at approximately 5 msec after injection.

Time dependent density fluctuations were seen to have wavelengths of approximately 1.5 cm. Wavenumber spectra were seen to peak at $k_i \rho_i \simeq 1$, for all values of $|B_p|$. A slight k-space anisotropy was measured $\frac{S(k_\theta)}{S(k_\chi)} \simeq 0.5$.

The frequency spectra, $S(\omega)$, was seen to extend out to 150 kHz, and peaked at the lowest frequency measured, 1 kHz. There were several statistically significant peaks extending out to 50 kHz, each being considered broadband, $\Delta\omega/\omega \sim 1$. The electron drift frequency (ω_*^e) was always approximately 10 times the frequency of any of the significant peaks in the spectrum.

Electron temperature gradients were observed in the new high energy-density plasmas. These gradients were produced from ionization and excitation of H and H_2 neutrals refluxing from the titanium-coated aluminum walls. The H_2 density was largest at the walls, where it was less than 1/100 the peak plasma density. The total refueling near the plasma boundaries was small. Less than 20% of the total plasma density near the plasma boundary was reionized reflux neutrals. This ionization and excitation of neutral hydrogen accounts for 95% of the electron energy loss, giving an electron temperature confinement time of approximately 3 msec. The remaining 5% of the energy loss was shared by electron heat diffusion and impurity radiation. An upper bound on the magnitude of the heat diffusion coefficient was found to be 5 times classical. Impurities played an insignificant role in the electron energy loss; the maximum value for $\langle Z \rangle$ was 1.1. Since the electron energy loss was dominated by neutral reflux, no correlations

could be made between the heat diffusion coefficient and plasma fluctuations.

Considering the present direction of research on the Wisconsin Levitated Octupole towards higher density plasmas, the usefulness of the existing 35 GHz microwave scattering system is limited. However, much could be done at higher densities with a higher frequency microwave scattering system. As the plasma beta is approaching the theoretical MHD limit in the Octupole, it is not known why enhanced density fluctuations are not observed. Scattering at higher frequencies, and relocating the scattering volume in the bad curvature region will be essential to examining confinement in those plasmas.

Relating $(\frac{\tilde{n}}{n})_k$ to E_k for each spectra component by invoking drift wave theory is the most questionable step in calculating perpendicular plasma transport from the observed density fluctuations. This has been investigated to some extent with Langmuir probes. These investigations could be improved by measuring both $\tilde{n}$ and $\tilde{\phi}$ simultaneously and directly by using a device such as a heavy ion beam probe in conjunction with a microwave scattering system.

The results themselves bring up questions not intended to be within the scope of this thesis, but which should be given more consideration. Further research in this area should address why the addition of shear did not change the confinement or the fluctuation spectra; why the total fluctuation level, $\frac{\tilde{n}}{n}$, grew with time after plasma injection, even though the density gradient (presumed to be the energy source for the modes), decreased; and why $S(\omega)$ was so broadband.